Phase Changes in Silica and Their Impact on Mechanical Properties in 3-D Printed Investment Casting Molds

By

Ryan C. Breneman

A dissertation submitted in partial fulfillment
of the requirements for the degree of
Doctor of Philosophy
(Material Science and Engineering)
in the University of Michigan
2014

Doctoral Committee:

Professor John W. Halloran, Chair
Professor John Edmond Allison
Assistant Professor Emmanuelle Marquis
Professor Michael D. Thouless

I once was unlettered, unfettered and free,

(As to doubts, well I never had nursed one.)

A Philosopher said, full of dread, “don’t you see?

That the life unconsidered’s a cursed one!”

He made without scruple a pupil of me.

(As to learning, I wasn’t the worst one.)

The Philosopher posited chains and a key,

but he only delivered the first one.

-Zach Weinersmith

Acknowledgements

I must thank my advisor Prof. John Halloran for his help and support over the last four years. I’ve found his door is always open and our discussions always insightful, whether or not they were related to work. I’m particularly thankful for the freedom that has enabled me to cast a little iron on the side and become a home owner during my stay in Michigan.

This work was primarily funded by DARPA Grant HR-0011-07-1-0034, the Direct Digital Manufacturing of Airfoils, under Dr. Bill Coblenz. The DARPA team at large deserve recognition. This work would not be possible without Prof. Suman Das of Georgia Tech and his group including Dajun Yuan, Hassan Rashidi, and all the members of the LAMP team at GT. Our partners at PCC Airfoils, Inc. were also invaluable, in particular Don Deptowicz, Jon Jarrabet, and Tom VanVranken.

I must also thank the members of the Halloran group, both on and off the LAMP project. Susan Gentry, Sinhura Gangireddy, Vladka Tomeckova, Brad Wing and Philip Dodge were all of invaluable help over the years. Outside the group there are many others for me to recognize from my time at UM. I must thank my fellow graduate students for assistance with data and equipment over the years including Anne Jugganauth, Kiersten Batzli, Michael Waters, and Jacob Jokisaari. Also deserving of thanks are Dr. John Mansfield and Prof. Martha Mecartney of UCSB for their help in capturing SEM of cristobalite.

I’m also grateful to John “Chip” Keough for enabling and encouraging me to pursue my love of metal casting. The opportunity to assist in the occasional steel or ductile iron pour was one of the highlights of my time in Michigan. Chip was also instrumental to introducing me to the Foundry Education Foundation which in turn precipitated my forthcoming employment in the experimental foundry at Pratt-Whitney.

I am incredibly thankful to my family and their continued love and support through my lengthy education. I’m thankful to my mother for her love and the early education she provided putting me on my current path. I’m thankful to my father for his aid and guidance in helping me make the most of the opportunities I’ve had. I’m thankful to my brother for sharing in my nerdy interests over the years. I’m thankful to my grandmother for her conversations over the years and her deep interest in my life and work. (I think she could give my thesis talk) I’m also deeply thankful for the wisdom shared by my late Grandfather.

Perhaps most of all, I am thankful for the love and support of my fiancé Caroline Sheehan without whom the past two years would have felt empty. In particular I am thankful for her support and patience in the past few months with the many late nights dedicated to the present document.

Table of Contents

List of Figures

List of Tables

Abstract

The devitrification of amorphous silica to cristobalite and the subsequent beta-alpha transformation of cristobalite were studied as well the impact of both transformations on mechanical properties. The work was motivated by the need to transform 3-D printed green molds composed of acryaltes and 60 vol% silica particles into refractory molds for the casting of single crystal Ni-superalloy. The 3-D printed molds were produced by Large Area Maskless Photopolymerization (LAMP), a process that selectively cures layers of photo-suspension with patterned UV light to produce solid objects. Cristobalite content was required to achieve sufficient sintering and creep resistance in the in the sintered silica molds. However, cristobalite lowers room temperature strength due to cracking caused by the beta-alpha transition, requiring a compromise between creep resistance and strength. The development of crack-like flaws in LAMP molds prior to sintering was also addressed.

The kinetics of the crystallization of amorphous silica to cristobalite was investigated and a time-temperature-transformation or TTT diagram was developed. The impact of seeding with cristobalite powder and use of silica with residual crystalline quartz were examined. The stress relaxation of partially crystalline sintered silica under fixed strain was studied as a function of cristobalite content. The results are used to infer the impact of cristobalite on the creep and sintering resistance of partially crystallized sintered silica. The impact of cristobalite on strength of sintered silica was explored.

The strength of partially crystalline sintered silica samples were tested at 350°C as beta-cristobalite having never cooled through the beta-alpha transition, at 25°C as alpha-cristobalite having passed the beta-alpha transition, and at 350°C as beta cristobalite having been cooled through the beta-alpha transition and subsequently reheated. The stress and fracture induced by the beta-alpha transition was also examined in the context of a model system: bulk silica glass. The formation of cristobalite spherulites on the surface of the glass and the development of stress and fracture were observed. The beta-alpha transition of cristobalite was also explored by differential scanning calorimetry (DSC) of sintered cristobalite repeatedly cycled through the beta-alpha transformation and the impact of cycling on hysteresis and transformation enthalpy was observed.

Chapter 1
LAMP: Additive Manufacturing for Investment Casting

1.1 Additive Manufacturing: A Revolution?

3-D printing and its potential to transform manufacturing have been a source of great excitement in recent years. At the start of the decade this enthusiasm reached new heights with the New York Times hailing a "manufacturing revolution" in 2010[1] and The Economist calling 3-D printing the "3rd Industrial Revolution" in April 2012.[2] The importance of 3-D printing as a new technology has been cemented in the public and corporate mind in the years since. More recently in September 2013 The Economist writes on the "scale up" of 3-D printing and its integration into business,[3] while in January 2014 Forbes depicts 3-D printing as key to the future of manufacturing.[4] For many Americans the role of 3-D printing in our future was confirmed by President Obama's nod to the technology in his 2013 State of the Union address and the advent of 3-D printed firearms in the last year. Clearly 3-D printing has captured the hearts and minds of the public, but what about the innovation behind this excitement?

3-D printing also referred to as "additive manufacturing" is a diverse area encompassing many processes with little else in common. Processes as diverse as laser sintering, stereolithography, polymer extrusion, and powder/binder systems are all considered to be additive manufacturing, despite relying on completely different methods. These processes all fall into the category of additive manufacturing because they produce 3-dimensional solids by the assembly of powder or fluid starting materials.

The core of additive manufacturing is that solid objects are assembled from base material, as opposed to classical manufacturing in which solids are machined or formed from a bulk.

It is easy to appreciate the appeal of such processes and the resulting enthusiasm they have generated. Many laypeople imagine a future with no stores in which consumers purchase blue prints online and build their own goods with a home 3-D printer. The more pragmatic among us recognize this extreme as a fantasy, but the appeal of 3-D printing techniques in many areas is great. With additive manufacturing products can be changed or customized on demand with the simple alteration of a CAD file. This can eliminate the costs and lead times associated with new tooling, allowing more rapid innovation and even product customization. Another appeal is that additive manufacturing appears at first glance to be inherently greener; products are assembled from a starting material producing little to no waste. This contrasts with traditional methods in which raw materials are machined down to produce a final product. The potential for additive manufacturing to revolutionize industry is a clear and present fact.

Despite the promise of 3-D printing and additive manufacturing, the process has not bridged the gap from prototyping to production. For now, it has yet to dramatically alter the way goods are produced. 3-D printing replaced traditional methods for prototyping and producing demonstration parts in the early 2000s, but the technique hasn’t bridged the gap to mass produced products. Traditional methods still remain cheaper and better for large scale production. The accurate and customizable plastic parts produced by photocuring processes such as Stereolithography remain expensive and slow to produce. Laser sintered ceramic and metal parts do not have nearly as high strength as their equivalents produced by traditional methods. Outside the success of Invisalign's customized 3-D printed orthodontics no common products are currently produced by 3-D printing.

The present work was motivated by a DARPA project with the goal to bridge the gap and move from 3-D printing to Direct Digital Manufacturing or DDM. The aim of the project is to replace the current extensive and unwieldy manufacturing process used to produce jet engine airfoils with a simple 2-step process based on 3-D printing. This goal is both ambitious as well as pragmatic. Jet engine airfoils are devilishly complex objects composed of what is arguably the most advanced alloy used by mankind, but this same complexity allows a 3-D printing technique to compete despite the high costs associated with the technology. Crucially, we avoid the pitfall of replacing a highly engineered conventional material with a 3-D printed object. Instead of producing blades directly, we seek to produce the refractory casting molds by additive manufacturing, and use these molds to cast blades conventionally. Thus the extensive manufacturing process is replaced, and the gains of 3-D printing are captured, while retaining the material quality of current methods in the finished part.

1.2 LAMP: Large Area Maskless Photopolymerization

1.2.1 Introduction to LAMP

Large Area Maskless Photopolymerization or LAMP is the additive manufacturing process which motivated the present work. LAMP is the brain child of Professors John Halloran of the University of Michigan and Suman Das of Georgia Tech. The goal of LAMP is to produce solid ceramic components by a scalable additive manufacturing technique. The photopolymerizable suspension technology was developed at UM while the actual LAMP machine was created at Georgia Tech. The technology is being advanced by the startup DDM Systems and a LAMP machine is in place at PCC Airfoils in Wycliffe, Ohio.

LAMP is a UV-curing based additive manufacturing method, in which layers of suspension are deposited and then selectively cured by UV illumination. The areas exposed to UV are cured to a solid while the unexposed areas remain fluid. Subsequent layers are deposited on top and likewise cured. The remaining fluid can then be drained away, leaving a 3 dimensional solid formed from the UV cured material.[5] An idealized schematic of the LAMP apparatus is shown in Figure 1.1; a large number of partially build molds are shown with photocured solid molds (white) immersed in uncured suspension (transparent in image). In this schematic the top layer of suspension is being polymerized by UV light patterned by the digital micro-mirror device (DMD).

In LAMP, the UV curable suspension is a ceramic loaded acrylate suspension. Acrylate monomers, photo-initiators, dyes, inhibitors, and dispersant are mixed with 60 vol% silica powder. The high solids loading enables the production of a silica ceramic following the burn out of the acrylate binder. LAMP differs from other processes, in this regard; the additive manufacture process is achieved by UV curing of polymers, which can be done with high resolution and low energy, but the final part is a sintered ceramic. Therefore LAMP has an advantage over laser sintering processes in that it does not require high energy lasers to form the build, but still produces a ceramic part. Likewise, LAMP has an advantage over stereo-lithography in that it produces a usable ceramic and not just a polymer prototype. There are ceramic stereolithography processes based on a ceramic loaded suspension similar to LAMP; however, such processes are very slow.[6]

1.2.2 The LAMP Build Process

The LAMP machine operates by depositing a layer of suspension and then selectively curing that layer with patterned UV light. The UV exposure is pattered by a digital micro-mirror device or DMD similar to those used in projectors. After a layer of suspension is deposited, a "print head" rasters across the surface selectively illuminating the suspension with UV light. The illuminated area cures into a solid while the unexposed areas remain liquid. The illumination by the print head adjusts dynamically on rastering across the surface ensuring illumination of the "pixels" destined to become solid. A schematic of the LAMP device is in Figure 1.2 and a detailed view of the print head is shown in Figure 1.3.

Fresh photo-curable suspension is deposited to create each layer. The base of the LAMP build is a flat plate. For the first layer, the recoater sweeps across the build platform depositing a smooth even layer of suspension 100 microns in depth. The suspension is fed from the recoater at the leading edge. The recoater sweeps over the base at a height of 100 microns leaving a layer of material 100 microns thick in its wake. At the leading edge, excess suspension is dragged forward and dumped into a collection pan at the edge of the build surface. The excess suspension is then filtered and recycled. Subsequent layers are deposited on top of the preceding layer of material after it has been cured.

The continued deposition and curing of additional layers creates a 3-D object. Following the deposition of a layer of suspension the print head sweeps the build, selectively curing the suspension. The build platform is then lowered by 100 microns, and a new layer of suspension is deposited. The process repeats until the part is completed, for example, a 76 mm (~3 inch) tall build requires 760 layers.

This method of building requires that a containing "wall" be built along with the intended parts, as the uncured suspension is still fluid and would flow if permitted to. A single layer is of insufficient depth for flow to occur, but for multiple layers the uncured suspension must be contained. This is accomplished by curing a perimeter dam around the build surface to contain the liquid suspension. The body of liquid could slosh and damage the builds in progress requiring further containment. A secondary "dam" is built around each part and the area between the parts is lightly hatched to contain the liquid suspension in small pockets, this prevents sloshing while minimizing wasted material as the entrapped liquid can be collected upon completion of the build and reused.

Following the build, LAMP parts must be broken out and the uncured suspension must be removed. The walls which prevented fluid flow during the build must be broken away after the build is completed. This process is done manually and is termed "break out" by the LAMP team. The excess cured material from break out is discarded, while uncured suspension can be collected and reused. Following break out the fluid trapped inside the molds must be cleared. The mold interior has many tight areas which can trap the viscous suspension, especially in the core. This remaining trapped liquid suspension is removed during a process we call "development." During development, the molds are immersed in a proprietary solvent blend and gently agitated for several hours, dissolving and removing the liquid suspension while the cured polymer remains.

The LAMP process was a joint development between the Suman Das group at Georgia Tech and the John Halloran group at the University of Michigan. The UM team was responsible for developing the photopolymerizable suspension and the conversion of the as built components into sintered refractory ready for investment casting. The GT team was responsible for the design and fabrication of the LAMP hardware, controls, data processing, software, mold design, and mold development. The LAMP hardware is constructed from a modified Basysprint 7102 UV-setter printer. The Basysprint machine was originally designed to expose photoresist for the patterning of printing plates used in high-quality magazine printing. This provides an excellent curing platform for the LAMP machine providing curing resolution within the build layer of 8.4 microns. Of course, the recoating system, and build platform were constructed separately by the Georgia Tech team. The completed beta version of the LAMP machine can be seen in Figure 1.4.

1.3 DARPA DDM of Airfoils for Investment Casting

The present work was funded by and conducted in support of DARPA grant HR-0011-07-1-0034, the Direct Digital Manufacturing of Airfoils. The work was sponsored by Dr. William Coblenz of DARPA. The goal of the project is the production of jet engine airfoils by additive manufacturing methods. Since it is not possible to produce nickel super-alloy by additive manufacturing techniques, this was pursued through the additive manufacture of refractory molds to cast the airfoils. LAMP was determined to be a promising technology to reach this end.

1.3.1 Airfoil Background

The design of jet turbine airfoils is complicated by the demands placed upon them. The efficiency of a jet engine is determined by the difference in temperature between the incoming and outgoing air. The higher temperature the engine can operate at the better the performance and the more efficient the engine. This has lead to the current state of the art in which engines operate at temperatures ABOVE the melting point of the alloy which composes the blades. This remarkable feat is accomplished by the use of interior cooling passages, which complicate the manufacturing of the turbine blades, and ceramic barrier coatings, which are not discussed here. These interior passages are produced by casting the metal around a ceramic core which is subsequently leached out of the airfoil. Figure 1.5 shows an example of a cast single-crystal turbine airfoils with the wall cut-away to view the interior passages.[7] The ceramic core responsible for the passages appears to the right. During casting, metal surrounds the ceramic core and solidifies; following casting the core is leached out to produce the interior passages.

Jet engine airfoils are currently produced by investment casting. A schematic of the current industry process appears in Figure 1.6. Step 0 represents the tooling and preparation for injection molding of the ceramic cores. Airfoil cores are produced by injection molding and subsequent firing, illustrated in Step 1 as a sintered airfoil core. These cores are then manually dressed in preparation for injection molding of wax. Wax injection is depicted in Step 2. The wax will become the metal in the final airfoil. Following wax injection the blades are manually assembled into “trees” in which many blades are gated together to be cast from a single pour cup and sprue, as illustratd in Step 3. This wax assembly will become the passages which guide the molten metal to airfoil mold. The process then becomes automated as the wax trees are coated in ceramic slurry and stuccoed, depicted in Steps 4-5. The ceramic shell becomes the mold during casting. The wax is burned out and the ceramic is sintered to achieve appropriate strength for casting, illustrated in Steps 6. Casting of the alloy follows in Step 7. During casting the mold is held at ~1550 for several hours as the metal is poured and slowly cooled to achieve a single crystal on solidification. Following casting the ceramic core must be leached out by a NaOH leaching processs at high-pressure, depicted in Step 8. Rigorous inspections follow as depicted in Steps 9 through 12.

Production of the ceramic cores is a significant hurdle in the fabrication of the finished airfoil. The injection molding places geometric constraints on the cores with certain shapes being impossible to form. This places design limitations on the cooling passages of the final airfoil. Additionally, due to the exacting dimensional standards and great complexity of the airfoil cores the manufacturing yield tends to be low. An additional constraint is the chemical and phase composition of the core. The core must be primarily composed of silica to allow chemical removal of the core after casting, but silica can be challenging to use as a refractory. Amorphous silica has poor resistance to creep at high temperatures and must be partially crystallized to maintain dimensional tolerance during sintering and casting. However, the crystalline phase that forms under ambient conditions, cristobalite, also induces micro-fracture at room temperature, potentially causing mechanical failure. This trade-off between high-temperature creep resistance and room temperature strength must be managed for successful core production.

1.3.2 Project Motivation

The current investment casting process for producing airfoils is very labor and tooling intensive resulting in huge lead times and costs associated with changes in design. An industry representative has given the rule of thumb that minor changes cost $500,000 and 6 months for new tooling and major changes are even more expensive and time consuming, motivating the DARPA funding for additive manufacturing. The current process makes it cost prohibitive to produce test designs which slow innovation. An even more immediate concern to US Navy and Air Force accountants are legacy parts. Many engines are being extended beyond their original design lifetime, requiring unplanned replacement parts. The original tooling is gone and the replacement parts are exhausted, but it is prohibitively expensive to produce a limited run of replacement parts by conventional methods. An additive manufacturing process could potentially lower the cost of such limited replacement runs dramatically. The current goal for LAMP is to produce a process which can allow the production of limited runs of old airfoils and experimental designs while avoiding the large start-up tooling costs of current methods.

1.3.3 LAMP Builds to Airfoil Castings

Molds were built by the LAMP process at GT and then sent to UM for binder burn-out and high-temperature sintering. Molds deemed of high enough quality were then sent to the PCC foundry in Minerva, Ohio for casting.

Unsintered, or green, LAMP molds received from GT were fired at UM. The green mold is the LAMP produced body after the interior has been cleared by development but before binder removal and sintering. The green molds are 60 vol% silica powder, but the entirety of the strength comes from the photo-polymerized acrylate matrix. The green bodies have sufficient strength to be handled safely with little concern for breakage. The cores are very delicate, but they are protected inside the mold.

The acrylate polymer is removed through binder burn-out or BBO in which the polymer is pyrolized leaving a ceramic part. The green molds are slowly heated to 600°C over the course of 10 hours with the details of the firing schedule graphed in Figure 1.7.

All of the organics pyrolize leaving only the silica. BBO is carefully controlled as the pyrolysis of the organics produces stress which can cause breakage and defect formation.[8] The BBO schedule for LAMP was developed to have slow heat rates through the temperatures at which mass loss occurs, as determined by thermal gravimetric analysis. Following BBO the mold is incredibly fragile as the polymer acrylate that provided strength in the green state has been removed, but the ceramic has not been sintered to develop any strength.

Following the BBO, the molds are moved to a high temperature furnace for sintering. Molds were sintered at 1350°C for 1 hour with 15°C/min ramps on heating and 10°C/min ramps on cooling with the detailed sintering schedule graphed in Figure 1.7. This heating schedule achieves a 80±3% cristobalite content and 28±1% open porosity. The high heating rates were used to limit sintering shrinkage by facilitating fast crystallization. Sintering was conducted under ambient atmosphere. Following sintering molds had sufficient strength for handling and casting. The amount of crystalline cristobalite developed during sintering is of great importance, motivating the present work. At the foundry, the molds are heated to casting temperature of ~1550°C a immediately prior to casting. This high temperature firing fully crystallizes the mold, but due to the crystallization accomplished in the initial sintering anneal no shrinkage occurs. An insufficient initial sintering step would result in sintering shrinkage upon heating to casting temperature and possibly result in failure of the mold.

This two-furnace firing procedure is not ideal. It would be better for BBO and sintering to be done without any movement in between given the fragile state of the molds. Unfortunately, we were limited to using a vented low temperature furnace for

BBO due to the fumes produced and a separate furnace with high temperature capability for sintering.

Successful molds were sent to PCC Airfoils Inc. at Minerva, Ohio for casting following BBO and sintering. There the molds were integrated into the established casting process by gating the LAMP molds together in a wax assembly. The ceramic LAMP molds were attached to the wax gating that would typically be used to attach the wax airfoils in the conventional process. The conventional suspension coat and firing procedures were then followed, resulting in the LAMP molds being covered by a coat of ceramic refractory. This inefficient process of substituting ceramic LAMP molds for the wax airfoil body in a conventional assembly was necessary as a short term means of casting LAMP molds. More direct methods will be developed in the future.

1.3.4 Green Molds Produced by LAMP

The LAMP process successfully produced high detail integrally cored molds. The outer shape of uncored molds can be seen in Figure 1.8 both with and without internal illumination. A cored mold cut-away is shown in Figure 1.10 and a labeled close up view of the core is shown in Figure 1.10, these molds were built at 45° angle to vertical in the images. During casting the outer wall defines the internal shape of the airfoil, while the core defines the interior cooling passages of the finished blade. These cored molds are referred to as "integrally cored molds," because the core and mold are a single solid piece; such integrally cored molds can only be produced by additive manufacturing methods.[6] Producing integrally cored molds offers the potential to replace many current manufacturing steps, saving both production costs and lead times associated with conventional methods. All molds produced were "dummy" designs not limited by export control restrictions. In these molds the features of the core were designed to have the manufacturing challenges of real designs but not the aerodynamic properties of real airfoils. The high detail that was captured with LAMP can be seen in the cut-away image in Figure 1.10. The flag holes, for example, are approximately 250 microns in diameter, and the angled leading edge film cooling rods are 450 microns in diameter.

Successful production of integrally cored mold was a great design challenge. The photopolymerization of the ceramic loaded solid is a complex problem as discussed in Chapter 7. In addition to the photo-curing parameters, the builds themselves required significant innovation. The mold design presented another major challenge; as LAMP is a layered build process from a liquid base, which presents geometric constraints. Any area in a LAMP layer that is to be solid must connect in some way to solid in the previous layer. Solid areas that appear out of liquid on the previous layer are deemed “islands” and cannot be produced. This necessitated tilting the mold orientation relative to the build direction for the molds with complex cores, as seen in Figure 1.10.

1.3.5 Single-Crystal Super-alloy Cast in LAMP Molds

Successful single crystal nickel-superalloy blades were cast in LAMP molds. These can be seen in Figure 1.11. These are uncored blades as the cores were found to break in cored molds as discussed in Chapter 7. The blades produced by LAMP were found to have great dimensional accuracy. The vertical lines seen in Figure 1.11 are the result of tessellations in the .STL files used to build the molds. That is, the LAMP molds had greater accuracy than the digital files used to produce them. Of course in the build direction the LAMP process produces poorer resolution due to the 100 micron layer thickness in the build direction. White-light measurements of an earlier LAMP casting can be seen in Figure 1.12. White-light is a measurement technique in which the surface is measured in 3-dimensions and compared to a CAD model standard. It can be seen that the LAMP blade has very little distortion other than the top of the platform and some flashing on the side. It should be noted, this white-light measurement was not calibrated to the shrinkage from the LAMP process, so only the relative distortion between areas is useful.

Of course, successful casting of Ni-superalloy did not come easily. The first attempt in the spring of 2011 resulted in disastrous failure of the LAMP mold, as can be seen in Figure 1.13. The LAMP mold shrank away from the slurry coat applied at PCC and cracked up. When metal was cast, it flowed through the cracks and encased the LAMP mold. The innovative LAMP produced mold had failed in its basic role as a refractory.

1.3.6 Basics of Silica Casting Refractories

This forced us to reconsider the very basics of high temperature refractories in order to for our advanced, disruptive technology to surmount the basic “old” problem of handling high temperatures. The investment ceramics commonly used in industry utilize several techniques to avoid shrinkage and failure. First, commercial systems use gradients of particle sizes. Small particles are applied to the wax body first to capture detail and then successively larger particles are applied. These larger particles have less surface energy and therefore less driving force to sinter and shrink, providing greater support at high temperature. In a LAMP build, we are limited to a single particle size in our suspension. We must use small particles to achieve the best resolution possible, and so this method is not usable for us. Secondly, industry formulations use multiple ceramic components including alumina and Zirconia in addition to silica. In LAMP, we must use slurries which are transparent to UV in order to have proper curing. The UV light must pass into the suspension with minimal scattering, necessitating a refractive index match between the ceramic and the suspension. We also must use silica as the majority constituent so that the core can be removed from the airfoil after casting. The refractive index of silica does not match that of Zirconia or alumina, and so pure silica must be used. Finally, in industry the silica is crystallized to cristobalite during use. The crystalline phase has far greater resistance to creep and sintering than the amorphous phase. However, cristobalite is known to weaken materials by cracking at room temperature. We must use cristobalite to control the sintering and creep of the LAMP mold, but there is a trade off to its use. This work is motivated by the need to understand the formation of cristobalite in amorphous silica and its impact on the creep behavior and the strength, in order to better inform the creation of successful LAMP molds.

1.4 Conclusions:

3-D printing or additive manufacturing shows great promise to revolutionize industry, but currently few processes have bridged the gap from prototyping to production. This work was motivated and funded by the DARPA initiative to use additive manufacturing techniques to enable the direct digital manufacturing of jet engine airfoils and eliminate the costs and time associated with conventional methods. This is approached by using the LAMP process to build a ceramic mold for the casting of the airfoils. By taking this approach, we can eliminate the extensive and expensive process of creating these molds by conventional methods while retaining the superior properties of the cast alloy produced by conventional means. This hybrid of conventional and additive techniques seeks to take the best from both processes.

As a member of the DARPA team, my role was to develop the firing processes necessary to take green LAMP molds and produce refractory capable of handling single-crystal super-alloy casting. This proved to be a crucial hurdle to the success of the project. It was found that the limitations placed by the LAMP process prevented the use of many of the creep reduction techniques utilized in conventional refractories. Instead, we were forced to solely rely on the crystallization of amorphous silica to cristobalite to provide the needed properties. This motivated the study of the transformation of amorphous silica to cristobalite and its impact on the mechanical properties of sintered silica.

1.5 References

1. A. Vance, "3-D Printing Spurs a Manufacturing Revolution." The New York Times. September 14, 2010.
2. "The 3rd Industrial Revolution." The Economist. April 21, 2012.
3. "3-D Printing Scales Up." The Economist. September 7, 2013.
4. R. Sharma, "The Future of 3-D Printing and Manufacturing." Forbes. January 15, 2014.
5. J. W. Halloran, V. Tomeckova, S. Gentry, S. Das, P. Cilino, D. J. Yuan, R. Guo, A. Rudraraju, P. Shao, T. Wu, T. R. Alabi, W. Baker, D. Legdzina, D. Wolski, W. R. Zimbeck, and D. Long, "Photopolymerization of powder suspensions for shaping ceramics," *J. Eur. Ceram. Soc.,* 31[14] 2613-19 (2011).
6. C. J. Bae and J. W. Halloran, "Integrally Cored Ceramic Mold Fabricated by Ceramic Stereolithography," *International Journal of Applied Ceramic Technology,* 8[6] 1255-62 (2011).
7. A. A. Wereszczak, K. Breder, M. K. Ferber, T. P. Kirkland, E. A. Payzant, C. J. Rawn, E. Krug, C. L. Larocco, R. A. Pietras, and M. Karakus, "Dimensional changes and creep of silica core ceramics used in investment casting of superalloys," *J. Mater. Sci.,* 37[19] 4235-45 (2002).
8. K. E. Hardina, J. W. Halloran, M. Kaviany, and A. Oliveira, "Defect Formation During Binder Removal in Ethelyne Vinyl Acetate Filled System," *J. Mater. Sci.,* 34 3281-90 (1999).

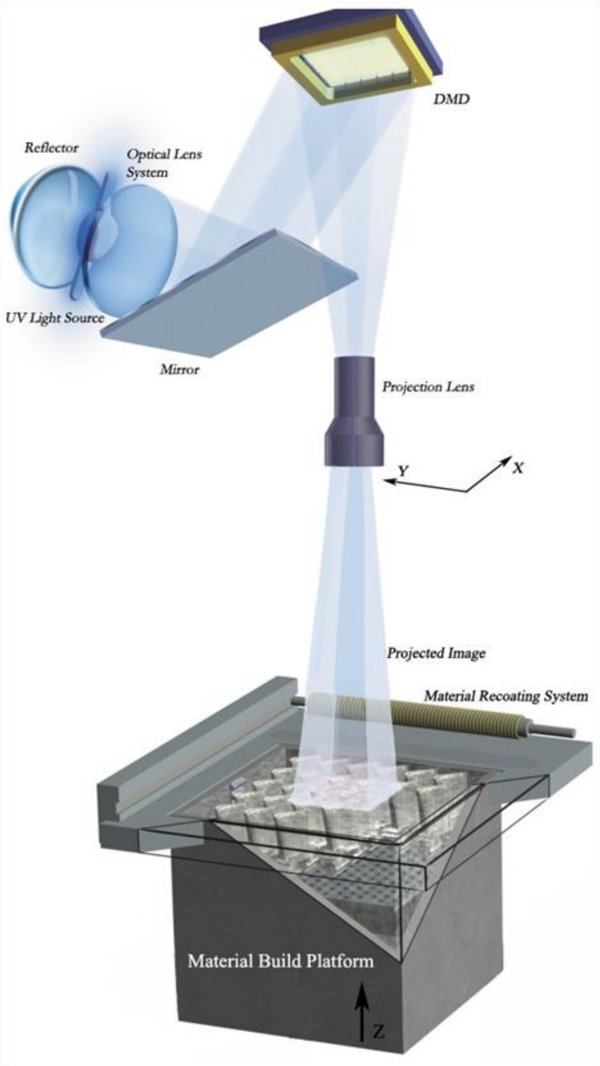

Figure 1.1 Idealized illustration of the LAMP apparatus. The current layer of partially built molds is shown being selectively cured by UV patterned by the DMD.

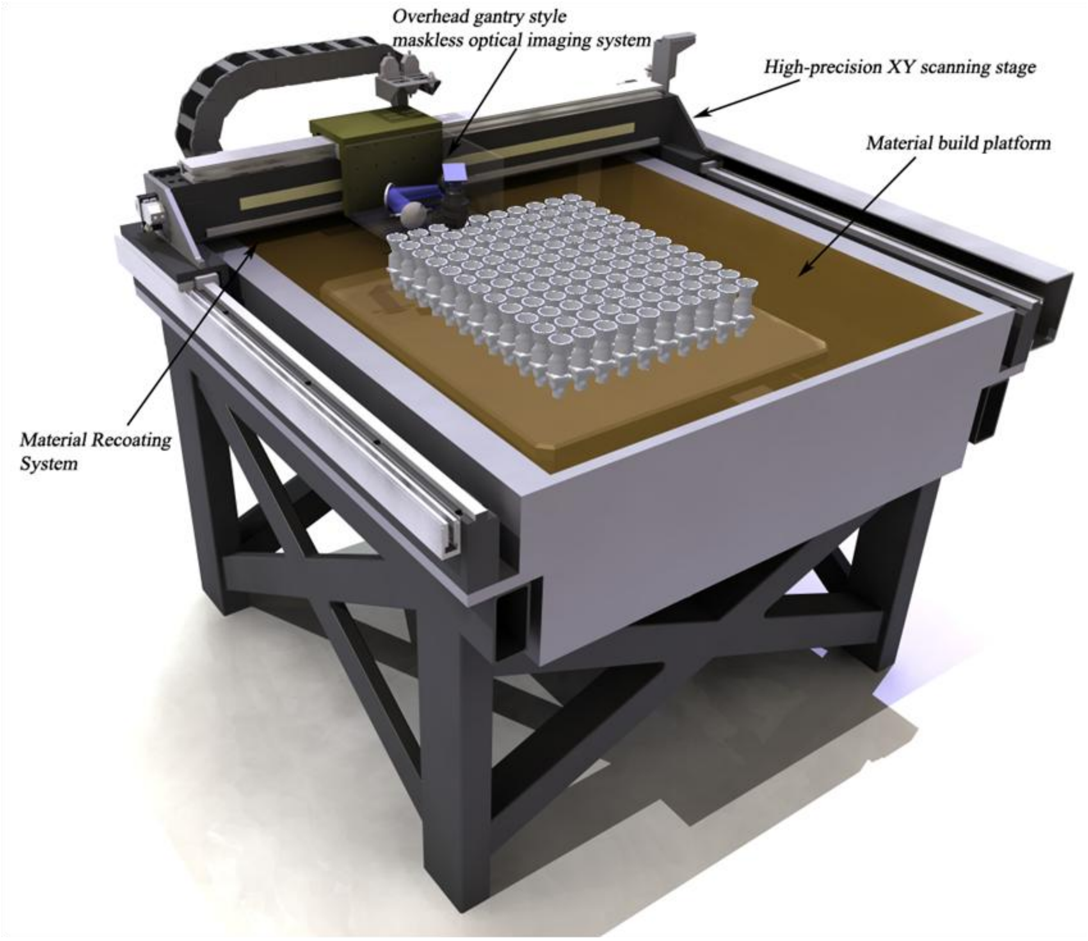

Figure 1.2 Schematic for LAMP apparatus stripped of obscuring covers.

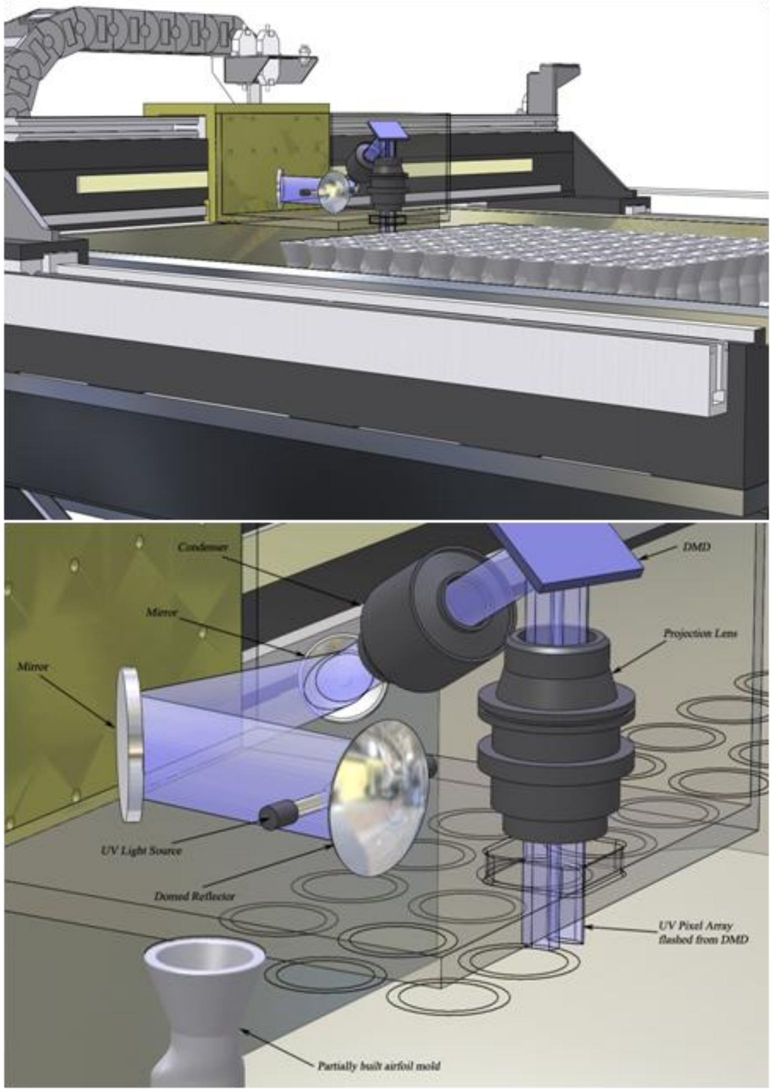

Figure 1.3 Close up of UV-print head in schematic view of LAMP apparatus.

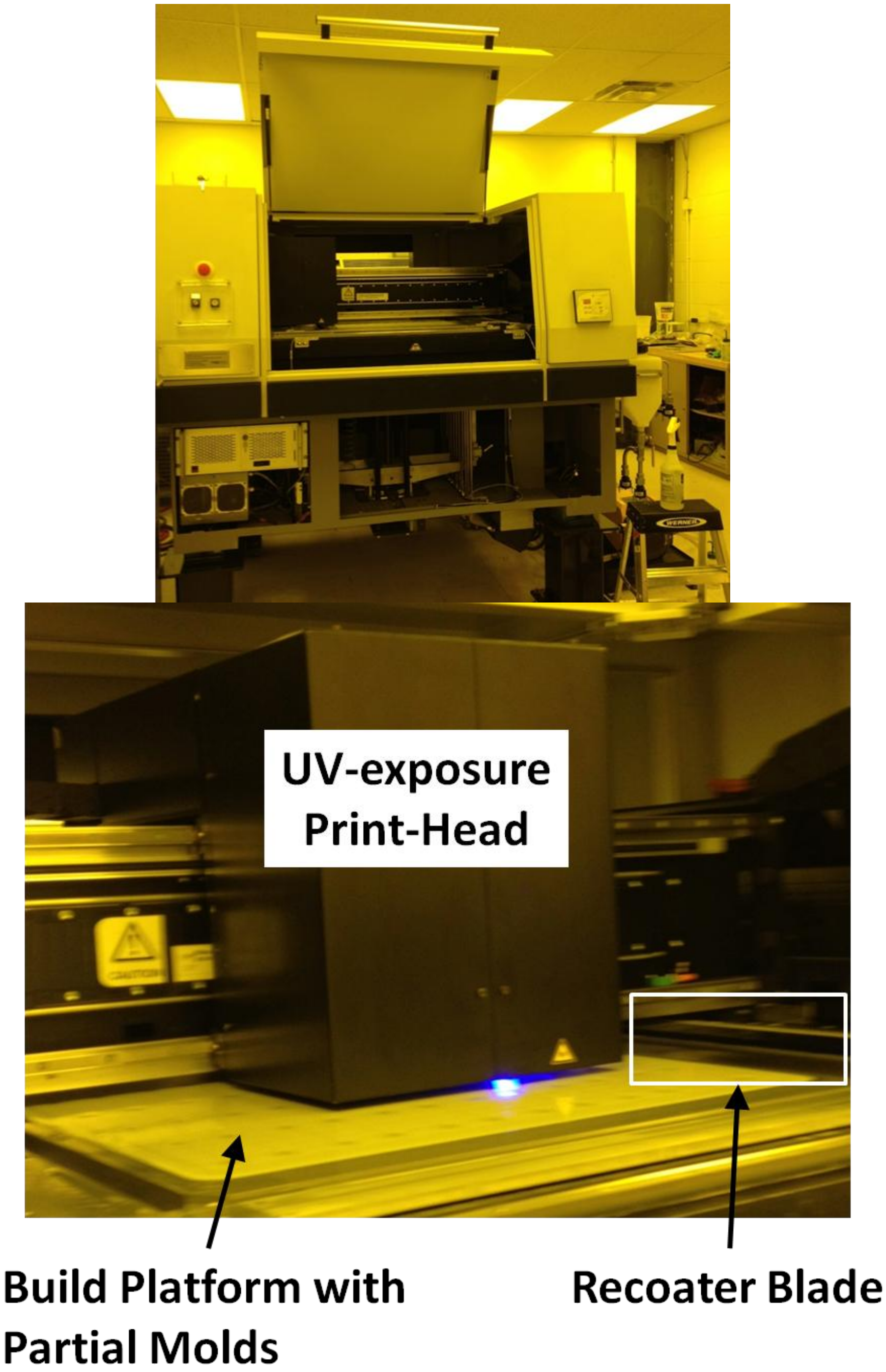

Figure 1.4 Images of LAMP-Beta machine. Top: Complete system installed at PCC Airfoils in Wickliffe, OH. Bottom: Close up view during exposure of a layer. The flat ivory surface is the photocured suspension with many molds on the build platform. The UV exposure head is traversing the surface, selectively exposing and curing the suspension with patterned UV. To the right is the recoater blade which will deposit a new layer of suspension after the build platform has been lowered following exposure of the current layer.

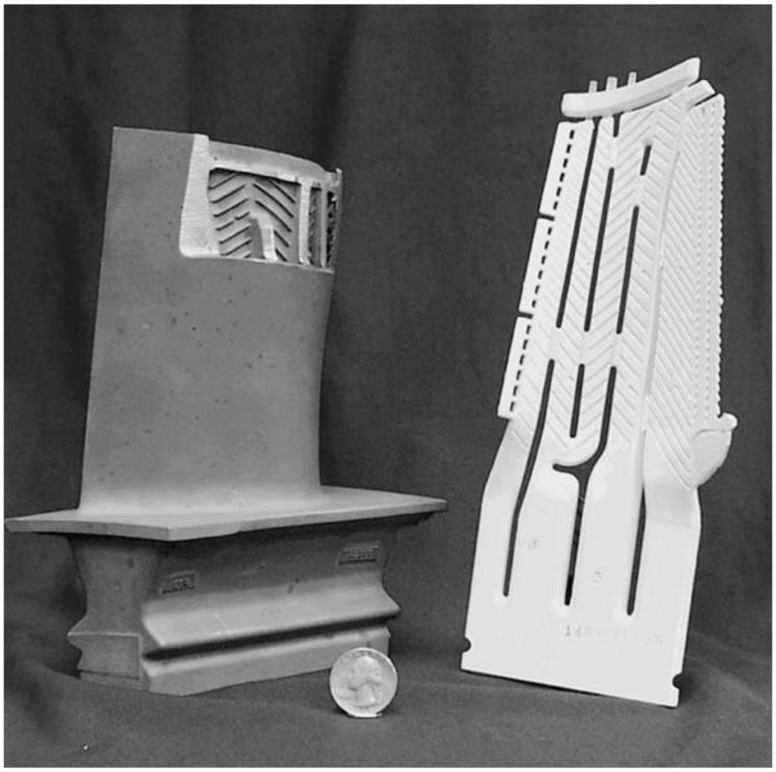

Figure 1.5 Example of hollow-cored airfoil with outer wall cut away to reveal interior cooling passages (left) and corresponding silica-based refractory core that goes inside the wax pattern to form the interior cooling passage (right), from Wereszckak et al 2002.

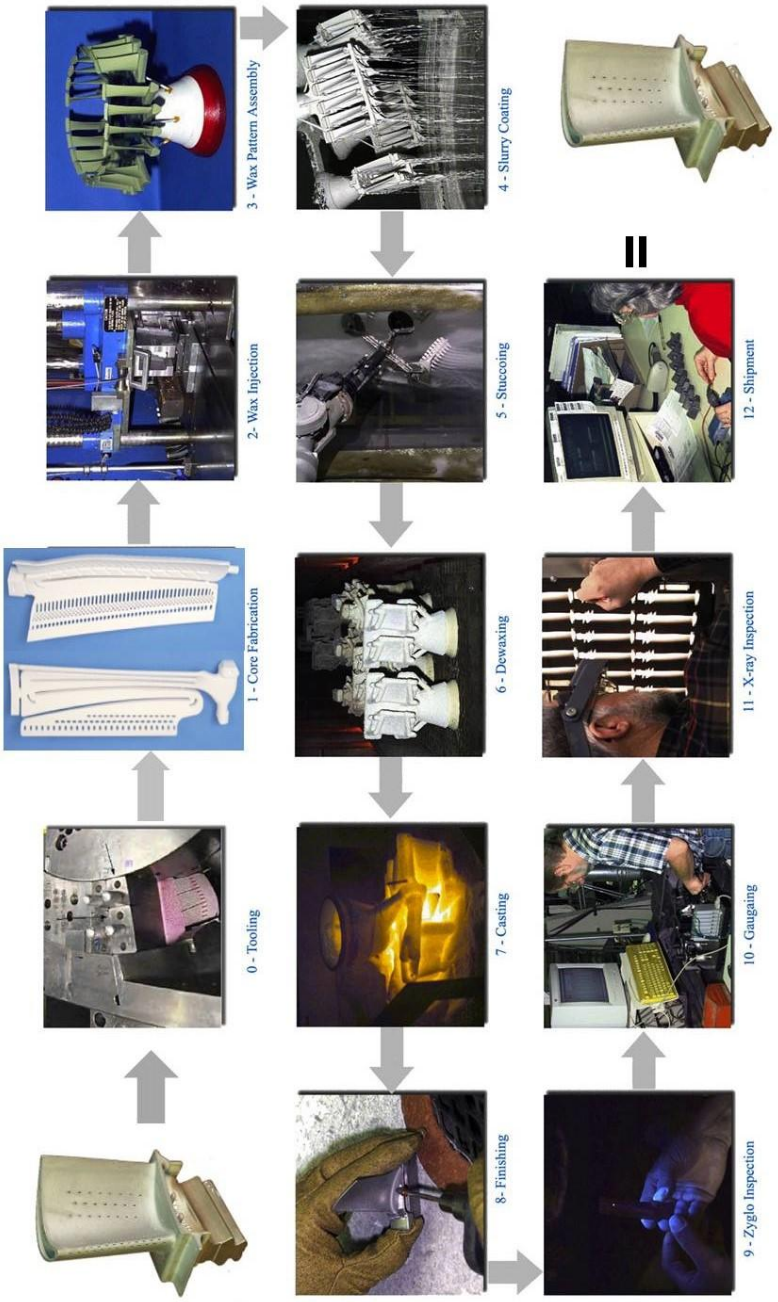

Figure 1.6 Current airfoil casting process showing sequence of steps to produce an airfoil. Step 0 is the preparation and tooling for producing the core by injection molding; Step 1 is the creation of the ceramic core; Step 2 is wax being injected around the core to produce the cored wax airfoil pattern; Step 3 is the assembly of the wax patterns; Step 4-5 is the application of the ceramic shell mold onto the wax patterns; Step 6 is the wax removal and sintering of the ceramic shell mold; Step 7 is the casting of the Ni-super-alloy in the sintered shell mold; Step 8 is the removal of the ceramic core; and Steps 9-12 are the inspection and certification of the cast airfoil.

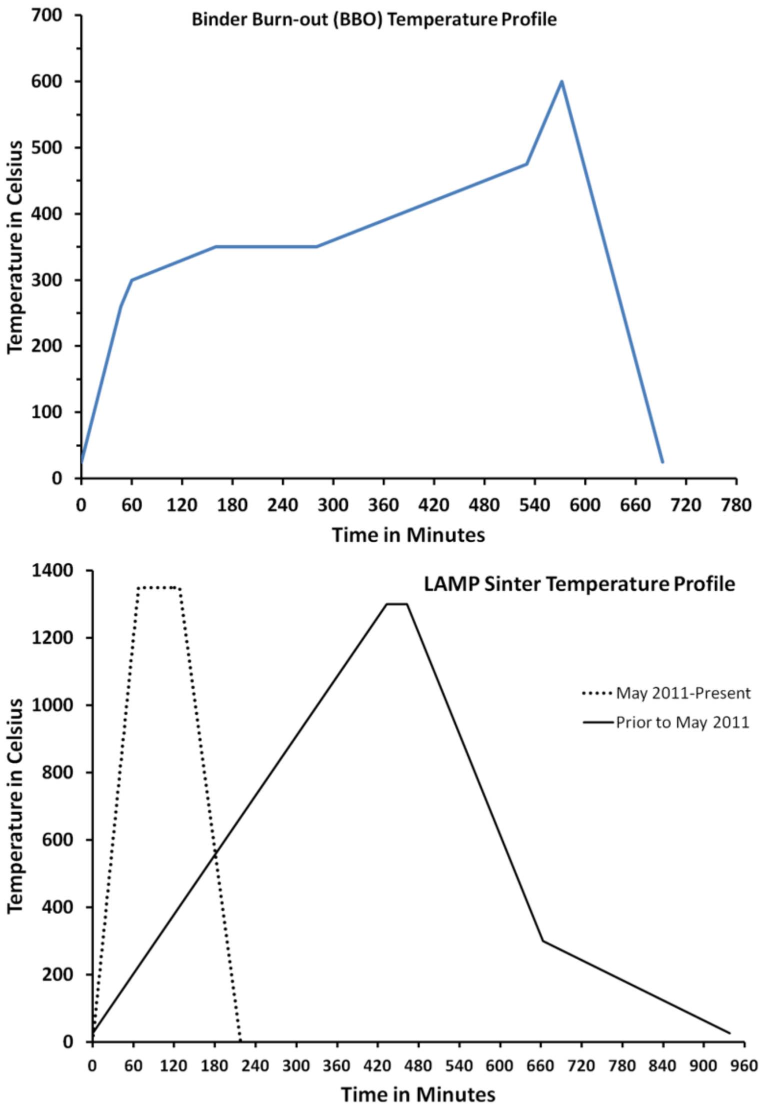

Figure 1.7 Binder Burn-out (BBO) firing schedule designed for slow heating during pyrolysis as determined by thermal gravimeteric analysis (top). Sintering firing schedules used in the LAMP project to achieve sintered silica with 80±3% cristobalite content and 28±1% open porosity (bottom).

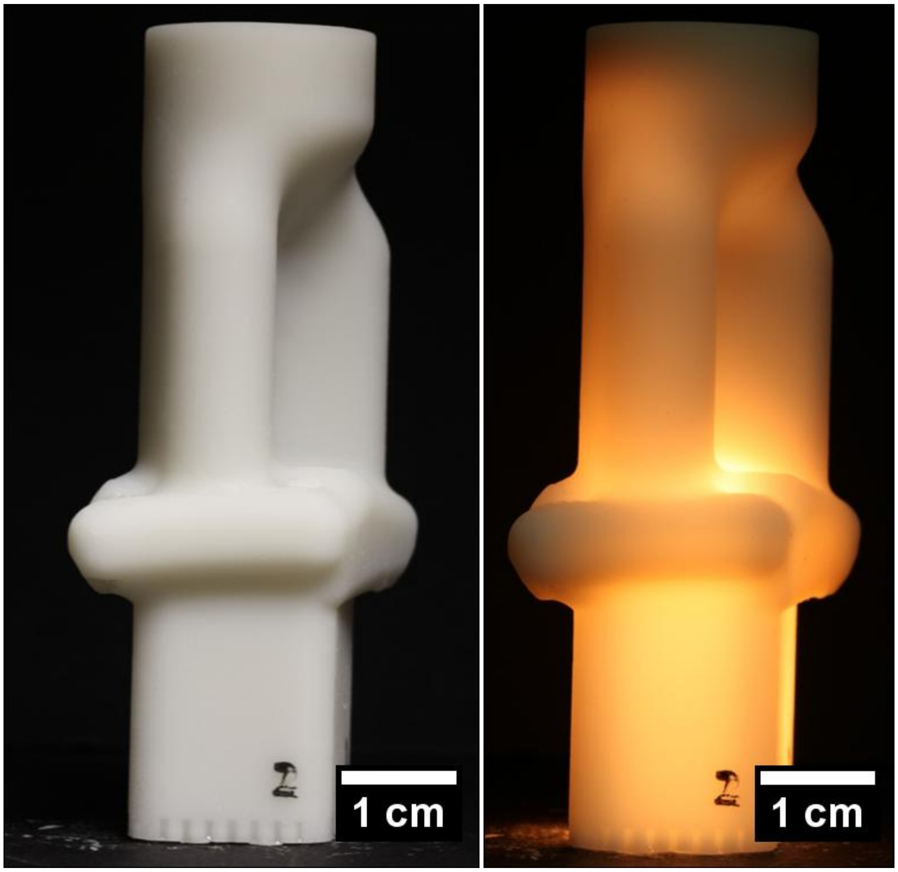

Figure 1.8 LAMP green molds with and without internal illumination.

Figure 1.9 Integrally cored mold with side wall cut away to view the core. The external walls define the shape of the airfoil while the interior core defines the cooling passages in the cast airfoil. This was built at a 45° angle from the vertical direction of the image.

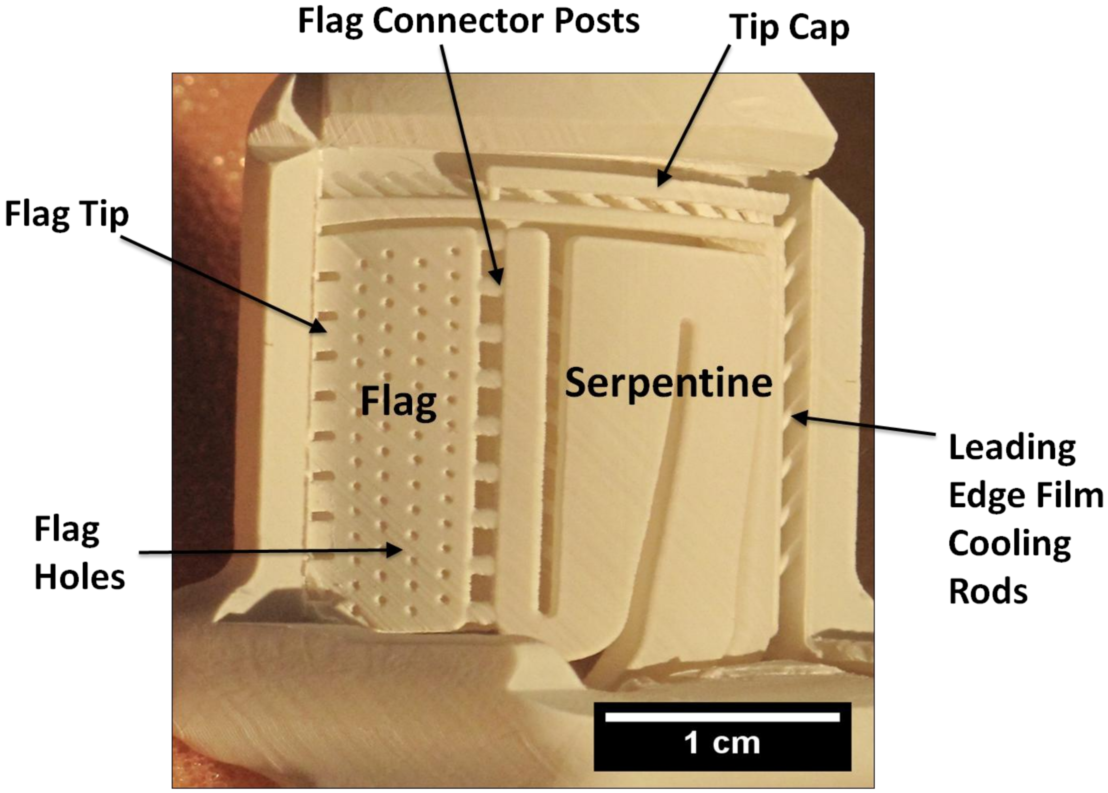

Figure 1.10 Close up of core with labels in an integrally cored mold with side wall cut away. The flag holes are This was built at a 45° angle from the vertical direction of the image..The flag holes are ~250 microns in diameter and the leading edge film cooling rods are ~450 microns in diameter.

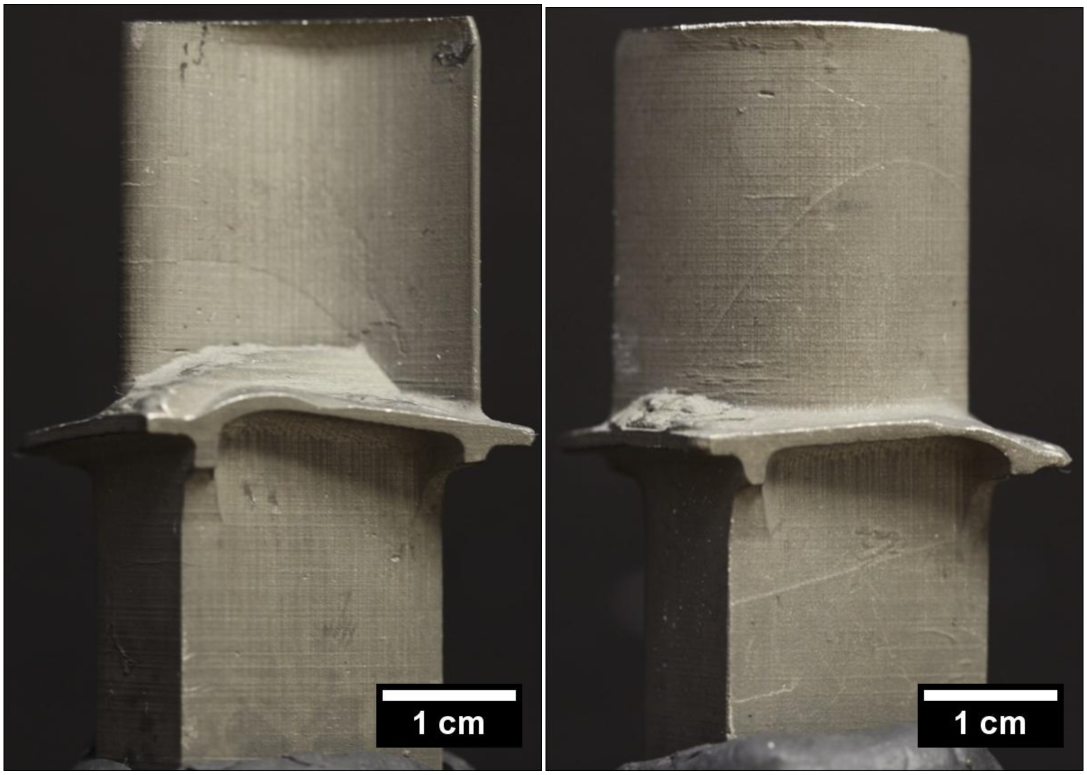

Figure 1.11 Single-crystal Ni-superalloy airfoils cast from LAMP molds. These are solid (uncored) airfoils.

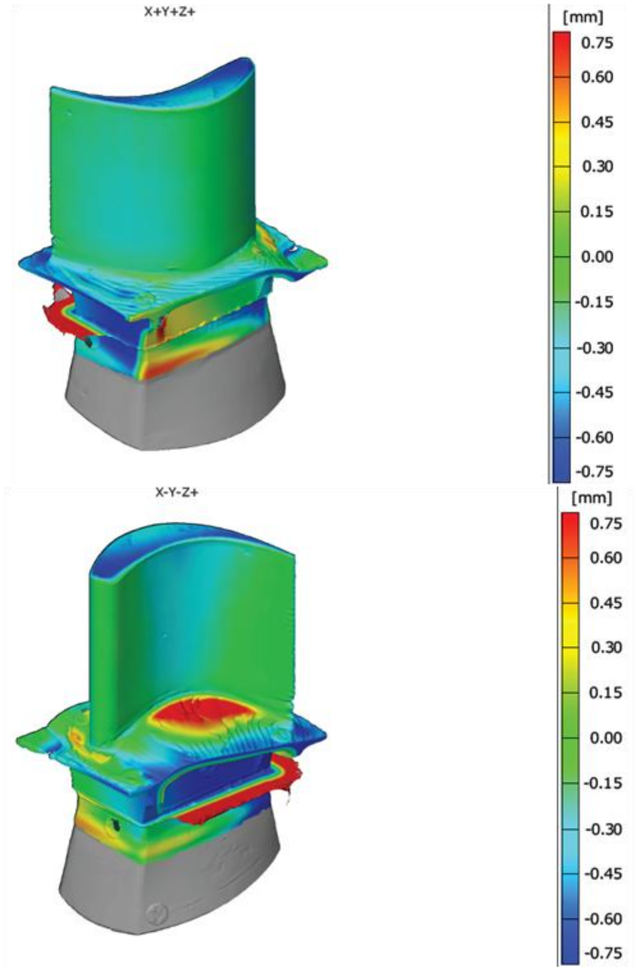

Figure 1.12 White light imaging of LAMP produced airfoil. Dimensional tolerance was not scaled to LAMP shrinkage, so only relative distortion is useful.

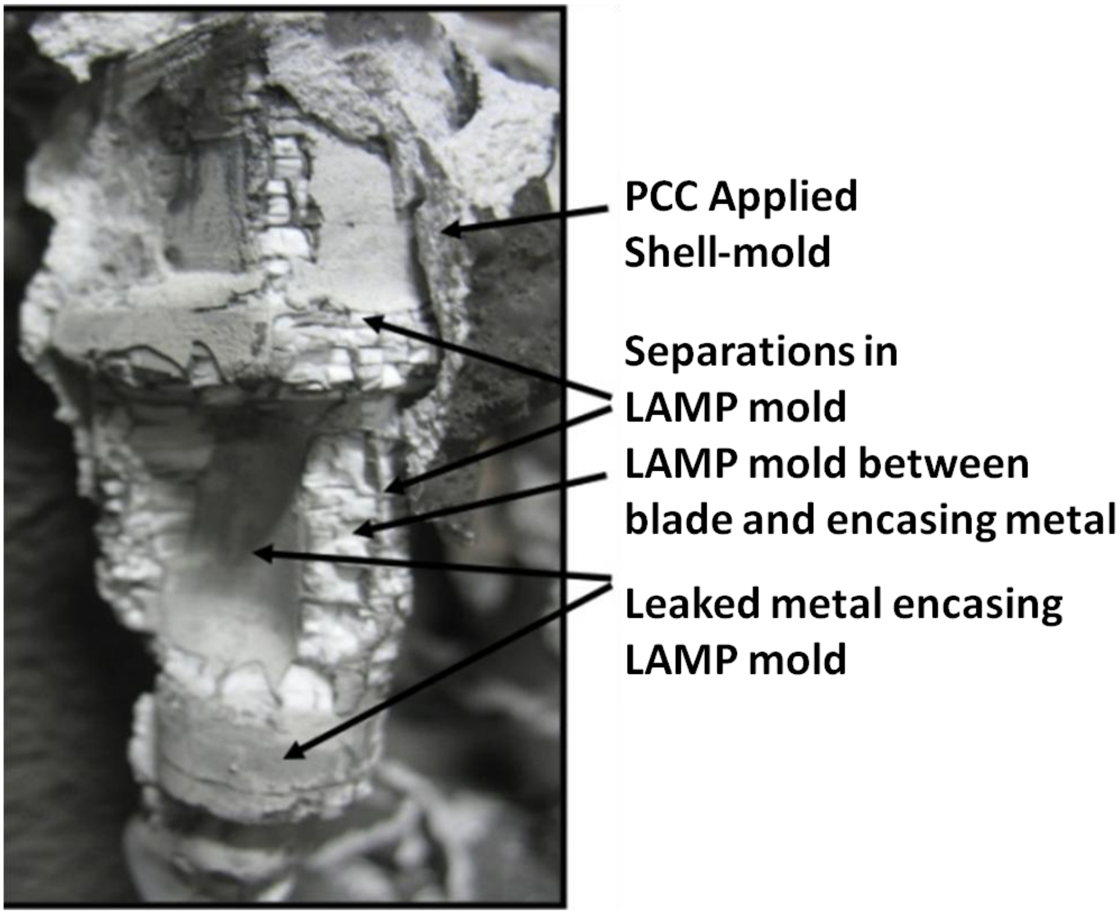

Figure 1.13 Results of initial attempt at casting single crystal in LAMP molds. The LAMP mold shrank and cracked at high temperature.

Chapter 2
The Kinetics of Cristobalite Formation in Sintered Silica

2.1 Preface

Cristobalite was determined to be the only available means of managing the high temperature creep and sintering behavior of sintered silica LAMP molds. In order to use cristobalite content for this purpose its formation must be understood and controlled. Transformation kinetics were studied and a time-temperature-transformation (TTT) plot was constructed for the sintered silica used in LAMP. [The following chapter in press, forthcoming volume of the Journal of the American Ceramic Society]

2.2 Introduction

Amorphous silica is widely used as a high temperature glass, electrical insulator, optical material, and refractory. In many silica applications it is crucial to control the transformation to cristobalite. Cristobalite formation sets the upper temperature bound for use of fused silica glassware; whereas, in glass ceramics and silica refractories, the formation of cristobalite is a vital part of processing. The devitrification of amorphous silica to cristobalite has a long history of study in many contexts. Research on the transformation to cristobalite in bulk glasses was conducted by Ainslie et al[1] in 1962 and by Wagstaff and Richards[2] in 1965. Cristobalite formation in gels was studied by Verduch[3] in 1962 and by Chao and Lu[4] in 2000. The transformation in powdered and sintered silica was studied by Wang and Hon[5] in 1995, Li et al[6] in 2008, and Kazemi et al[7] in 2013. Despite being studied in many contexts and forms across several decades the transformation of amorphous silica to cristobalite remains less defined and quantified than many silica derived glass ceramics. Perhaps this arises from the sensitivity of the system to impurities. It was noted by Wagstaff and Richards,[8] and many since,[9, 10, 11] that the devitrification of amorphous silica is sensitive to moisture in the air and trace impurities. In this study we have examined the cristobalite transformation in a 99.7% pure, commercial refractory silica powder. As this material is an industrial silica, we expect that the behavior will differ from purer laboratory and electronics grade silica. Indeed, it was found that this material has faster transformation kinetics than any reported pure silica but slower transformation kinetics than reported for doped glass systems.

We collected data for the degree of crystallization vs. annealing time and temperature for sintered silica powder. At temperatures between 1200-1350^{o}C, the porosity and surface area did not change during the crystallization anneal. The results could be fit to an expression based on the the Johnson-Mehl-Avrami-Kolmogorov model, JMAK, and this was used to construct Time Temperature Transformation or TTT diagrams. For this temperature range, the TTT diagram is linear, as it represents the low temperature leg of the full TTT diagram. At higher temperatures there is a maximum crystallization rate, corresponding to the “nose” of the TTT diagram. We were able to explore the transformation rate around the nose with a set of experiments from 1400-1650^{o}C, but in this range, the amorphous silica sintered and densified concurrently with crystallization, which complicates the analysis[12, 13]. The effect of seeding amorphous silica powders with powdered cristobalite was studied by comparison of crystallization kinetics in seeded and unseeded silica powders. The effectiveness of seeding with powder cristobalite was also compared to the effect of residual quartz in incompletely amorphized silica glass powder.

2.3 Procedure:

2.3.1 Materials:

Sintered silica ceramics were prepared with commercially available industrial silica of 99.7% purity with 5% residual quartz content, (TECO-Sphere-Microdust, CE Minerals, Greeneville, TN). The predominant impurities are 2000 ppm alumina and 250 ppm iron oxide. Calcium, Magnesium, Sodium, and Potassium oxides are present in concentrations of less than 50 ppm each. As determined by dynamic light scattering with a Microtrac X-100, mean particle size by volume is 10.3 µm, the D10 2.5 µm, the D50 6.7 µm, and the D90 22.0 µm. The powder is largely composed of 5-25 micron spheriodized particles with a small volume fraction of irregular, fine particles under 0.5 micron. This silica powder is spheroidized by a drop furnace process, in which ground quartz powder is dropped through a hot furnace which heats it to melting. This simultaneously transforms the crystalline quartz starting material to amorphous silica while causing particles to adopt a spherical shape. The quartz content is remnant crystallinity due to incomplete amorphization during the process. The crystalline content and phase were verified by X-ray Diffraction.

For the powder comparison study a fully amorphous silica powder was used (TECO-Sphere-A, CE Minerals, Greeneville, TN). The fully amorphous powder of 99.7% purity (TECO-Sphere-A) was compared to the material with 5% residual quartz (TECO-Sphere-Microdust). The fully amorphous powder has a similar size distribution, with the mean particle size by volume is 7.45 µm, the D10 2.2 µm, the D50 4.64 µm, and the D90 16.0 μm. This fully amorphous powder is also spheriodized by a drop furnace process, but it differs in that the starting material is amorphous silica powder rather than crystalline ground quartz powder. For the seeding experiment, samples of both the fully amorphous and residual quartz powder were produced with 10 wt% cristobalite powder (Goresil, CE Minerals, Greeneville, TN) to act as a seed.

2.3.2 Annealing

Samples were dry-pressed in a 25 mm die under an axial loading of 30 MPa. For the lower temperature, constant surface area study, the as-pressed pellets were annealed on an alumina plate for 0.5 to 24 hours at 1200 to 1350°C in a box furnace under lab air with humidity ranging from 15-60% relative humidity. Furnace ramp rates of 20°C/min on heating and 15°C/min on cooling were used. Note that these ramp rates place samples in the transformation range for 5-10 minutes, which is short compared to the annealing time. Temperatures reported are the furnace set point temperatures, and the furnace temperature readings have been verified by external thermocouple measurements to be accurate within ±7°C. The density of sintered samples were found by the Archimedes method, (ASTM C-373-88), to have 78-86% full density and corresponding open porosity of 14-22% with no closed porosity.

For the higher temperature study, in which concurrent densification was significant, the samples were briefly inserted and then removed from a furnace. These samples were lightly annealed at 1100°C to develop sufficient strength for handling but not form any cristobalite. The samples were then cut into bars of 3 mm thickness, 6 mm width, and length of 10-30 mm. These bars were suspended by a platinum wire in a furnace held at 1400-1650°C for 5 or 10 minutes. Densification of these samples varied significantly reaching nearly full density for samples sintered at 1550°C and above. As with the lower temperature samples the porosities were found by the Archimedes method. The open porosity after 10 minutes at 1450°C was found to be 8%, after 5 minutes at 1550°C it was found to be 1.1%, and after 5 minutes at 1600°C it was found to be 0.5%.

Transformation kinetics were studied for samples annealed at 1200°C to 1350°C with a 25°C step size between temperatures. The lower temperature limit of collected data in this study was chosen as a matter of practicality. At 1200°C, after a 30 hour isothermal hold, samples were found to have a 0.23±0.02 cristobalite fraction. The upper limit of 1350°C was found to be the highest temperature at which concurrent sintering during crystallization was not a concern. For all samples sintering occurred during the anneal. For samples annealed at 1350°C and below this sintering did not significantly impact the surface area of the powder. Samples sintered at 1400°C and above had significant densification which impacts the surface area of the material and the crystallization kinetics.

To obtain the isothermal transformation kinetics,[14] hold times at the reported temperature far exceeded time spent ramping to temperature or equilibrating at temperature. For samples annealed at 1350°C and below, the sample was inserted at room temperature and heated. Samples were exposed to temperatures in the transformation range for a short time relative to the isothermal hold. For samples annealed at 1400°C and above the sample was inserted into the furnace at temperature. For these temperatures, based on sample dimensions and the thermal diffusivity of amorphous silica the estimated time for temperature to equilibrate is on the order of 10 seconds, which is short relative to the hold times of 5 and 10 minutes.

2.3.3 Determination of Cristobalite Fraction

Following annealing, the fraction transformed was determined by means of quantitative powder x-ray diffraction (QXRD). As amorphous silica has no Bragg peak, we used 20 wt.% TiO_2 anatase as an internal standard. Powder patterns were collected on a Rigaku Rotaflex with CuKα radiation operating at 40 kV and 100 mA. The scanning step size was 0.02 degrees and scan speed 3 seconds per step. Scans were conducted from 18.5 to 28.5 degrees. The (101) peak of cristobalite at 22° was compared to the (101) peak of the anatase at 25.3°, both being the primary diffraction peak of their compound.

To construct a standard, samples of pure cristobalite devitrified from the powder were mixed with untransformed starting material in known quantities. The pure cristobalite standard was produced by the method of Wang and Hon: 24 hour anneal at 1550°C followed by grinding, a 12 hour 1550°C anneal followed by grinding, and then a final 12 hour 1550°C anneal.[5] These standards were mixed with 20 wt% anatase and measured by QXRD. The relative integrated intensities of the cristobalite and anatase signals were used to construct a calibration curve against which all samples were measured. The XRD scan to scan variation in measured cristobalite content of the same sample was found to be 1% between 20-80% cristobalite content and up to 5% for cristobalite contents outside this range.

All samples were run in duplicate to minimize the effect of sample-to-sample variation. Two samples were simultaneously annealed and were separately ground and prepared for XRD. The cristobalite content produced from the XRD results was then averaged to produce the reported value. For simultaneously annealed samples, cristobalite content was found to vary by 0-8%, with an average variation of 2%. The largest deviations were seen for cristobalite contents less than 20% or greater than 80%. For cristobalite content between 20-80% the variation was found be ≤ 2%.

2.4 Results:

2.4.1 Transformation and Data Analysis

A typical XRD pattern can be seen in Figure 2.1. For this example, the sample was annealed at 1325°C for 45 minutes and the cristobalite fraction was 0.21±0.02. Note the anatase (101) standard peak at 25.3°, the cristobalite (101) peak rising from the amorphous background at 22°, and the residual quartz peak (011) at 26.7°. The quartz content was not quantified by a comparison to an established standard; however, it was observed in the raw powder to be compatible with the manufacturer's value of 5% by the standard established for cristobalite. Quartz content was observed to decrease from its initial value to that of background noise as samples exceeded 80% cristobalite content.

Figure 2.2 shows the complete data set for the constant-porosity series as degree of transformation to cristobalite over the isothermal hold time at various temperatures. The lines seen in Figure 2.2 are arbitrary and placed only to guide the eye. At 1500°C 50% transformation to cristobalite was achieved in 10 minutes, while at 1200°C only 27% transformation was observed after 30 hours.

For samples annealed from 1200°C to 1350°C, the degree of densification was minimal, and this transformation data was fit to an expression of the form of the Johnson-Mehl-Avrami-Kolmogorov equation:

$$Y = 1 - e^{-K(t)^n} \quad Eq. 1.1$$

in which *Y* is fraction of cristobalite, *t* is time in minutes, *K* the kinetic constant, and *n* the time exponent.[14, 15, 16]

The two unknowns, *K* and *n*, are extracted from the data. For each temperature the averaged cristobalite content was used to plot the linearized form of Equation 1.1: ln ln (1/(1-Y)) vs ln(t). This can be seen in Figure 2.3. Plotted in this way the slope of a linear fit to the data provides the value for *n*, while the intercept provides the value of ln (*K)*. The data at each temperature consisted of as few as 3 data points, which limits the accuracy with which slope can be determined. To account for this, a composite plot was produced by shifting the data from each temperature along the x-axis by its x-intercept, seen in Figure 2.4. It was observed that this composite data set fit a single slope with greater accuracy than the individual slopes found at each temperature. From this composite plot it was found the data fit a single n value of $n=3.0 \pm 0.6$ with error determined by residual sum of squares. Here we are using the Avarami exponent as a fitting parameter and do not seek to interpret its values in terms of mechanism[16] or address crystallization at particle surfaces.[17, 18]

Linear fits were then made for the data at each individual temperature using the n value determined from the composite plot, as seen in Figure 2.3. The ln(K) values, seen below in Table 2.1, were determined from the plots. Using these n and K values with Eq. 1.1, we calculated the time required to achieve cristobalite fraction of 0.1, 0.5, and 0.9 and plotted the results in the format of a TTT diagram in Figure 2.5. This constant porosity series represents the low temperature leg of the TTT diagram, and appears to be linear.

For the transformation data in Figure 2.5, the kinetic constant K can be expressed in Arrhenius form in order to find the apparent activation energy, Q for this low temperature leg:

$$K = A\mathrm{e}^{(-\mathrm{Q/RT}\ )} \qquad Eq.1.2$$

where A is the pre-exponential term, R is the universal gas constant, and Q is the activation energy in J/mol. Recall that for a phase transformation the activation energy involves the enthalpy of the transformation and the activation energies of the transport process. Figure 2.6 displays ln(K) vs 1/T, which has a slope of Q/R. From Figure 2.6 an apparent activation energy of 555±24 kJ/mol is derived, where the uncertainty range is inferred from the residual sum of squares. The preexponential term A, inferred from regression of Figure 2.6, is approximately A=exp(-36.7)=4.7 x 10^{-17}. From this we can represent the kinetic constant that fits these data as:

$$K = (4.7 \text{ x } 10^{-17})e^{-555\frac{kJ}{mol}/RT} \qquad Eq.1.3$$

The low temperature data can be described by:

$$Y = 1 - \exp\left((4.7 \text{ x } 10^{-17})e^{-555\frac{kJ}{mol}/RT}(t)^3\right) \qquad Eq.1.4$$

This expression was used to calculate the lines seen in Figure 2.5. This provides a good fit to the values calculated for each temperature observed in this study. The constants in Eq.1.4 were determined from the data collected at all temperatures, and are, therefore, less sensitive to the observed experimental variation than the smaller individual temperature data sets.

The points in Figure 2.5 for the Y_{10}, Y_{50}, and Y_{90} use the isothermal values from Eq.1.4 to interpolate from the measured Y(t) values. Most of the directly measured data, as seen in Figure 2.2, do not exactly fall at transformation fractions of 0.1, 0.5, or 0.9 cristobalite content. However, two measurements did come within experimental variation of 50% transformation allowing comparison to the Eq.1.4 values. These two points, seen in Figure 2.2, are 53±2% after 180 minutes at 1275°C, and 49±2% after 60 minutes at 1325°C. The 50% TTT line from Eq.1.4 predicts t_{50}=216 minutes at 1275°C, and 56 minutes at 1325°C.

This TTT diagram, Figure 2.5, does not have the typical TTT "nose." This is because these temperatures fall far below the melting point of 1713°C; so the displayed range falls entirely in the low-temperature leg of the TTT curve. The location of the nose can be determined from the data at temperatures from 1450-1600°C. The direct observations in this range are plotted as degree of transformation by temperature in Figure 2.7. The temperature of maximum crystallization rate falls between 1500 and 1550°C. The specimens sintered rapidly at 1550°C and fully densified during the anneal. This would be expected to reduce crystallization rate as cristobalite is known to surface nucleate, so these higher temperature data for more densely sintered silica may not be directly comparable to the lower temperature data for porous silica. However, we have added the higher temperature direction observations falling near Y=0.1 in Figure 2.8, and they appear to agree with the lower temperature data. This allows us to estimate a more complete TTT diagram including the nose around 1550°C and cristobalite melting temperature of 1713°C.[19]

2.4.2 Seeding

Silica powder seeded with cristobalite was evaluated and compared to unseeded powder silica with and without residual quartz. A fully amorphous silica powder similar to the powder used in the previously discussed TTT study, but containing no residual quartz, was used as a comparison to evaluate the impact of the residual quartz on transformation. The effect of residual quartz content and cristobalite seeding was compared for: (1) a fully amorphous powder with no seed (2) a fully amorphous powder with 10 wt% cristobalite added (3) a powder with 5 % residual quartz (4) a powder with 5% residual quartz with 10 wt% cristobalite added. Formulations are summarized in Table 2.2.

A comparison of the cristobalite fraction after 1 hour at various temperatures for the 4 powders can be seen in Figure 2.9. For ease of comparison, a chart showing the temperature at which a given formulation achieved 0.5 cristobalite fraction after a 1 hour hold is shown in Figure 2.10. As expected, fully amorphous powder without cristobalite seed requires the highest temperature to transform in a 1 hour anneal. It can be seen that the temperature at which the sample transforms after a 1 hour hold is lowered in fully amorphous silica powder by the addition of cristobalite powder. This is also unsurprising, as it is expected that the crystalline powder will seed devitrification. The temperature at which the sample transforms after a 1 hours hold is even lower in the powder with residual quartz than in fully amorphous powder seeded with cristobalite. The residual quartz crystal has a larger impact on lowering the transformation temperature than seeding with cristobalite powder. For the mixed case, in which powder with residual quartz was seeded with cristobalite, the behavior was identical to unseeded powder. It should be noted that crystalline contents were measured by XRD and no confusion between quartz and cristobalite was possible. The quartz content was only observed to decrease, never increase, during devitrification to cristobalite.

2.4.3 Microstructure of Cristobalite

Nucleation of cristobalite on the surface of the particles is suggested by the microstructure. Polished sections were prepared from epoxy-impregnated specimens polished to a 0.05 micron finish. Images were collected on Phillips XL30 scanning electron microscope with a field emission gun electron source.

Figure 2.11 A-D shows backscattered electron (BSE) imaging of samples with 11, 25, 55, and 84% cristobalite. These samples fall in the 1200-1350°C range of minimal densification with relatively constant surface area. Using electron backscatter imaging the small density difference between the amorphous and crystalline state provides contrast, in that the cristobalite is slightly darker. The presence of a cristobalite layer can also be inferred from the pattern of micro-cracks in the surface layer of the larger particles. This cracking occurs during the transformation from the high-temperature β-cristobalite phase to the low-temperature α-cristobalite phase upon cooling below 250°C.[20] In a partially crystalline particle, stress will develop when the volume change associated with the β-α transformation is constrained by the static amorphous region. As seen in Figure 2.11 over the course of transformation, cristobalite forms a shell layer around the still amorphous core. This is the expected behavior as it is widely known that cristobalite preferentially nucleates at the surface.[3, 8, 21] This being a powder sample, cristobalite has apparently nucleated at the internal free surfaces and progressed inward from the particle surface leaving an amorphous core. The micro-cracks pass through the cristobalite shell region and terminate at the amorphous-crystalline interface. A schematic illustration of this core-shell morphology follows in Figure 2.12.

Figure 2.13 shows a sample with 41% cristobalite sintered at 1550°C which sintered to high density after only a 10 minute anneal. Cracked particles of the same 5-50 micron scale, similar to the larger spheres from the powder, can be seen embedded in a matrix. The area fraction of these embedded fractured particles matches that of the fraction cristobalite observed by XRD.

2.5 Discussion:

2.5.1 Comparison to Prior Work

The transformation behavior observed in this study can be compared to various published results, seen in Figure 2.14. The published kinetic data these studies in several silica systems were used to plot Y=0.5 values in the format of a TTT diagram. The direct observation of Y=0.48 observed after 10 minutes at 1500°C is plotted as well. The wide range of the transformation behavior is immediately apparent. High purity amorphous silica transforms at the highest temperatures over the longest times.[6] Less pure refractory grade commercial silica powder, comparable in purity to the powder used in this study, transforms over shorter times and can be accelerated by seeding with cristobalite to transform even more quickly.[5] The powder used in this study can be seen to transform at even shorter times. This corroborates the findings of the powder comparison study in which purely amorphous silica seeded with cristobalite had slower transformation than silica with residual quartz. Doped silica systems such as borosilicate glass and NaO_2 doped silica are found to transform at lower times and temperatures.[4, 22] Among the studies of nominally pure SiO_2 systems we then see a progression, where the slowest kinetics belong to the purest material. Overall, we observed that lower purity accelerates the transformation, cristobalite seeding accelerates the transformation further, and indicated in this study, residual quartz crystallinity accelerates the transformation still further. We see the powder with residual quartz possesses the fastest transformation kinetics of nominal pure SiO_2 systems, but is slower than doped silica based systems.

2.5.2 Concurrent Densification and the Temperature of Maximum Transformation Rate

The apparent “nose” of the TTT diagram, or the temperature of maximum transformation rate, was observed to fall between 1500-1550°C. However, the kinetics of crystallization at the observed nose are complicated by concurrent sintering densification during crystallization. Concurrent crystallization and sintering can be a complex phenomena common in glass powders, which has been previously reported on by Prado et al.[12, 13] In the present study it was observed that the samples annealed above 1400°C densified to a far greater extent than those annealed at lower temperatures. In a surface nucleating crystallization process such as the current study this can potentially have a large impact on the kinetics of the reaction by reducing the number of nucleation sites available. In particular, at temperatures of 1550°C and above the samples were observed to densify into a dense glass with closed porosity. It is unclear from the present study whether this densification impacted the apparent transformation rate. It is possible that at temperatures at which sintering densification occurs rapidly the kinetics are slowed due to a reduction in the available number of nucleation sites as the surface area decreases.

2.5.3 Seeding and Residual Quartz Effect

As illustrated in Figure 2.9 and 2.10, the temperature at which a sample crystallized in a 1 hour anneal was lowered by seeding with cristobalite, but lowered more by use of a powder with residual quartz. The effect is prominent when one looks at the temperature at which the material passes the 50% cristobalite conversion mark in a 1 hour anneal. Seeding with cristobalite has a dramatic effect, lowering the temperature to pass 50% conversion by 90°C. However, powder with residual quartz shows an even more dramatic decrease of 150°C for 50% conversion in a 1 hour anneal. Further, in material with residual quartz crystallinity, the addition of cristobalite powder had no effect on transformation. This behavior is unexpected. The apparent conclusion is that, paradoxically, residual quartz is more effective at accelerating the formation of cristobalite than the addition of cristobalite seed powder. Additionally, the effect of the residual quartz is such that the further addition of cristobalite powder has no observed effect.

It is surprising to find quartz accelerating the transformation to cristobalite to a greater degree than cristobalite. However, the details of the system must be remembered. Seed cristobalite is crystalline powder mechanically mixed with amorphous silica powder. One expects cristobalite-silica contact to be very limited in such a system. On the other hand, residual quartz is presumably retained within the silica particles as an unmelted fraction from the drop-furnace process. This presents the possibility that the observed behavior arises from differences in the distribution of the cristobalite seed and residual quartz rather than the relative potency of quartz and cristobalite in accelerating crystallization. For example, the quartz retained in the silica particles may be acting as a heterogeneous nucleation site for cristobalite formation. A study comparing powders incompletely amorphized from cristobalite starting material may shed more light on this behavior. It is not known by what mechanism residual quartz crystal accelerates the formation of cristobalite, but given the significant effect further study is warranted.

2.5.4 Residual Quartz as a Nucleation Site

The ability of residual quartz content to catalyze the formation of cristobalite may be due to residual quartz crystals acting as heterogeneous nucleation sites within the silica particles. This possibility was explored by use of TEM to locate quartz in partially crystalline material and observed whether it served as a nucleation cite for cristobalite formation. Locating quartz surrounded by cristobalite in turn surrounded by amorphous silica would strongly suggest quartz was acting as a nucleation site. Unfortunately, no such conclusive results were found. Finely ground partially crystalline sintered powder was examined on a JEOL 3011 high resolution electron microscope. Quartz was observed and a High Resolution TEM (HRTEM) micrograph appears in Figure 2.15. Its structure was confirmed to be α-quartz viewed along the 211 zone axis by select area electron diffraction (SAED) patterns which match the predicted pattern for α-quartz viewed along the 211 axis, observed and simulated SAED appear in Figure 2.16. However, it was not possible to observed cristobalite under TEM, preventing the confirmation of nucleation at the quartz inclusion. Cristobalite is widely known to amorphize very quickly under a TEM electron beam.[23, 24, 25] In practice it was found to be possible to bring cristobalite into focus for slightly less than a second before it completely amorphized. In this short time it was not possible to collect SAED or well focused images. The rapid amorphization of cristobalite prevented the determination of quartz's role in crystallization.

2.6 Conclusions:

The degree of transformation (Y) of sintered silica glass powder to cristobalite, annealed at 1200°C-1350°C under conditions where the porosity was constant, can be represented by an expression of the form: $Y = 1 - \exp\left((4.7\text{ x }10^{-17})e^{-555\frac{kJ}{mol}/RT}(t)^3\right)$.

Short anneals at 1400-1650°C showed that the temperature of maximum transformation rate was between 1500-1550°C. At these higher temperatures, the powder densified by sintering, but the transformation kinetics agreed with the lower temperature kinetics extrapolated to 1400°C

Seeding of fully amorphous silica powders with cristobalite powder lowers the temperature required to transform the material. Residual quartz from incompletely amorphized silica also lowers the transformation temperature to a larger extent than cristobalite seeding.

2.7 References

1. N. G. Ainslie, C. R. Morelock, and D. Turnbull, "Devitrification Kinetics of Fused Silica," in Symposium on Nucleation and Crystallization in Glasses and Melts.
2. F. E. Wagstaff and K. J. Richards, "Preparation and Crystallization Behavior of Oxygen Deficient Vitreous Silica," *Journal of the American Ceramic Society,* 48[7] 382-& (1965).
3. A. G. Verduch, "Kinetics of Cristobalite Formation from Silicic Acid," *Journal of the American Ceramic Society,* 41[11] 427-32 (1958).
4. C. H. Chao and H. Y. Lu, "Crystallization of Na2O-doped colloidal gel-derived silica," *Mater. Sci. Eng. A-Struct. Mater. Prop. Microstruct. Process.,* 282[1-2] 123-30 (2000).
5. L. Y. Wang and M. H. Hon, "The effect of Cristobalite Seed on the Crystallization of Fused Silica Based Ceramic Core- A Kinetic Study," *Ceram. Int.,* 21[3] 187-93 (1995).
6. X. M. Li, X. W. Yin, L. T. Zhang, and S. S. He, "The devitrification kinetics of silica powder heat-treated in different conditions," *J. Non-Cryst. Solids,* 354[28] 3254-59 (2008).
7. A. Kazemi, M. A. Faghihi-Sani, and H. R. Alizadeh, "Investigation on cristobalite crystallization in silica-based ceramic cores for investment casting," *J. Eur. Ceram. Soc.,* 33[15-16] 3397-402 (2013).
8. F. E. Wagstaff and K. J. Richards, "Kinetics of Crystallization of Stoichiometric SiO2 Glass in H2O Atomospheres," *Journal of the American Ceramic Society,* 49[3] 118-& (1966).

9. T. Honma, N. Tamura, K. Saito, and E. Sekiya, "Difference in Structural Relaxation Times of Inner Surface and Inner Bulk Region of Silica Glass Arc Tube," *New Journal of Glass and Ceramics* 48-52 (2013).
10. E. Opila, "Influence of Alumina Reaction Tube Impurities on the Oxidation of Chemically-Vapor-Deposited Silicon-Carbide," *Journal of the American Ceramic Society,* 78[4] 1107-10 (1995).
11. P. P. Bihuniak, "Effect of Trace Impurities on Devitrification of Vitreous Silica," *Journal of the American Ceramic Society,* 66[10] C188-C89 (1983).
12. M. O. Prado, M. L. F. Nascimento, and E. D. Zanotto, "On the sinterability of crystallizing glass powders," *J. Non-Cryst. Solids*, 354[40-41] 4589-97 (2008).
13. M. O. Prado and E. D. Zanotto, "Glass sintering with concurrent crystallization," *C. R. Chim.*, 5[11] 773-86 (2002).
14. M. Avrami, "Kinetics of phase change I - General theory," *J. Chem. Phys.*, 7[12] 1103-12 (1939).
15. W. A. Johnson and R. F. Mehl, "Reaction kinetics in processes of nucleation and growth," *Trans. Am. Inst. Min. Metall. Eng.*, 135 416-42 (1939).
16. M. C. Weinberg, D. P. Birnie, and V. A. Shneidman, "Crystallization kinetics and the JMAK equation," *J. Non-Cryst. Solids,* 219 89-99 (1997).
17. I. Gutzow, R. Pascova, A. Karamanov, and J. Schmelzer, "The kinetics of surface induced sinter crystallization and the formation of glass-ceramic materials," *J. Mater. Sci.*, 33[21] 5265-73 (1998).
18. A. Karamanov, I. Avramov, L. Arrizza, R. Pascova, and I. Gutzow, "Variation of Avrami parameter during non-isothermal surface crystallization of glass powders with different sizes," *J. Non-Cryst. Solids,* 358[12-13] 1486-90 (2012).
19. W. A. Deer, R. A. Howie, and J. Zussman, "An Introduction to the Rock Forming Minerals." Logman, (1966).
20. D. R. Peacor, "High-temperature Single Crystal Study of Cristobalite Inversion," *Z. Kristall.,* 138 274-98 (1973).
21. F. E. Wagstaff, "Crystallization Kinetics of Internally Nucleated Vitreous Silica," *Journal of the American Ceramic Society,* 51[8] 449-& (1968).
22. J. H. Jean and T. K. Gupta, "Crystallization Kinetics of Binary Borosilicate Glass Composite," *J. Mater. Res.*, 7[11] 3103-11 (1992).
23. R. L. Withers, T. R. Welberry, G. L. Hua, J. G. Thompson, and B. G. Hyde, "A Transmission Electron-Microscopy Study of Cristobalite," *Phase Transitions,* 16 41-45 (1989).
24. R. L. Withers, J. G. Thompson, and T. R. Welberry, "The Structure and Microstructure of Alpha-Cristobalite and its Relationship to Beta-Cristobalite," *Physics and Chemistry of Minerals,* 16[6] 517-23 (1989).
25. E. S. Thomas, J. G. Thompson, R. L. Withers, M. Sterns, Y. H. Xiao, and R. J. Kirkpatrick, "Further Investigation of the Stabilization of Beta-Cristobalite," *Journal of the American Ceramic Society,* 77[1] 49-56 (1994).

Table 2.1 Derived JMAK Constants

T ±7 C	N	K	Ln K
1200	3.0±0.6	0.00038	-7.9
1250	3.0±0.6	0.0022	-6.1
1275	3.0±0.6	0.0048	-5.3
1300	3.0±0.6	0.0091	-4.7
1325	3.0±0.6	0.015	-4.2
1350	3.0±0.6	0.026	-3.7

Table 2.2 Formulations Used in Powder Comparison Study

Formulation	Fully Amorphous Powder (TECO-Sphere-A)	Residual Quartz Powder (TECO-Sphere-Microdust)	Cristobalite Powder (Goresil)
1	100 wt%		
2	90 wt%		10 wt%
3		100 wt%	
4		90 wt%	10 wt%

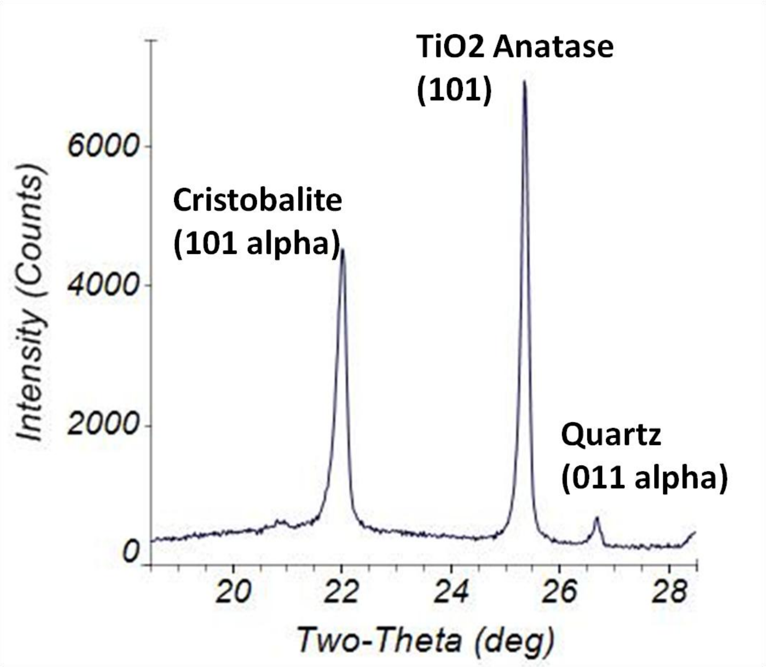

Figure 2.1 Typical XRD Scan. Showing cristobalite, anatase, and quartz peaks. Cristobalite content found to be 21 ± 2% following a 45 minute hold at 1325°C.

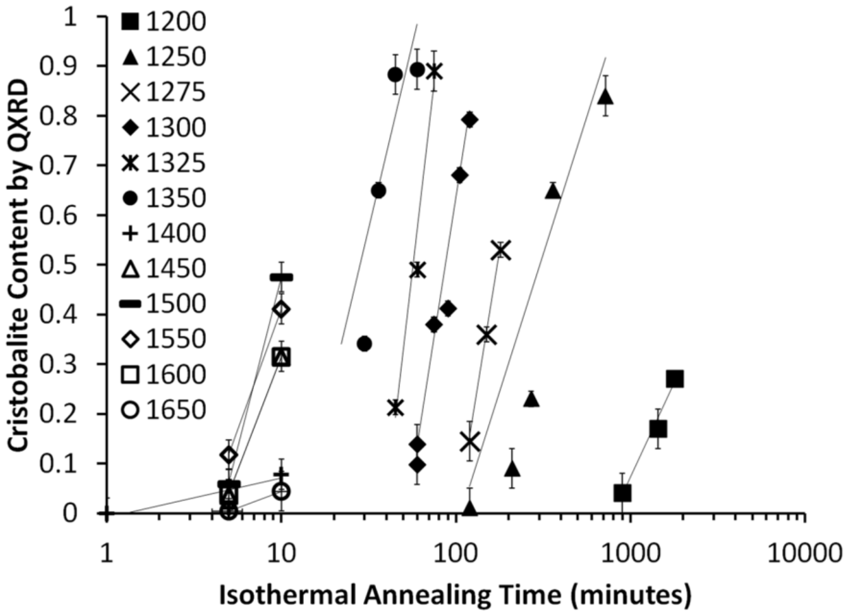

Figure 2.2 Cristobalite content obtained by QXRD vs isothermal hold time. (Linear fits plotted as visual guide only.)

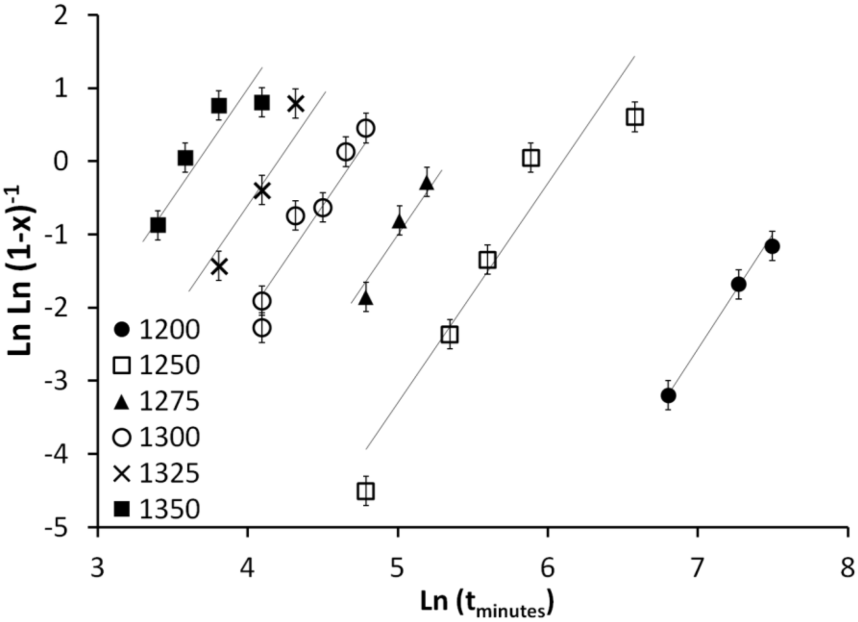

Figure 2.3 Transformation data plotted as the linearized form of the JMAK equation, along with linear fits using an Avrami exponent of n = 3.

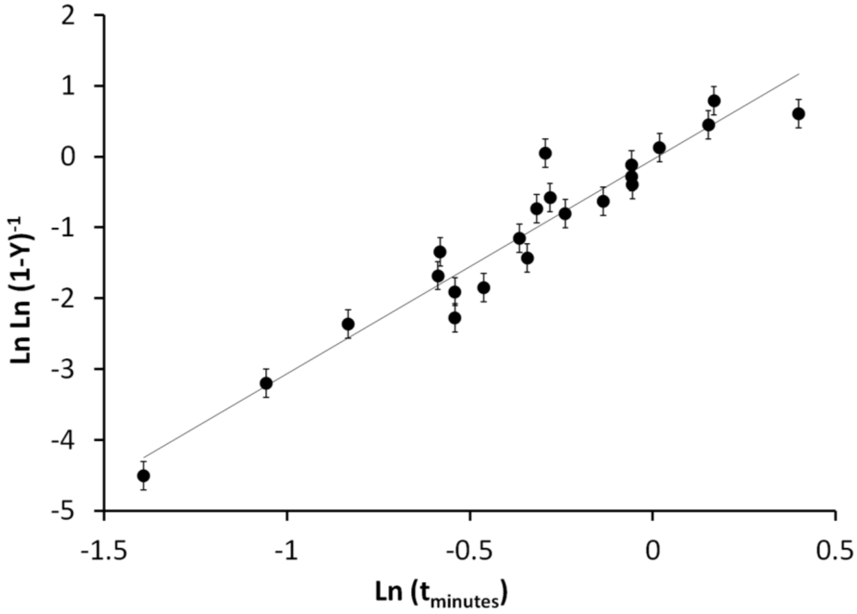

Figure 2.4 Composite plot of the transformation data plotted as linearized form of the JMAK equation. Data from individual temperatures shifted on ln($t_{minutes}$)-axis. Data found to fit a single slope of Avrami constant n = 3.

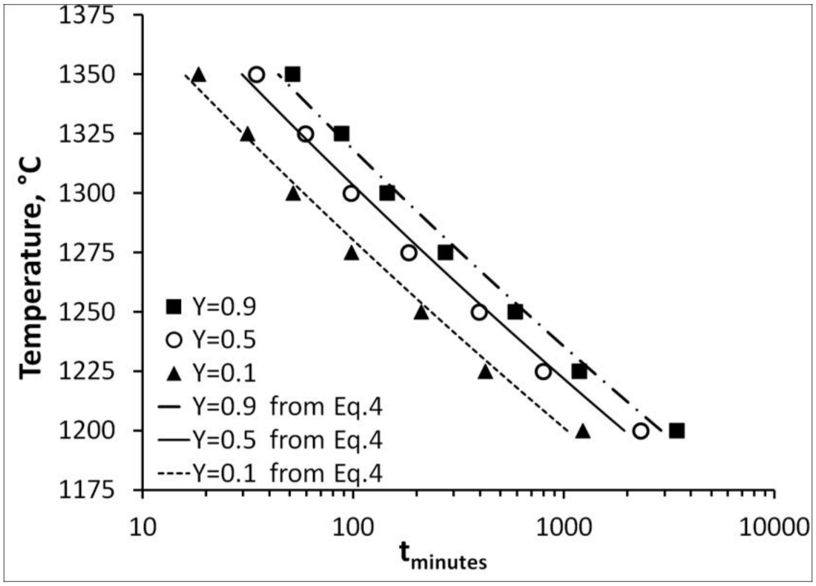

Figure 2.5 Time-Temperature Transformation (TTT) plot for Y 10%, Y 50%, and Y 90%. Individual points are interpolated using JMAK from collected data at each temperature. Lines are plotted from Equation 1.4, calculated from the JMAK equation using the constants inferred from the data.

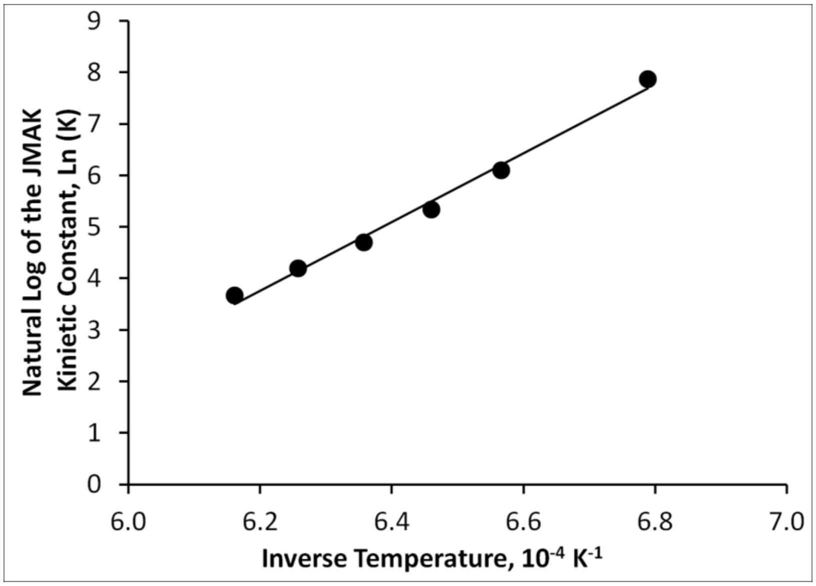

Figure 2.6 Arhennius plot of JMAK kinetic constant K vs inverse temperature.

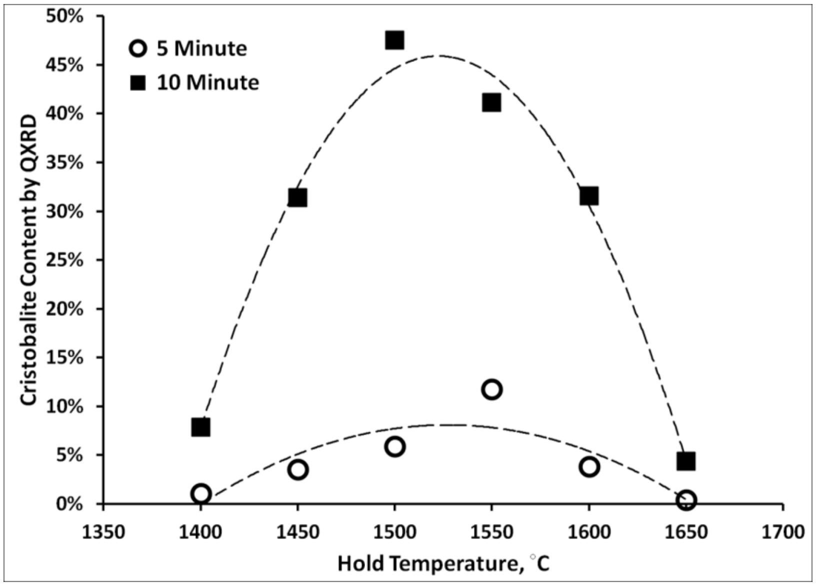

Figure 2.7 Brief annealing times at 1400-1650°C illustrate the temperature of maximum crystallization rate or "Nose" of the TTT. (Dashed lines are for visual guide only.)

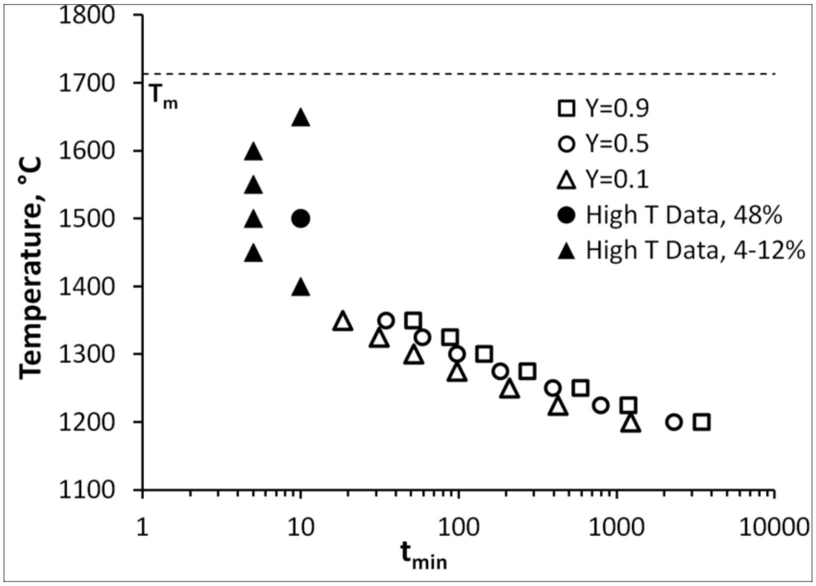

Figure 2.8 Combination plot of 10, 50, 90 % transformation interpolated from collected data from 1200-1350°C and direct observations near 10% and 50% collected at high temperature. Combination plot of 10, 50, 90 % transformation interpolated from collected data from 1200-1350°C and direct observations near 10% and 50% collected at high temperature.

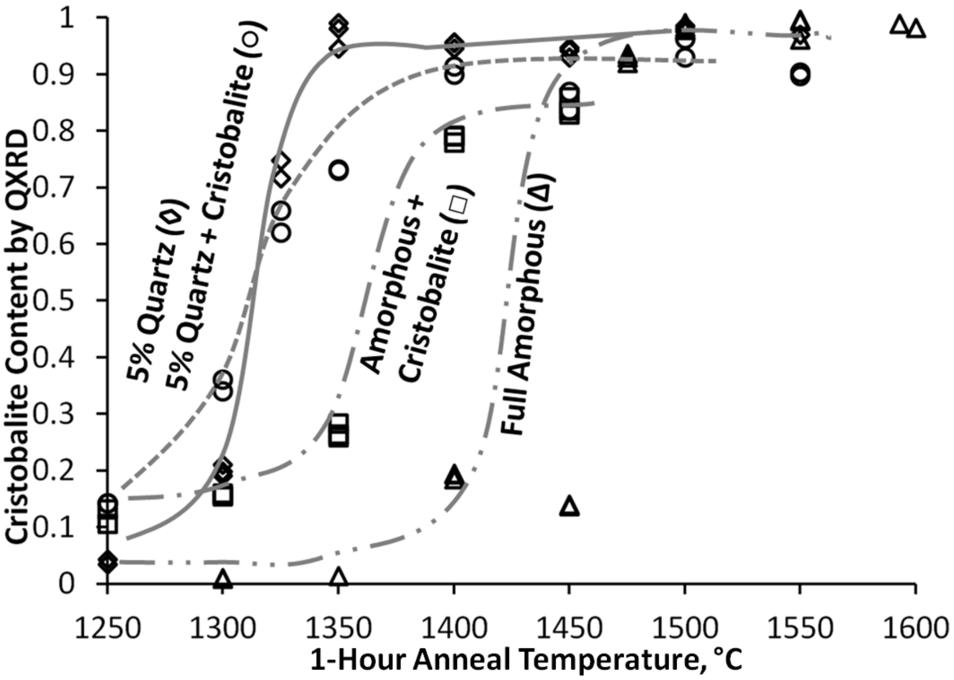

Figure 2.9 Comparison of cristobalite content in varying powder formulations following 1-hr isothermal annealing at various temperatures. Compares transformation of fully amorphous powder, fully amorphous powdered seeded with 10 wt% cristobalite, 5% residual quartz powder, and 5% residual quartz powder seeded with 10 wt% cristobalite.

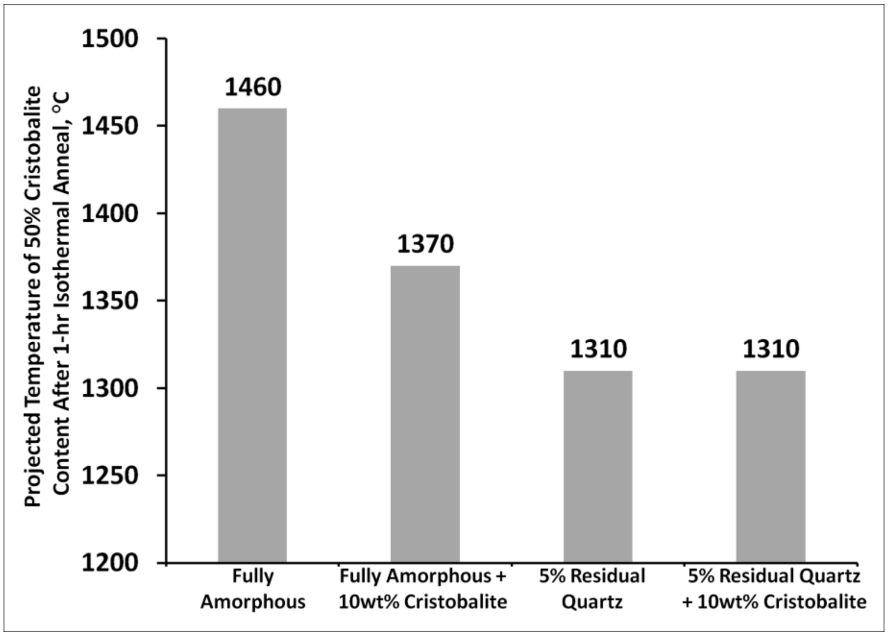

Figure 2.10 Temperature for Y=0.5 following 60 minute anneal for seeded and unseeded formulations.

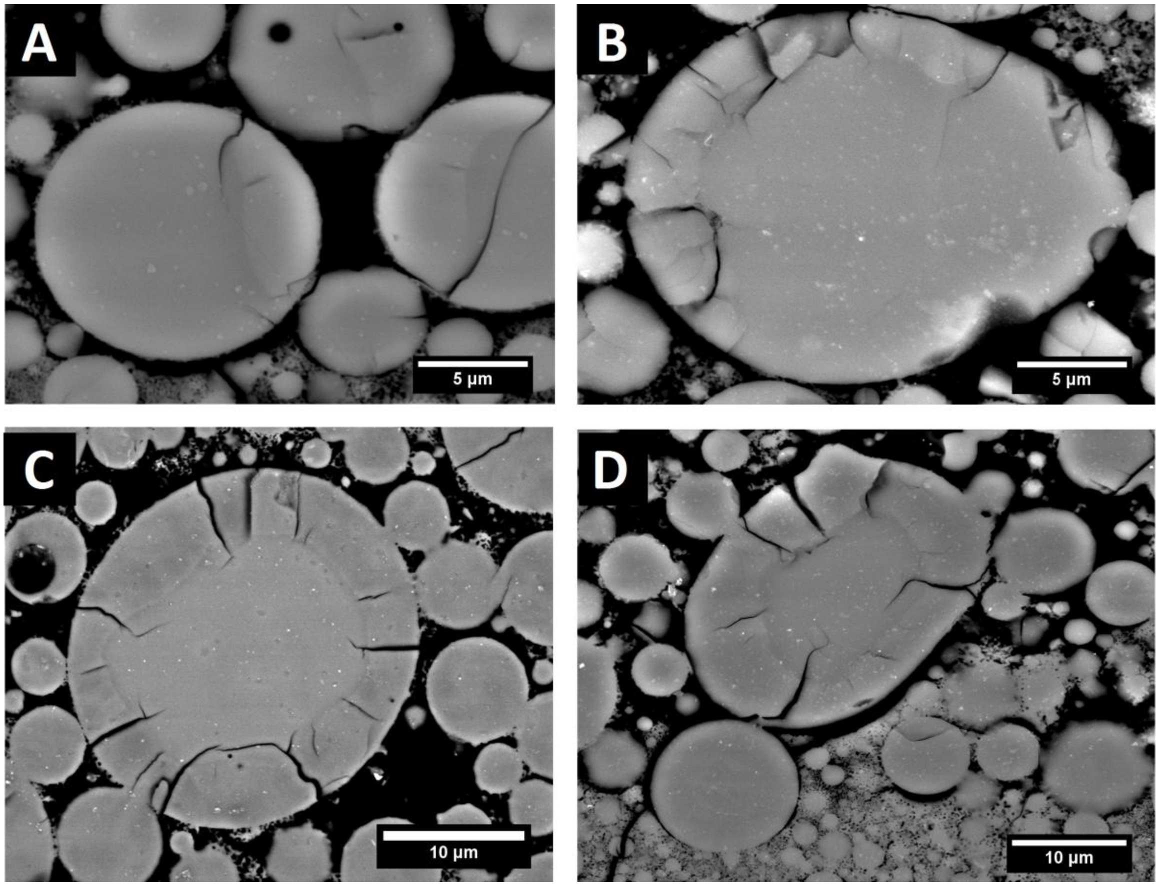

Figure 2.11 Partially crystalline material imaged with electron back scatter, BSE. The growth of the cristobalite crystalline phase on particle surface and the development of a core-shell morphology is visible. (A) 11% cristobalite content. (B) 25% cristobalite content. (C) 55% cristobalite content. (D) 84% cristobalite content.

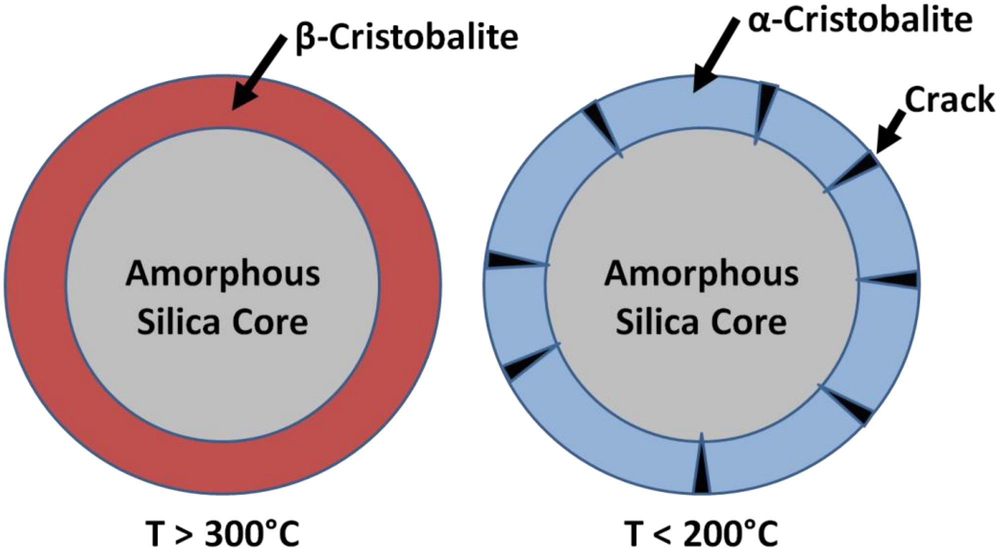

Figure 2.12 Illustration of the observed core-shell morphology. At high temperature the silica crystallizes to β-cristobalite forming a crystalline shell around the amorphous particle core, upon cooling below the β-α transition the cristobalite transitions to α-cristobalite and cracks due to the 4.9% volume reduction and constraint of the amorphous core.

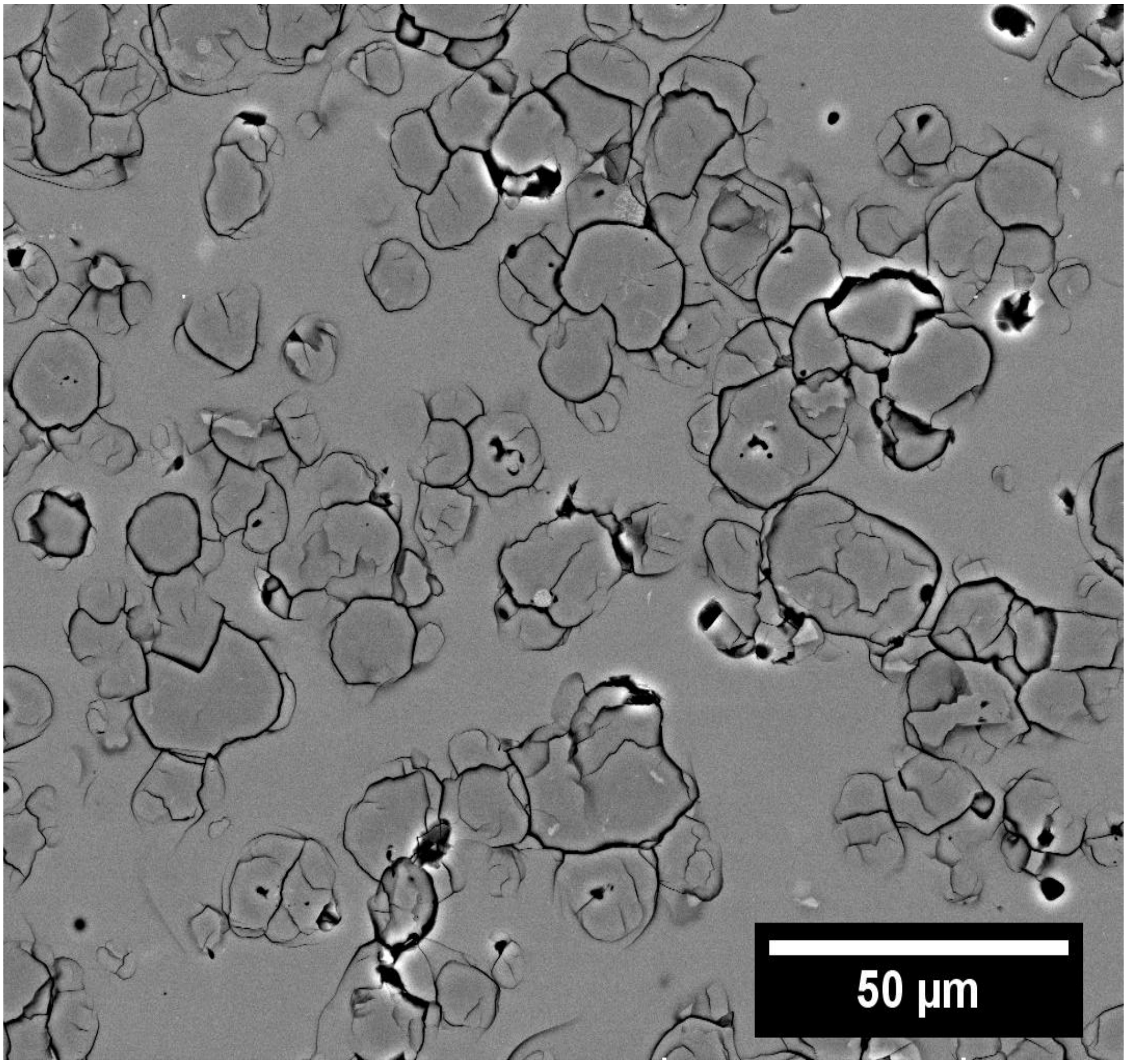

Figure 2.13 Sample annealed at 1550°C for 10 minutes imaged by backscattered electrons, where cristobalite is slightly darker in contrast. This specimen had 41% cristobalite by QXRD. Cracking is from the transformation to α-cristobalite on cooling.

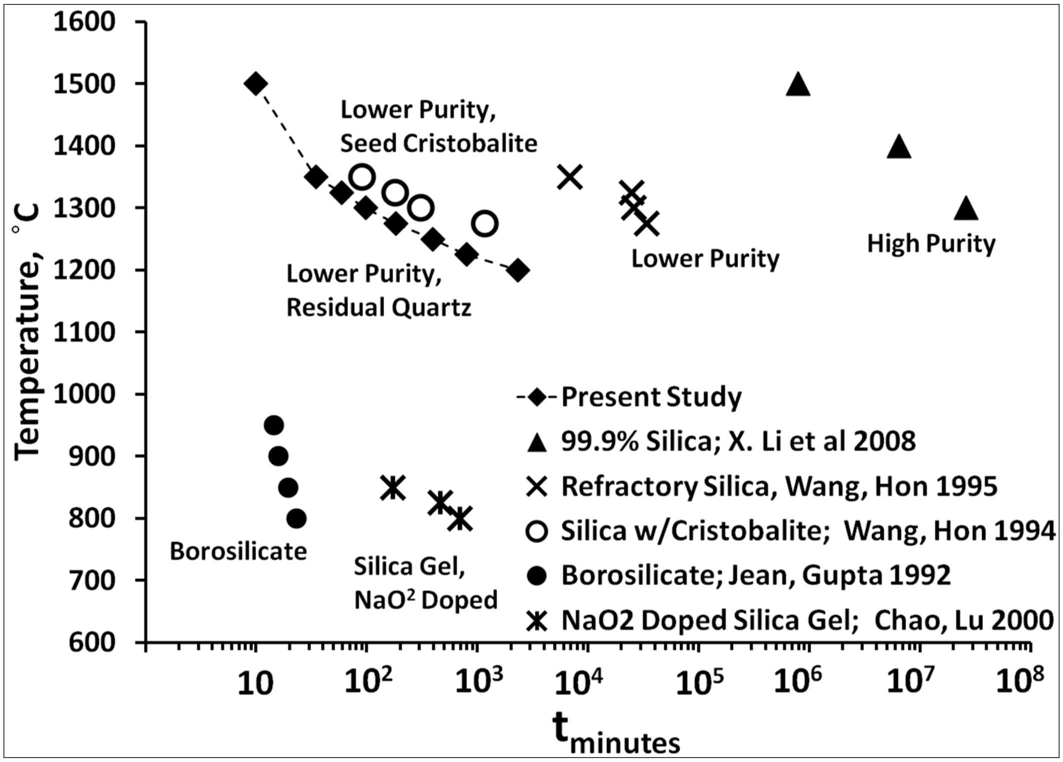

Figure 2.14 Comparison of results to published JMAK values for crystallization of silica to cristobalite presented in TTT format for Y=0.5. Results from present study include the additional direct observation of Y=0.48 for 10 minute anneal at 1500°C.

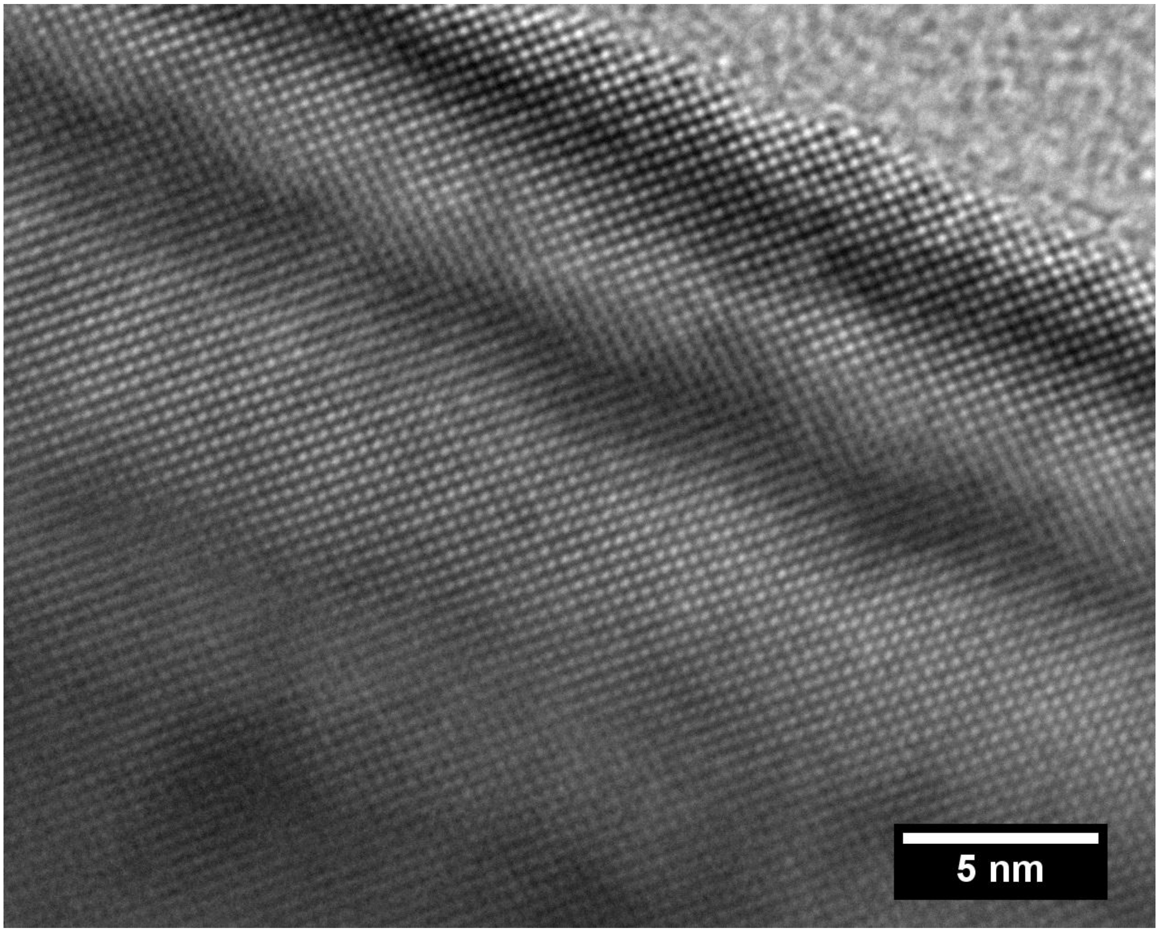

Figure 2.15 HRTEM image of quartz crystal within the sintered silica powder. Viewed along 211 zone axis.

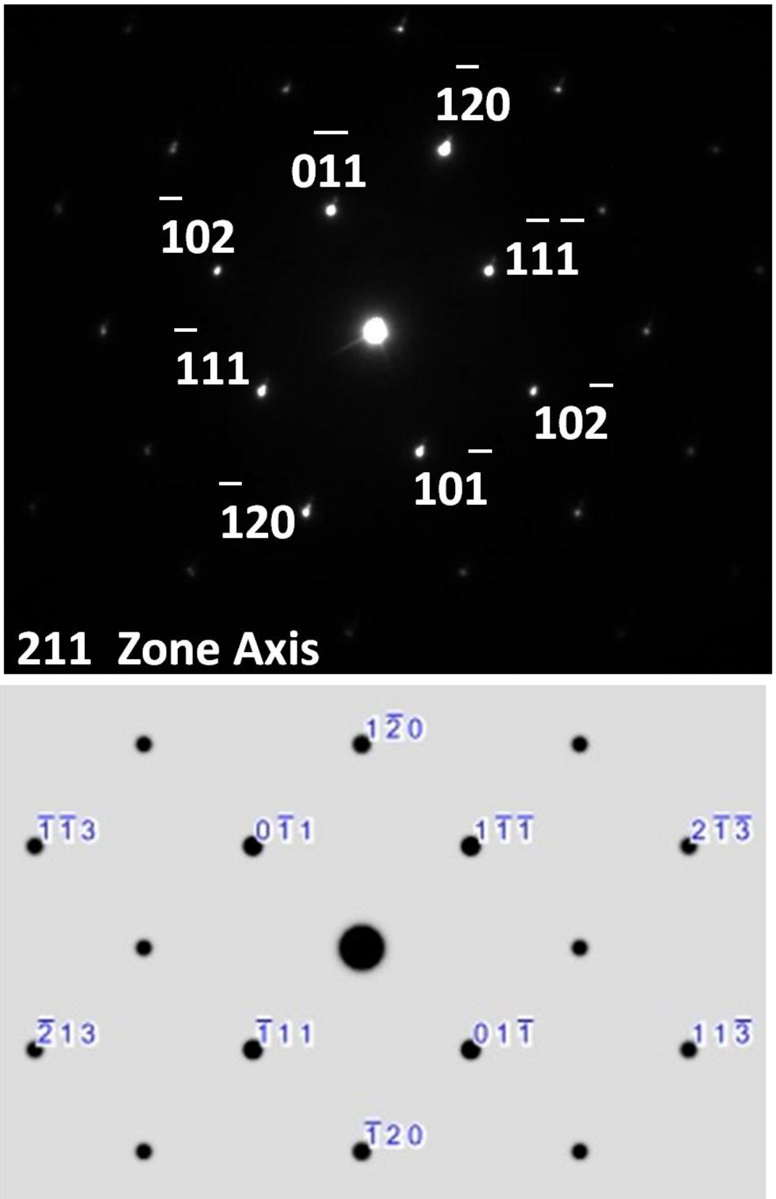

Figure 2.16 SAED image taken from view in Fig.2.14 (above) and simulated SAED (below) for 211 zone axis of α quartz. Plane spacing and angles confirm SAED image is α quartz viewed along 211 zone axis.

Chapter 3
Stress Relaxation in Sintered Silica with Cristobalite

3.1 Preface

In order to control the sintering shrinkage and creep of LAMP molds at high temperature, the amorphous silica is partially crystallized to cristobalite. However, cristobalite is known to reduce room temperature strength. Understanding of the impact of cristobalite on the sintering and creep is needed in order to optimize the cristobalite content. Stress relaxation of sintered silica samples of varying cristobalite content were observed at 1100C under constant axial strain. The resulting stress relaxation as a function of cristobalite content data is used to better inform the choice of target cristobalite content of LAMP molds.

3.2 Introduction

Sintered silica investment casting refractory molds are designed with a certain porosity, but they must resist sintering at casting temperatures, which causes the mold to shrink. The refractories must also resist deformation from mechanical loads, which causes distortions. To suppress sintering and creep deformation, it is a common technological practice to partially devitrify the initially amorphous silica to form a certain fraction of cristobalite.[1, 2, 3, 4, 5] However, cristobalite weakens sintered silica ceramics from microcracking due to the β-to-α phase transformation. Therefore, a balance is sought to have enough cristobalite to suppress deformation, but not too much which would reduce strength. The relationship between the amount of cristobalite and the resistance to deformation and sintering is not known quantitatively. In this paper we attempt to address this with simple stress relaxation experiments to determine how the amount of cristobalite changes the relaxation of stress at constant strain for sintered silica ceramics.

The general case of sintering and creep in multiphase materials has been widely studied, notably Scherer[6] reported on sintering in 1987 and Wilkinson[7] on creep in 1998. Wereszczak et al.[1] have examined the creep behavior of specific refractory mixtures, while Taylor et al examined the shrinkage behavior[3] in such systems. While others including Rouxel et al[8] have looked at the impact of crystalline content on creep behavior of specific dense glasses. Prado et al[9, 10] have extensively reported on the sintering of glass with concurrent crystallization. However, no study has shown the creep and shrinkage behavior of porous refractory sintered silica as a function of crystalline content.

We examine sintering and creep of porous sintered silica by means of stress relaxation. We measure stress vs. time, and direct our attention to the stress relaxation rate vs. time, and the logarithmic decrement vs. time. Our particular interest is the influence of cristobalite on sintering and creep by means of its influence on stress relaxation. We are primarily interested in comparing the behavior as a function of the amount of cristobalite, and we do not attempt to infer the mechanisms. Whether it occurs by densification or creep, stress relaxation involves very small strains. For our experiments, the stress can be relaxed by strains on the order of 0.0001, which are too small to contrast with expectations from steady state creep models. Instead we address the phenomenological behavior of porous sintered silica with varying amounts of cristobalite. Understanding the way in which cristobalite content impacts stress relaxation is of great practical value for the use of sintered silica refractories.

3.3 Procedure:

We conduct relaxation experiments at 1100°C by imposing an axial stress of 4 MPa on sintered silica disks and measuring load vs. time at constant strain. Prior to the stress relaxation experiments, the samples had been sintered to establish a certain sintered density and subjected to crystallization anneals at 1275-1400°C to establish a certain amount of β-cristobalite. To avoid microfracture from the transformation of β-cristobalite to α-cristobalite, which occurs around 250°C[11, 12], we avoid cooling the specimens to room temperature, and conduct both the crystallization anneal and the stress relaxation in the high temperature mechanical testing system.

3.3.1 Materials:

An amorphous silica powder with a purity of 99.7% and a residual crystalline quartz fraction of 5% was used in this study, (TECO-Sphere-Microdust, CE Minerals, Greenville, TN). The powder has a spherical morphology and consists primarily of 5-20 micron spherical particles with a small fraction of fine submicron particles. The detailed powder characteristics were previously reported.[13]

3.3.2 Annealing and Relaxation Testing

Pellets approximately 25 mm in diameter and 6 mm in thickness were produced by dry-pressing the powder in a 25 mm die with a load of 30 MPa. Prior to testing the as-pressed pellets were pre-sintered on an alumina plate for 1 hour at 1100°C in a box furnace under lab air with humidity ranging from 15-60% relative humidity. Furnace ramp rates of 20°C/min on heating and 15°C/min on cooling were used. The pre-sintering anneal produced a pellet of 25% open porosity as determined by Archimedes method, ASTM C-373-88. At 1100°C no crystallization occurs leaving the pellets with the same 95% amorphous, 5% residual crystalline quartz as the starting powder. This pre-anneal was done to ensure a baseline level of densification and strength to facilitate handling during the high-temperature anneal and testing.

The mechanical testing and high-temperature crystallization anneal were both conducted on an Instron 4483 screw driven electromechanical test frame with an attached ATS high temperature "clam-shell" style furnace. Pre-sintered discs were loaded into the furnace between alumina platens resting on the lower alumina push-rod of the mechanical test frame. The upper push rod was left 2.5 cm above the upper alumina platen to allow room for thermal expansion during the anneal. The sample was then annealed at 1275-1400°C with hold times of 30 s to 24 hours. Samples were heated from room temperature to annealing temperature over a 4.5 hour ramp producing heating rates of 4.1 to 5.2°C/minute. Following heating the samples were held at 1100°C for testing.

Load relaxation was conducted on samples at 1100°C following the high temperature anneal. Disc-shaped samples were compressed axially between flat alumina platens under load control to achieve an axial compressive stress varying from 4.0-4.4 MPa. At that point, cross-head displacement was held constant and resulting stress observed as a function of time at 1100±8 C for 10,000 seconds. The rigidity of the system was determined by a blank run, where the crosshead displacement was held constant with no sample, so the push rods and platens were in direct contact. After an initial relaxation of 0.1±0.02 MPa the stress stayed constant within 2.5% over the period 500-10,000 seconds at 1150°C.

Relaxation was examined at 1100°C to avoid further cristobalite crystallization during testing, which would have occurred at higher temperatures. A previously reported kinetics study[13] had found the crystallization of the this silica powder to be slow in comparison to test times at temperatures up to 1200°C. However, it was found that samples partially crystallized at higher temperatures continued to crystallize over the relaxation experiment at temperatures as low as 1125°C. Further, it was found that relaxation did not occur below 1100°C at the time scales observed, which is consistent with the reported glass transition of amorphous silica, of around 1100°C.[14] For this reason samples were only tested at 1100°C to avoid the complication of concurrent crystallization.

Following testing samples displayed a density of 81-83% full density and corresponding open porosity of 17-19% with no closed porosity as determined from similarly fired samples by the Archimedes method, ASTM C-373-88.

Following testing cristobalite content was determined by quantitative powder x-ray diffraction (QXRD) using TiO_2 anatase as an internal standard by the method previously reported.[13]

3.4 Results:

3.4.1 Relaxation Curves

The stresss relaxation behavior is presented in Figure 3.1, which shows the remaining stress vs. time for samples with 0%, 1%, 18%, 25%, 52% and 90% cristobalite.

Stress relaxation is faster in fully amorphous sintered silica, and significantly slower in sintered silica with higher cristobalite content. After 6,000 seconds, the fully amorphous specimen with no cristobalite had only 1.2 MPa retained compressive stress, so 70% of the stress had relaxed in this time period. The specimen with 19% cristobalite retained 2.4 MPa, having relaxed 40% relaxed of the stress, and the specimen with 90% cristobalite retained 3.4 MPa, having relaxed only 15% of the stress in this time period.

The rate of stress relaxation is not constant and decreases over time. If we choose to use a logarithmic decrement, as is commonly done for many relaxation behaviors, we can define the rate of relaxation:

$$\frac{d ln\left(\frac{\sigma_t}{\sigma_o}\right)}{dt} = \frac{-1}{\tau} \qquad Eq. 3.1$$

in which σ_t is the stress at time t, σ_o is the initial stress, and the apparent relaxation time τ carries the units of time. Newtonian materials have a single relaxation time τ which is invariant with time. Figure 3.2 shows that the apparent relaxation time τ increases with time, in a manner that depends strongly on the amount of cristobalite. For fully amorphous sintered silica with 0% cristobalite the relaxation time is about 5 ksec at the early stages, and lengthens slightly to 8 ksec near the end of the test. In contrast, the sintered silica with 90% cristobalite has a much longer relaxation time in the early stages, 20 ksec, and the relaxation time increases dramatically over time to 73 ksec as the end of the experiment. Clearly stress relaxation in this material does not behave in a Newtonian manner. For the fully amorphous samples containing no cristobalite τ only increases slightly and the behavior is approximately Newtonian. But for higher cristobalite contents τ is longer and changes more significantly with time deviating dramatically from Newtonian behavior. It can be seen the increase in τ over the test is larger for samples with 25% and 52% cristobalite compared to the fully amorphous sample. And the increase in τ for the 100% sample is substantially larger than the others with τ more than tripling over the time interval shown. Cristobalite not only increases the relaxation time, but also the manner in which relaxation changes with time.

It is useful to look at the relaxation behavior as a function of the remaining stress. In Figure 3.3 the apparent relaxation times from Figure 3.2 are replotted as a function of stress. Here the time range displayed is 500 to 6,000 seconds as in Figure 3.2. Fully amorphous samples relaxed away 1.5 MPa or 37% of the initial stress by the start of the τ data at 500 seconds while the 100% cristobalite sample still retains over 75% of the initial stress after 6,000 seconds. Once again it is apparent that as cristobalite content increases the relaxation time increases, and as cristobalite content increases the increase in relaxation time over the test increases as well.

The relaxation time τ is dependent on stress as seen in Figure 3.3. To determine the nature of this relationship the relaxation time was plotted against stress. A plot of $\ln(\tau)$ vs σ_t displayed a linear relationship as seen in Figure 3.4. Samples with differing cristobalite contents were found to display differing slopes and intercepts but all were found to fit a linear relation. The linear fits seen in Figure 3.4 can be fit to the equation:

$$\ln(\tau) = ln\left(\frac{-dt}{ln\left(\frac{\sigma_t}{\sigma_o}\right)}\right) = mln\sigma_t + b \qquad Eq. 3.2a$$

in which *m* and *b* are the slope and intercept of the linear fits respectively. To simplify the equation we can define b=ln(q), allowing us to write:

$$\ln(\tau) = ln\left(\frac{-dt}{ln\left(\frac{\sigma_t}{\sigma_o}\right)}\right) = mln\sigma_t + \ln(q) \qquad Eq. 3.2b$$

Higher cristobalite contents are associated with larger values for m and ln(q) which are tabulated in Table 3.1 for the results in Figure 3.4. The slope m was found to vary significantly from a value of -0.68 in the sample with no cristobalite to -9.88 in the sample with 90% cristobalite. The relationship in Eq.3.2b allows us to explicitly define an empirical relation for the change in stress at a give time as a function of the stress in terms of the m and q parameters found for each cristobalite content found in Figure 3.4:

$$\frac{d\sigma}{dt} = -q\sigma^{-(m+1)} \qquad Eq. 3.3$$

From this relationship we see that higher cristobalite contents are associated with a larger stress exponent. The larger stress exponents are in turn associated with the greater degree of “hardening” type behavior seen in Figure 3.2, in which τ was seen to increase over the course of testing. Material with higher cristobalite content exhibit a greater increase in τ during testing and present a larger value for m.

3.4.2 Microstructure

A fired but untested sample was cut across the diameter, impregnated with epoxy and polished to a 0.05 micron finish. The microstructure was imaged under secondary electron, SE, to illustrate the sintered microstructure, Figure 3.5. It can be seen the large spherical particles are only lightly sintered and the density of the material varies with some dense and some sparse regions. The distribution of cristobalite can be imaged by electron back-scatter, BSE, in which the small density difference between the crystalline and amorphous phase provides contrast. Figure 3.6 illustrates the surface nucleation of cristobalite and its distribution. At an 11% cristobalite phase fraction, cristobalite can be seen forming at the surface of the particles. At 25%, a cristobalite “shell” has formed surrounding the amorphous “core” of the particle. This surface nucleation agrees with the observations reported for silica. [2, 5, 15, 16, 17]

3.5 Discussion:

3.5.1 Impact of Cristobalite Content on Stress Relaxation

With increasing cristobalite content the τ was larger and increased with time at a faster rate. The relaxation time τ was found to vary slightly from a constant value for samples with no cristobalite. Ideally, amorphous material is Newtonian. The fully amorphous samples with no cristobalite, were nearly Newtonian with τ changing only slightly during testing. In contrast, as cristobalite content increased samples were seen to deviate more dramatically from Newtonian behavior. Thus, cristobalite content impacted not only the observed relaxation time, but the behavior over the course of testing. In samples containing cristobalite, the apparent relaxation rate τ was found to increase with increasing cristobalite content. Further, the degree to which τ increased over the course of testing increased with increasing cristobalite content. That is, higher cristobalite contents were associated with larger τ and larger degree of apparent hardening over the course of the test. The role of cristobalite was not simply to slow the relaxation producing a longer τ, but to alter the way τ changed over the course of testing. This impact from cristobalite was significant. As seen in Figure 3.3, the relaxation time for a 90% cristobalite sample was 3.5 times longer 500 seconds into a test and 8.5 times longer 6,000 seconds into a test compared to a sample with no cristobalite. The sample with 90% cristobalite content still retained 3.4 MPa (85%) of the initial compressive load after 6,000 seconds at 1100°C while the sample with no cristobalite content retained only 1.2 MPa (30%) of the initial load over the same time. This dramatic impact of cristobalite content in captured in the empirical relationship presented in Eq.3.3. The slopes of the plot of ln(τ) vs $ln(\sigma_t)$ in Figure 3.4 vary significantly with cristobalite content. High cristobalite content is associated with a larger slope, a larger value to the constant, m, and a greater stress dependence in Eq.3.3. The stress exponent in Eq.3.3 was found to be 6.5 times larger in material with 90% cristobalite than 0% cristobalite, highlighting the dramatic role of cristobalite content on the relaxation rate as a function of stress. Cristobalite dramatically slows relaxation with higher cristobalite contents associated with longer relaxation times and greater degrees of hardening over the course of testing.

3.5.2 Relative Roles of Sintering and Creep on Stress Relaxation

Stress relaxation can occur through sintering or by creep. Each of these mechanisms is dependent on mobility but they differ in driving force. Fundamentally, sintering is flow driven by the reduction of surface energy. Creep, on the other hand, is material flow driven by an external stress. Both can show a dependence on time, which in our study was linked to stress. However, in the case of sintering, this time dependence is associated with the change in surface area and structure associated with sintering. As sintering progresses surface energy is reduced and the rate of sintering can slow as the driving force diminishes. In the limit of incredibly small strains, such as the less than 0.01% strain in the present study one would not expect sintering to depend on time as densification cannot progress sufficiently for the rate to slow. Therefore in the context of stress relaxation one would expect the rate of relaxation due to sintering to be independent of residual stress. Creep, on the other hand, is directly dependent on stress as applied stress is the driving force. During stress relaxation the driving force for creep diminishes as the stress diminishes. Therefore one would expect that stress relaxation due to creep would show hardening behavior as relaxation rate slows as the stress diminishes. In light of this, the strong dependence on stress and time observed suggest creep was the dominant mechanism.

3.5.3 Optimizing Cristobalite Content in Refractories

The observed relaxation behavior as a function of cristobalite content can be used to optimize crystallization of sintered silica to suppress sintering and creep. The results showed increasing relaxation times with increasing cristobalite content across the entire range of crystallinity. This indicates that if suppression of creep and sintering behavior is the only concern in a sintered silica refractory, the cristobalite content should be maximized and the sintered silica fully crystallized. Of course, this result is trivial. It could be concluded without testing that full crystallization to cristobalite would provide the greatest sintering and creep resistance possible. In reality we are aware the cristobalite content is associated with a loss of strength (the exact relation is explored in Chapter 4). This presents a trade-off between suppression of sintering and creep and the strength of the refractory material.

The present results can assist in optimizing the cristobalite content by considering the gains in sintering and creep resistance for intermediate values. It can be seen in Figures 3.2, 3.3 and 3.4 that there is a significant change in the relaxation rate between fully amorphous material and material with 25% cristobalite content. However, there are small changes in relaxation behavior between material with 25% cristobalite and material with 52% cristobalite. Further, there are again large changes between material with 52% cristobalite and material with 90% cristobalite. This indicates there are significant gains to the creep and sintering resistance to developing 25% cristobalite content as opposed to fully amorphous material, very little reason to increase the crystallinity to ~50%, but further significant gains to approaching full crystallization. If the creep and sintering resistance provided by 25% cristobalite content are sufficient for a process, then ~25% may be an optimal target crystallinity to maximize creep resistance and minimize loss of strength. If greater creep is needed then the material will need to be crystallized to nearly 100% cristobalite, as very little is gained at intermediate values. The data indicate that in order to optimize cristobalite content for creep resistance it is best to target either low cristobalite content or fully crystallize the material, as intermediate values provide very small marginal gain with increasing cristobalite content.

3.6 Conclusions:

The stress relaxation of sintered silica was observed at 1100°C under constant strain. The stress relaxation rate was found to decrease with crystalline cristobalite content. It was found that the apparent relaxation time of the material, τ increases with increasing cristobalite content. The apparent relaxation time increases with time as stress decreases during testing, and the rate at which τ increases with time was larger at higher cristobalite contents. The apparent relaxation time varies systematically with the cristobalite content. The natural log of the apparent relaxation time was found to be a linear function of the natural log of the remaining stress, with parameters varying as a function of cristobalite content.

3.7 References

1. A. A. Wereszczak, K. Breder, M. K. Ferber, T. P. Kirkland, E. A. Payzant, C. J. Rawn, E. Krug, C. L. Larocco, R. A. Pietras, and M. Karakus, "Dimensional changes and creep of silica core ceramics used in investment casting of superalloys," *J. Mater. Sci.*, 37[19] 4235-45 (2002).

2. A. Kazemi, M. A. Faghihi-Sani, and H. R. Alizadeh, "Investigation on cristobalite crystallization in silica-based ceramic cores for investment casting," *J. Eur. Ceram. Soc.*, 33[15-16] 3397-402 (2013).
3. B. Taylor, S. T. Welch, and S. Blackburn, "Investigation into the Effect of Common Ceramic Core Additives on the Crystallization of Amorphous Silica," *Mechanical Properties and Performance of Engineering Ceramics and Composites VIII: Ceramic Engineering and Science Proceedings*, 34 (2013).
4. E.-H. Kim, G.-H. Cho, Y. Yoo, S. Seo, and Y.-G. Jung, "Development of a new process in high functioning ceramic core without shape deformation," *Ceram. Int.*, 39[8] 9041-45 (2013).
5. A. Kazemi, M. A. Faghihi-Sani, M. J. Nayyeri, M. Mohammadi, and M. Hajfathalian, "Effect of zircon content on chemical and mechanical behavior of silica-based ceramic cores," *Ceram. Int.*, 40[1, Part A] 1093-98 (2014).
6. G. W. Scherer, "Sintering with Rigid Inclusions," *Journal of the American Ceramic Society*, 70[10] 719-25 (1987).
7. D. S. Wilkinson, "Creep mechanisms in multiphase ceramic materials," *Journal of the American Ceramic Society*, 81[2] 275-99 (1998).
8. T. Rouxel, B. Baron, P. Verdier, and T. Sakuma, "SiC particle reinforced oxynitride glass: Stress relaxation, creep and strain-rate imposed experiments," *Acta Mater.*, 46[17] 6115-30 (1998).
9. M. O. Prado, M. L. F. Nascimento, and E. D. Zanotto, "On the sinterability of crystallizing glass powders," *J. Non-Cryst. Solids*, 354[40-41] 4589-97 (2008).
10. M. O. Prado and E. D. Zanotto, "Glass sintering with concurrent crystallization," *C. R. Chim.*, 5[11] 773-86 (2002).
11. R. B. Sosman, "The Phases of Silica." Rutgers University Press, (1965).
12. D. R. Peacor, "High-temperature Single Crystal Study of Cristobalite Inversion," *Z. Kristall.*, 138 274-98 (1973).
13. R. C. Breneman and J. W. Halloran, "Kinetics of Cristobalite Formation in Sintered Silica Glass," *Journal of the American Ceramic Society* (in revision 2014).
14. D. M. Krol, K. B. Lyons, S. A. Brawer, and C. R. Kurkjian, "High-Temperature Light-Scattering and the Glass-Transition in Vitreous Silica," *Phys. Rev. B*, 33[6] 4196-202 (1986).
15. F. E. Wagstaff, "Crystallization and Melting Kinetics of Cristobalite," *Journal of the American Ceramic Society*, 52[12] 650-& (1969).
16. F. E. Wagstaff and K. J. Richards, "Kinetics of Crystallization of Stoichiometric SiO2 Glass in H2O Atomospheres," *Journal of the American Ceramic Society*, 49[3] 118-& (1966).
17. A. G. Verduch, "Kinetics of Cristobalite Formation from Silicic Acid," *Journal of the American Ceramic Society*, 41[11] 427-32 (1958).

Table 3.1 Slopes and Intercepts for Linear Fits in Figure 3.4

Cristobalite Content	m	ln(q)
0%	0.68	9.12
25%	3.56	13.63
50%	2.5	12.89
90%	9.88	22.52

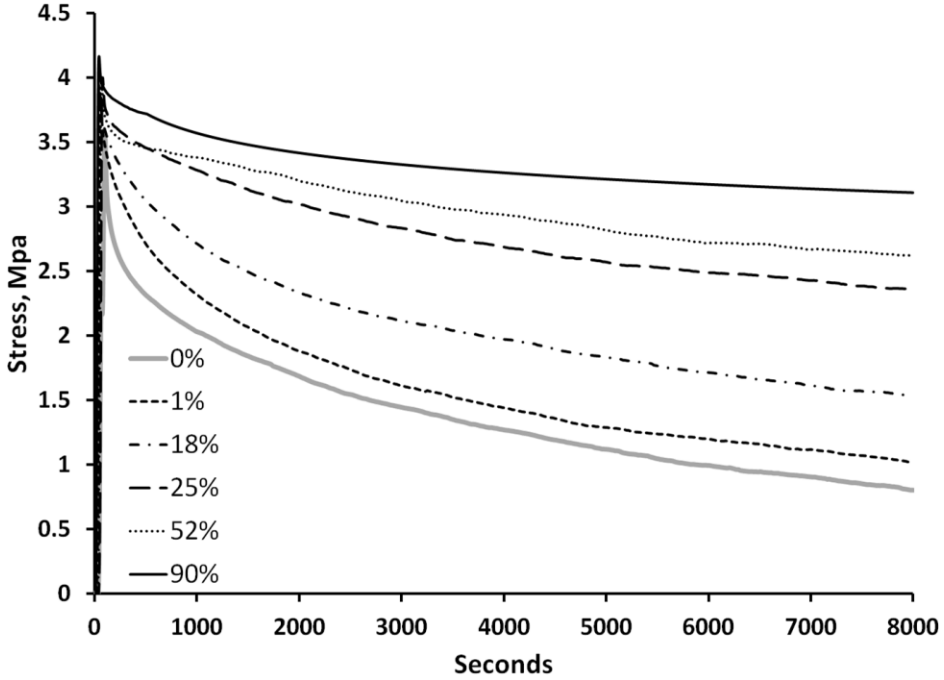

Figure 3.1 Stress relaxation observed for 5 separate specimens found to have 0, 1, 18, 25, 52, and 90% cristobalite content.

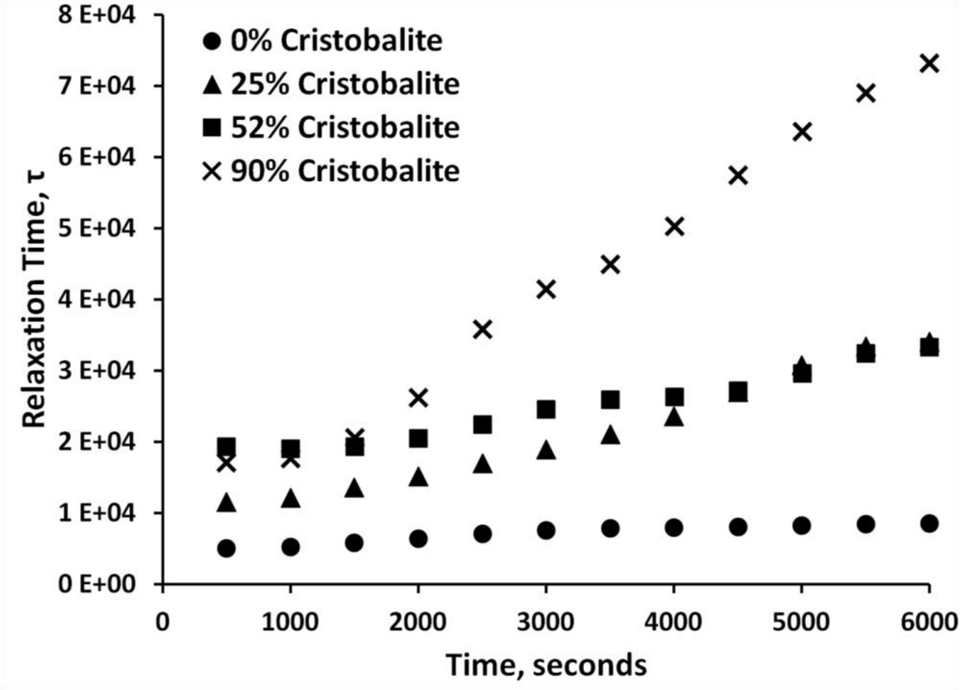

Figure 3.2 Relaxation time τ vs time for 4 specimens whose relaxation curves appear in Fig. 1. The data does not fit a single relaxation time. Remaining compressive load varies between the data sets.

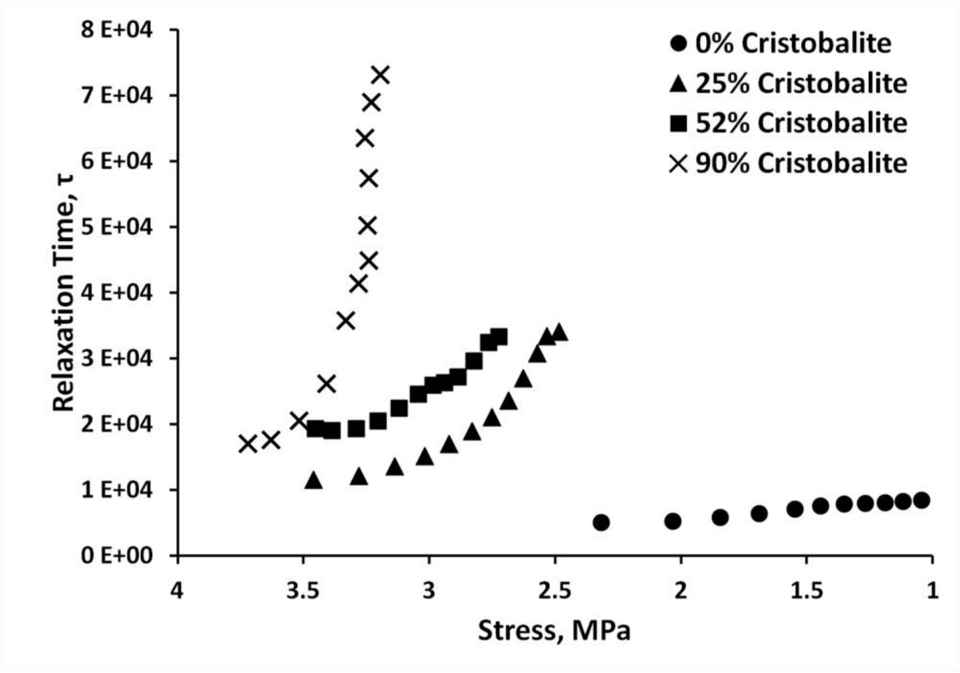

Figure 3.3 Apparent relaxation time τ vs stress for the samples and time increment seen in Fig.3. The data covers 500-6,000 seconds with time intervals of 500 seconds, and progresses from left to right.

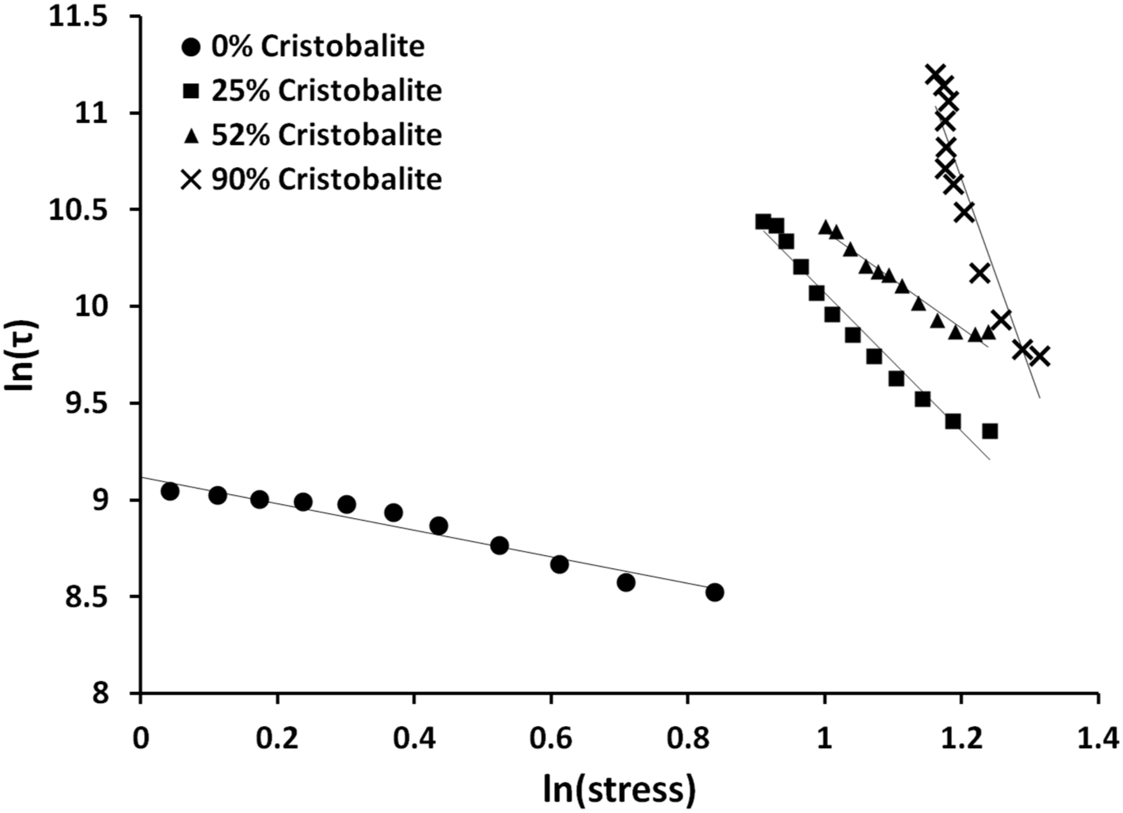

Figure 3.4 Relaxation time observed at 2 ksec into testing. The variability in local slope of the relaxation curve is significant, providing the stochasticity seen here.

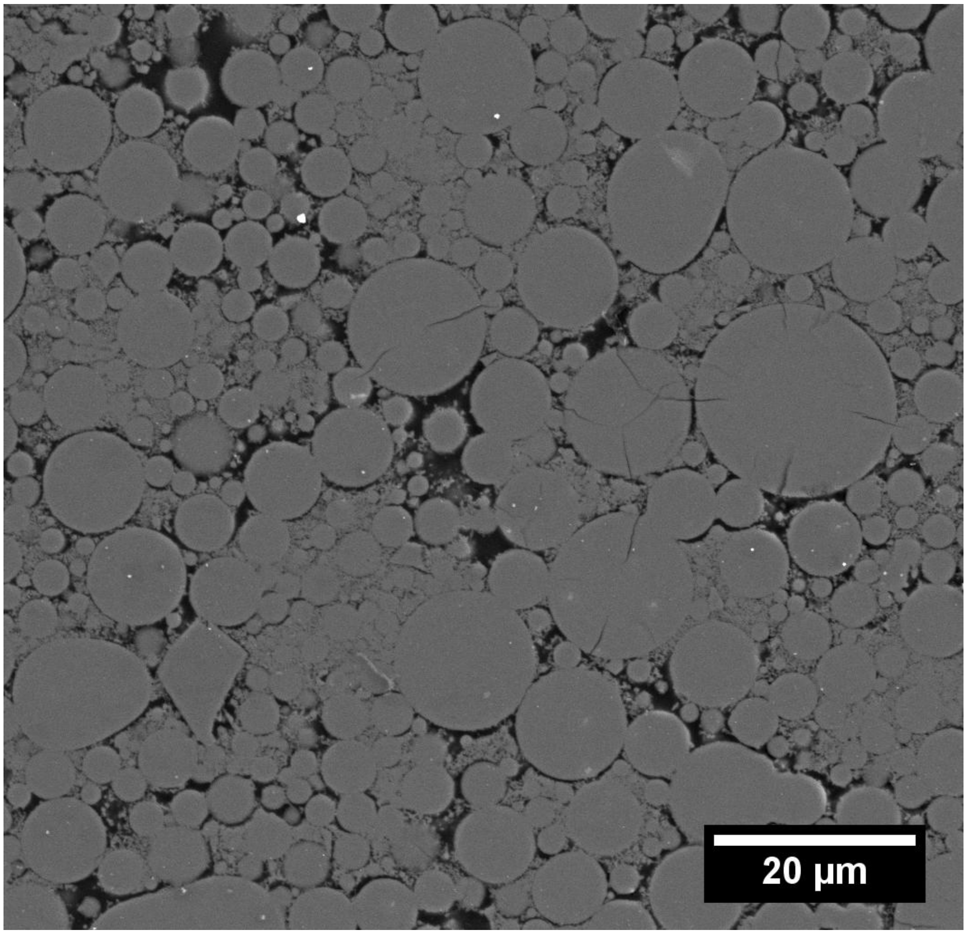

Figure 3.5 Secondary electron, SE, imaging of a sample with a 50% cristobalite phase fraction illustrating the typical microstructure. Cracking is due to the ~5% volume change on transformation from α-to-β cristobalite at ~250°C.

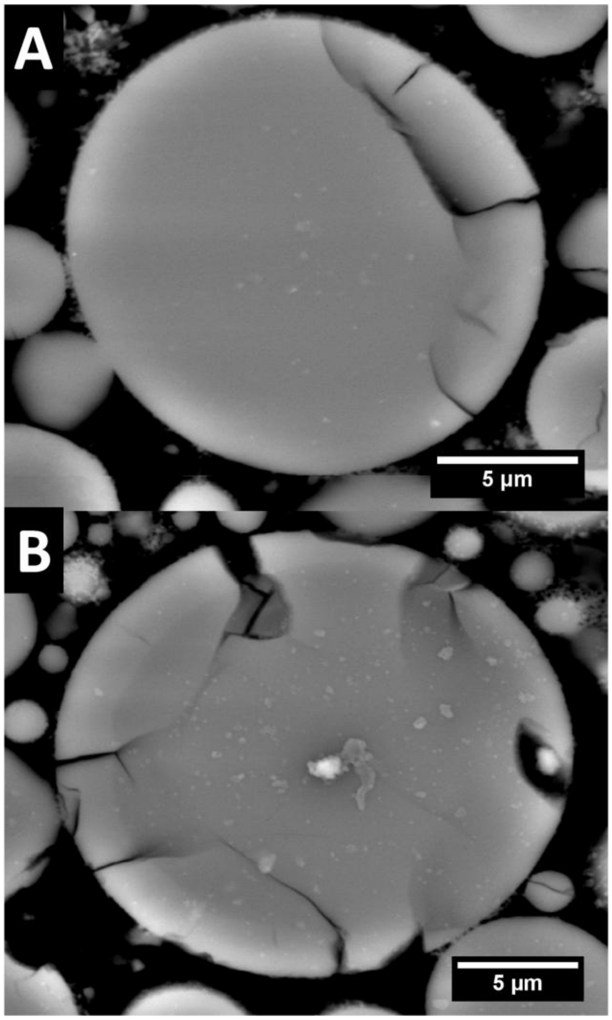

Figure 3.6 Electron back-scatter, BSE, image of material illustrating the surface nucleation and development of a core-shell microstructure. (A) 11% cristobalite phase fraction (B) 25% cristobalite phase fraction.

Chapter 4
Effect of Cristobalite on the Strength of Sintered Silica Above and Below the Cristobalite Transformation

4.1 Preface

The strength of LAMP molds was an important concern in optimizing the cristobalite content for casting. While it is generally accepted that cristobalite content weakens materials due to the formation of microcracks, the exact relationship was not known. Accurate understanding of cristobalite's impact on strength is needed in order to better strike a balance between the gains in creep resistance with higher cristobalite content and potential loss of strength. To better understand the impact of cristobalite content on strength, sintered silica was tested under three different conditions. First, samples were tested at 350°C as β-cristobalite having never passed the β-α transition, in order to evaluate the impact of cristobalite outside of fracture caused by the phase change. Second, samples were tested at room temperature as α-cristobalite to evaluate the impact of the β-α transition on strength. Third, samples were tested at 350°C as β-cristobalite after having been previously been cooled to 25°C to establish if any strength was recovered on conversion back to β-cristobalite.

4.2 Introduction

Porous sintered silica is a common refractory material, often used in the casting of superalloy airfoils. In service it is crystallized to beta-cristobalite to suppress sintering shrinkage and creep deformation.[1, 2, 3, 4, 5] For at least a century it has been known that cristobalite weakens sintered silica.[6] This weakening arises from the extensive microfracture of the cristobalite caused by the phase transition from β-cristobalite to α-cristobalite at ~250°C, which has a ~5% volumetric reduction.[7, 8] Although cristobalite reduces the room temperature strength of silica-based investment casting molds, this weakening is a necessary trade off for the creep and sintering suppression provided by the crystalline phase. The literature on the effect of cristobalite on the strength of sintered silica is surprisingly sparse. Kazemi et al and Kim et al have independently reported on the flexural strength of partially crystallized and uncrystallized material, but they did so in refractory mixtures including zircon and other additives.[2, 3, 9] Taylor et al investigated the role of cristobalite development on sintering shrinkage at high temperature.[5] In this paper, we examine the strength of porous sintered silica over a range of cristobalite content. Strength is measured at 350°C, above the β-to-α transformation temperature, to assess the role of partial crystallinity. We also examine the room temperature strength, below the β-α transition temperature, to assess the possible influence of micro-cracking from the β-α transition. Finally, we examine the strength of partially crystallized silica which had been cooled to α-cristobalite, then heated to 350°C and converted back to β-cristobalite.

4.3 Procedure:

4.3.1 Methods:

We loaded sintered disk samples in diametral compression for specimens of varying cristobalite content to evaluate the failure under tensile loading. Diametral testing is well established means to test the failure of brittle materials under tension.[10, 11, 12, 13, 14] Indirect tensile strength by the diametral compression technique is an effective method for the testing of tensile failure in brittle materials. This method has been used for the testing of medicine tablets[15], concrete[16, 17], geological specimens[10, 18], bone substitutes[19, 20], silica aerogels[21], and glass[22]. For this technique, a load P applied along the diameter produces a tensile stress in the diameter plane which is:[12]

$$\sigma_{dia} = \frac{2P}{\pi D t} \qquad Eq. 4.1$$

In which P is the applied load, D is the disk diameter, and t the disk thickness. The appeal of this method is that it allows the loading of brittle samples under compression without the alignment and gripping problems that plague direct tensile testing of ceramics. Unlike flexural testing, it is not necessary to prepare carefully machined bars, as simple disks are used. This is particularly convenient for this study, since we must avoid cooling specimens below the ~250°C cristobalite transformation temperature, so all handling must be done while the specimen is hot. Specimens were tested at 350°C in the β-phase having never passed through the β-α transition, at 25°C in the α-phase, and at 350°C in β-phase having previously been cooled through the β-α transition to 25°C.

4.3.2 Materials

This study was conducted with a commercially available amorphous silica powder, (TECO-Sphere-Microdust, CE Minerals, Greenville, TN). The powder is of 99.7% purity and is 95% amorphous with a 5% residual crystalline quartz fraction resulting from incomplete amorphization. The powder consists predominantly of 5-20 micron particles which display a spherical morphology, with small (<5% each) fractions of larger 20-50 micron particles and fine <1 micron particles. Details of the powder characteristics were previously reported.[23]

4.3.3 Annealing and Testing Procedure

Testing was conducted on pellets with approximate dimensions of 25 mm diameter and 6 mm thickness. These were produced by pressing the powder without binder under a 30 MPa load. In order to provide sufficient strength for handling the as-pressed pellets were annealed at 1100°C for one hour in a box furnace. This pre-sintering did not result in any crystallization and resulted in a pellet with 25% open porosity as determined by Archimedes method, ASTM C-373-88.

A high temperature anneal and subsequent mechanical testing were conducted on an Instron 4483 screw driven electromechanical test frame and attached ATS "clam-shell" style high temperature furnace. Samples were annealed at temperatures of 1100-1400°C for iso-thermal hold times of 20 minutes to 8 hours on a bed of cristobalite powder on an alumina plate. Samples tested in the α-cristobalite phase were cooled to room temperature for testing. Samples tested in the β-cristobalite phase were cooled to 350°C for testing. The transition from β-α-cristobalite is observed to occur between 200-273°C,[7] the test temperature allowed sufficient super heating to prevent any cooling to the transition when opening the furnace to load samples. Samples tested in the β-cristobalite phase after previously having passed the β-α transition were cooled to 25°C for 60 minutes and then re-heated to 350°C for testing. These samples are referred to as β-α-β samples. For testing, the samples were placed up-right on an alumina platen with forceps and the furnace closed. Contact with the sample was made between the lower alumina platen and the upper alumina push rod of the furnace. This loaded the sample along the vertical diameter. Testing was conducted under load control. Following sample failure it was removed from the furnace. Results from samples failing under tension by a vertical diametral fracture were included in this study, as the stress state was known. Some specimens failed in compressive crushing or other modes for which the stress state was not known, and these samples were discarded.

Density measurements were conducted by Archimedes method, ASTM C-373-88. The final density of the samples depended on the annealing temperature used. We only compare results at similar porosities. Samples annealed at 1100°C, corresponding to 0% cristobalite phase fraction, had 25.1±0.4% open porosity. Samples annealed at 1200°C, corresponding to >0% but <1% cristobalite phase fraction, had 23.1±1.1% open porosity. Samples annealed at 1275-1375°C, corresponding to 8-92% cristobalite phase fraction, had 17.9±2.3% open porosity. Samples annealed at 1400°C, corresponding to 100% cristobalite phase fraction, had 13.8±1.2% open porosity.

Cristobalite phase fraction was determined by quantitative x-ray diffraction, QXRD, using an internal standard of TiO_2 anatase by the method previously reported.[23]

The microstructure of the partially crystallized sintered silica was examined using polished cross sections. Annealed samples of known α-cristobalite content were impregnated with epoxy to fill the porosity, sectioned, and polished to 0.05 micron finish. The microstructure of the sintered samples was investigated by scanning electron microscopy using backscattered electron imaging under conditions where there was some contrast between the amorphous silica and the cristobalite.

4.4 Results:

For each specimen we have the value of strength, cristobalite fraction, and sintered density. The strength data are presented as cumulative strength distributions, specifically as cumulative fraction of specimens that are weaker than a particular strength value. The sets of tensile strengths are rank-ordered, expressed as a fraction of the population, and plotted directly so that the complete distributions can be compared for different ranges of cristobalite content. These ranges were 1-20% cristobalite, 20-40%, 40-60%, and 80-99% cristobalite, determined at room temperature as α-cristobalite by QXRD. Material was also tested with cristobalite content of 0%, <1%, which had lower sintered density and 100%, which had higher sintered density compared with the density of samples with 1-99% cristobalite content. The fracture strength also varies with sintered density, so the samples with 0, <1, and 100% cristobalite should not be directly compared with the 1-99% samples to report the effect of cristobalite alone. They will be discussed separately. The strength values varied over a wide range as is common in brittle materials. We report the cumulative strength distributions. They could not be usefully represented by a Weibull distribution, as the Weibull plots could not be fit with a single line.

Figure 4.2, Figure 4.4, Figure 4.6, and Figure 4.7 represent the strength distributions measured under three conditions: 1) samples never cooled below 350^{o}C and tested at 350^{o}C so that the cristobalite is in the high temperature β-phase (labeled “beta”); 2) samples cooled to room temperature and tested at 25^{o}C where the cristobalite is in the α-phase (labeled “alpha”); and 3) room temperature samples which had been re-heated to transform the α-cristobalite back to β-cristobalite, and tested at 350^{o}C in the β-cristobalite stability field (labeled “beta-alpha-beta”).

4.4.1 Strength at 25^o and 350^{o}C with no cristobalite Seeding

In order to establish whether testing temperature has an impact on measured strength we examined samples containing no cristobalite. These samples were annealed at 1100°C where previous kinetic studies have shown cristobalite will not form.[23] This was confirmed by x-ray diffraction, which showed no measurable cristobalite content. The porosity in these 1100°C samples was 25.1±0.4%, so the strengths cannot be compared with the denser specimens sintered at higher temperature. Figure 4.1 shows the cumulative strength distribution for cristobalite-free material measured at 25°C compared with the strength measured at 350°C. The strength distributions are very similar, suggesting that there is little effect of temperature itself in the range 25-350°C. Thus we might expect for specimens that contain cristobalite, that the difference between the 350°C strength (in the stability range of β-cristobalite) and the 25°C strength (in the stability range of α-cristobalite) reflects the impact of the phase transformation.

4.4.2 Strength as a Function of β-Cristobalite Content

We assessed how partial crystallization to cristobalite affects the strength of sintered silica without the complication of the β-α transformation by testing samples having never been cooled through the β-α transition. So we test discs which had been partially transformed to cristobalite by high temperature anneals, but never cooled below 350°C. These tests at 350°C allow the impact of the crystalline β-phase on strength to be examined independently from microfracture caused by the β-α transition. A large number of combinations of cristobalite content and strength were measured. These results were divided into ranges of cristobalite content. The mean and meadian diametral strength, open porosity, and number of observations for all these groupings can be seen in Table 4.1. The cumulative strength distributions for five cristobalite fractions are presented in Figure 4.2. Here the data collected at 350°C is labeled "Beta" for the phase of cristobalite at the testing temperature. It can be seen in Figure 4.2 that the strength distributions are overlapping suggesting β-cristobalite does not have a large impact on the strength of the sintered silica compacts. The 100th,75th,50th, 25th, and 10th percentile values for the 350°C strength are plotted in Figure 4.3 as a function of cristobalite content. There is not a consistent variation in strength as a function of cristobalite content. The strength of sintered silica is not significantly changed by crystallization to cristobalite at 350°C above the β-α transition.

4.4.3 Strength as a Function of α-Cristobalite Content

The impact of cristobalite content on strength at room temperature and the weakening effect of the β-α transition were also examined. Samples were cooled through the β-α transition and tested at 25°C. These results collected at 25°C are labeled “alpha” for the phase of cristobalite at this temperature. These results can be seen in Figure 4.2 and Table 4.1. Notice that the strength distribution of the samples tested at 25°C are all weaker than the strength distributions for the samples tested at 350°C, which had not undergone the β-α transformation. This becomes clearer when directly compared to the tests at 350°C. In Figure 4.4 separate plots for varying ranges of cristobalite content compare the 350°C β-cristobalite strength distributions to the α-cristobalite strength distributions at 25°C. It is apparent that the β-α transition dramatically weakens the sintered silica. The results in Figure 4.4 and Table 4.1 show that the relative strength of the α-cristobalite and the β-cristobalite diverge with increasing cristobalite content from 1-80% and then re-converge at the higher cristobalite contents of 80-100%. To better display this behavior the strength at 25°C is normalized by the strength at 350°C and plotted in Figure 4.5. In Figure 4.5(A) the mean strength found at 25°C (alpha) for each range is normalized by the 350°C (beta) strength. In Figure 4.5(B) the same is done for the 100th, 75th, 50th, and 25th percentile strengths. It can be seen that for the mean and above the 25th percentile strength the intermediate values of cristobalite content display the greatest degree of weakening. Sintered silica with 80-99% cristobalite content is consistently stronger than those with 40-80% cristobalite. Also, for the weakest 25th percentile there was no impact from cristobalite content suggesting that the weakest samples failed due to a critical flaw unrelated to cristobalite formation and transformation. The strength at 25°C (α-cristobalite) displays a strength minima between 40 and 80% cristobalite content.

The impact of small quantities of cristobalite on strength was established in material containing between 0-1% cristobalite. Material was fired at 1200°C for 8 hours. The density of these samples was 23.1±1.1% preventing comparison to more densely sintered material or the less densely sintered 0% cristobalite material. By QXRD the α-cristobalite (101) peak was indistinguishable from the background. However, based on prior kinetic studies we estimate there is a cristobalite phase fraction of <1%.[23] Figure 4.6 shows the cumulative strength distribution for material containing <1% cristobalite. It can be seen that the material is stronger when tested at 350°C prior to the β-α transformation than it is when tested at 25°C after the β-α transformation. This suggests the weakening effect from α-cristobalite is present even at a cristobalite contents of <1%.

4.4.4 Strength as a Function of β-Cristobalite Content Following β-α Transition

Many times refractories used in casting applications are fired, cooled, and subsequently heated during casting. Presumably the first transformation to α-cristobalite creates microcracks. Subsequent re-heating would transform the cristobalite back to the β-phase, but might not change the microcracks created by the prior β-α transformation. To evaluate strength of sintered silica in the β-cristobalite phase in material which had been previously cooled through the transformation to α-cristobalite, samples were cooled to 25°C following annealing, and then reheated to 350°C for testing. These samples are referred to as beta-alpha-beta in reference to their transformation history. In Figure 4.7 these beta-alpha-beta samples tested at 350°C are displayed alongside samples tested at 25°C (alpha) and samples tested at 350°C having never been cooled (beta). For samples with 20-40% cristobalite the beta-alpha-beta material has a strength distribution comparable to the "beta" material which had never been cooled. The beta-alpha-beta samples with 40-60% cristobalite appear to be stronger than the beta material which had never been cooled. When the sintered silica is fully crystalline, 100% cristobalite, the beta-alpha-beta samples have a strength distribution similar to the "alpha" samples tested at 25°C The strength of these samples tested in β-phase following the β-α transition normalized by the samples tested in β-phase having never passed the β-α transition can be seen in Figure 4.8. The 100th, 75th, 50th, and 25th percentile strengths of the beta-alpha-beta material tested at 350°C are normalized by the values from the 350°C tests on material never cooled to α-cristobalite. The samples tested at 350°C after having previously been cooled to α-cristobalite display an apparent strengthening for 40-60% cristobalite content. Also, the 25th percentile strength shows no dependence on cristobalite content as seen in Figure 4.5 for the 25°C and 350°C tests.

4.4.5 Microstructure

The sintered microstructure as imaged by secondary electron can be seen in Figure 4.9. In Figure 4.9(A) a polished cross section of epoxy impregnated material shows the structure of the material. The TECO-Sphere powder still retains its characteristic spherical particle morphology. The material is lightly sintered with limited particle to particle contact, retaining the appearance of sintered particles rather than a porous solid. Figure 4.9(B) is a fracture surface. The fracture has passed around the large spherical particles and we see no cracks passing through these larger particles. This confirms the appearance from Figure 4.9(A) that structurally the material is only lightly sintered and fails along the junctions between particles.

Using back-scatter electron imaging, BSE, the distribution of cristobalite can be seen with contrast provided by the small difference in density between the crystalline and amorphous phase. Figure 4.10 shows the progression of crystallization as cristobalite forms at the surface and develops into a shell around the amorphous core of the particles. It can be seen that at 50% cristobalite content a well developed cristobalite shell surrounds an amorphous core. In the particles displaying this core-shell morphology the cristobalite shell displays extensive micro-cracking. The cracks are seen to extend from the surface and terminate in the vicinity of the crystalline-amorphous boundary. The smaller fully crystalline particles, such as the adjoining particle in the lower left of Figure 4.10(C), do not display such cracking. This cracking presumably occurs as a result of the β-α transition; however, as all microscopy was done at room temperature the degree of cracking in the β-phase above 250°C is unknown.

4.5 Discussion:

4.5.1 Impact of Cristobalite Content on Strength

The strength of the sintered silica (with no cristobalite) was essentially the same at 25°C and 350°C. Thus for cristobalite-containing samples, we can attribute differences in the 25°C and 350°C strength to differences in α-cristobalite and β-cristobalite. Aside from the effect of the β-α transition, partial devitrification to cristobalite does not have a significant effect on strength. The strength distributions for samples tested at 350°C (never passed the β-α transition) did not change systematically with the amount of cristobalite. However, the transition to α-cristobalite dramatically reduced the strength of partially crystalline sintered silica compacts relative to β-cristobalite. Further, the weakening due to α-cristobalite occurred at very small crystalline contents. Figure 4.6 illustrates that samples held at a transformation temperature sufficient to nucleate cristobalite but displaying less than 1% by QXRD displayed only 80% the median strength value at 25°C as α-cristobalite as at 350°C as β-cristobalite.

Partially crystalline samples tested at 25°C as α-cristobalite had only about 80% of the strength of the β-cristobalite at 1% cristobalite. The strength of sintered silica with 40-60% α-cristobalite was as little as 35% of the strength of material with the same amount of β-cristobalite. This compares to the values reported by Kazemi et al. who found samples heat treated to transform to cristobalite had 75% of the flexural strength of those treated at lower temperature, which presumably had not crystallized. The weakening effect, as demonstrated in Figure 4.5, increased with increasing cristobalite content up to 40-60% after which relative strength in α-phase increased with increasing cristobalite content. At 100% cristobalite content samples tested as α-cristobalite displayed 64% the strength of samples having never passed the β-α transition. This reconvergence of strength can be understood in light of the microstructure as seen in Figure 4.10. Cristobalite surface nucleates and over the course of transformation forms a crystalline shell over an amorphous core as observed by others.[1, 2] For intermediate cristobalite contents this crystalline shell contracts around the static amorphous core on transition from β-cristobalite to α-cristobalite. This produces large tensile stresses in the shell resulting in microfracture. At higher cristobalite contents this facture is reduced as more particles become fully crystalline. This can be seen in Figure 4.10. Cracking can be seen in the cristobalite shell surrounding the amorphous core, but not in fully crystalline particles, such as the one in the lower left corner of Figure 4.10(C).

4.5.2 Impact of Passing β-α transition on Strength of β-cristobalite

As is clearly demonstrated in Figure 4.8 samples with 40-60% cristobalite which have been cooled to α-cristobalite and reheated to β-phase are in fact stronger than those samples that have never been cooled through the β-α transition. This behavior is surprising and unexpected as we had expected that the damage from microcracking during the first transformation to α-cristobalite would permanently weaken the material. However, we postulate that it can be explained in the context of the core-shell morphology observed in the microstructure. The transition from β-α in samples results in tensile stresses arising from the ~5% volume reduction accompanying the transformation. These tensile stresses are relieved by the microfracture seen in Figure 4.10. Upon reheating, the samples pass through the α-β transition with an accompanying volume increase of ~5%. If the original tensile forces have not been relieved this transition will apply equal and opposite compressive forces returning the material to a neutral state. However, if the original tensile forces have been partially relieved, this volume expansion leads to the development of compressive stress commensurate to the amount of tensile stress relieved by microfracture. In the case of a crystalline shell around an amorphous core these compressive stresses arising on the α-β transition will be concentrated at the surface just as the tensile forces were on the β-α transition. It is widely understood that compressive stress at the surface increases the strength of brittle materials by suppressing crack growth. At 100% cristobalite content, there is no amorphous core and the entire particle undergoes the volume change. Some microfracture occurs leading to the weakening seen in α-cristobalite, but this effect is smaller than for partially crystalline material. On reheating, no internal constraint is applied, consequently no surface compressive forces form and no strengthening is observed. The strengthening effect is observed to scale with cristobalite content in the opposite manner of the weakening effect seen in α-cristobalite. We posit this is due to the formation of surface compressive forces from the reversal of the tensile stress when it has been partially relieved by fracture.

4.6 Conclusions:

No difference in strength between 350°C and 25°C was observed for material containing no cristobalite. For cristobalite contents as low as <1% the material tested at 25°C as α-cristobalite was weaker than that tested at 350°C as β-cristobalite. The relative strength of the α-cristobalite relative to β-cristobalite was weakest for intermediate cristobalite contents displaying some recovery towards 100% cristobalite content. When tested at 350°C as β-cristobalite there was no observed impact of cristobalite content on strength. Material cooled to α-cristobalite and subsequently reheated and tested at 350°C as β-cristobalite was found to be stronger than material never cooled to α-cristobalite for intermediate cristobalite content. Microscopy revealed that cristobalite formed on the particle surface developing as a crystalline shell around an amorphous core. Extensive micro-cracking was observed in this crystalline shell that did not appear in fully crystalline particles.

4.7 References

1. A. A. Wereszczak, K. Breder, M. K. Ferber, T. P. Kirkland, E. A. Payzant, C. J. Rawn, E. Krug, C. L. Larocco, R. A. Pietras, and M. Karakus, "Dimensional changes and creep of silica core ceramics used in investment casting of superalloys," *J. Mater. Sci.*, 37[19] 4235-45 (2002).
2. A. Kazemi, M. A. Faghihi-Sani, and H. R. Alizadeh, "Investigation on cristobalite crystallization in silica-based ceramic cores for investment casting," *J. Eur. Ceram. Soc.*, 33[15-16] 3397-402 (2013).
3. A. Kazemi, M. A. Faghihi-Sani, M. J. Nayyeri, M. Mohammadi, and M. Hajfathalian, "Effect of zircon content on chemical and mechanical behavior of silica-based ceramic cores," *Ceram. Int.*, 40[1, Part A] 1093-98 (2014).
4. L. Y. Wang and M. H. Hon, "The effect of Cristobalite Seed on the Crystallization of Fused Silica Based Ceramic Core- A Kinetic Study," *Ceram. Int.*, 21[3] 187-93 (1995).
5. B. Taylor, S. T. Welch, and S. Blackburn, "Investigation into the Effect of Common Ceramic Core Additives on the Crystallization of Amorphous Silica," *Mechanical Properties and Performance of Engineering Ceramics and Composites VIII: Ceramic Engineering and Science Proceedings*, 34 (2013).
6. W. Crookes, "On the devitrification of silica glass," *Proc. R. soc. Lond. Ser. A-Contain. Pap. Math. Phys. Character*, 86[588] 406-08 (1912).
7. R. B. Sosman, "The Phases of Silica." Rutgers University Press, (1965).
8. D. R. Peacor, "High-temperature Single Crystal Study of Cristobalite Inversion," *Z. Kristall.*, 138 274-98 (1973).
9. E.-H. Kim, G.-H. Cho, Y. Yoo, S. Seo, and Y.-G. Jung, "Development of a new process in high functioning ceramic core without shape deformation," *Ceram. Int.*, 39[8] 9041-45 (2013).
10. M. Mellor and I. Hawkes, "Measurement of Tensile Strength by Diametral Compression of Discs and Annuli," *Engineering Geology*, 5[3] 173-& (1971).
11. H. Awaji and S. Sato, "Diametral Compressive Testing Method," *J. Eng. Mater. Technol.-Trans. ASME*, 101[2] 139-47 (1979).
12. M. K. Fahad, "Stresses and failure in the diametral compression test," *J. Mater. Sci.*, 31[14] 3723-29 (1996).
13. D. K. Shetty, A. R. Rosenfield, and W. H. Duckworth, "Mixed-Mode Fracture of Ceramics in Diamtetral Compression," *Journal of the American Ceramic Society*, 69[6] 437-43 (1986).
14. R. H. Marion and J. K. Johnstone, "Parametric Study of Diametral Compression Test for Ceramics," *Am. Ceram. Soc. Bull.*, 56[11] 998-1002 (1977).
15. J. T. Fell and J. M. Newton, "Determination of Tablet Strength by Diametral Compression Test," *Journal of Pharmaceutical Sciences*, 59[5] 688-& (1970).
16. F. L. L. B. Carniero and A. Barcellos, "Concrete Tensile Strength," *Union of Testing and Research Laboratories for Materials and Structures*[No. 13] (1953).
17. T. Akazawa, "Tension Method for Concrete," *International Association of Research Laboratories for Materials and Structures*[No. 16] (1953).

18. J. A. Hudson, F. Rummel, and E. T. Brown, "Controlled Failue of Rock Disks and Rings Loaded in Diametral Compression," *International Journal of Rock Mechanics and Mining Sciences*, 9[2] 241-& (1972).
19. R. M. Pilliar, M. J. Filiaggi, J. D. Wells, M. D. Grynpas, and R. A. Kandel, "Porous calcium polyphosphate scaffolds for bone substitute applications - in vitro characterization," *Biomaterials*, 22[9] 963-72 (2001).
20. M. B. Thomas, R. H. Doremus, M. Jarcho, and R. L. Salsbury, "Dense Hydroxyapatite Fatigue and Fracture Strength After Various Treatments, From Diametral Tests," *J. Mater. Sci.*, 15[4] 891-94 (1980).
21. T. Woignier and J. Phalippou, "Mechanical Strength of Silica Aerogels," *J. Non-Cryst. Solids*, 100[1-3] 404-08 (1988).
22. K. Gopalakrishnan and J. J. Mecholsky, "Quantitative Fractography of Mixed-Mode Fracture in Soda Lime Silica Glass," *Journal of the American Ceramic Society*, 95[11] 3622-27 (2012).
23. R. C. Breneman and J. W. Halloran, "Kinetics of Cristobalite Formation in Sintered Silica Glass," *Journal of the American Ceramic Society* (in revision 2014).

Table 4.1 Mean observed strength, porosity, and number of observations N for selected ranges of cristobalite content

	% Cristobalite	Median σ	Mean σ	Porosity	N
Alpha	0	0.46	0.5	25.1±0.4	10
	<1	1.94	2.17	23.1±1.1	10
	1-20	5.07	5.23	17.9±2.3	12
	20-40	2.45	4.63	17.9±2.3	14
	40-60	2.52	2.64	17.9±2.3	14
	60-80	2.66	2.67	17.9±2.3	6
	80-99	3.60	3.86	17.9±2.3	15
	100	5.85	6.06	13.8±1.2	14
Beta	0	0.451	0.52	25.1±0.4	13
	<1	2.44	2.90	23.1±1.1	8
	1-20	5.78	6.20	17.9±2.3	16
	20-40	7.40	8.48	17.9±2.3	14
	40-60	5.81	7.24	17.9±2.3	11
	60-80	6.48	6.97	17.9±2.3	15
	80-99	5.32	6.2	17.9±2.3	13
	100	9.19	9.54	13.8±1.2	12
Beta-Alpha-Beta	20-40	8.67	8.8	17.9±2.3	12
	40-60	9.25	9.5	17.9±2.3	10
	100	5.68	7.3	13.8±1.2	5

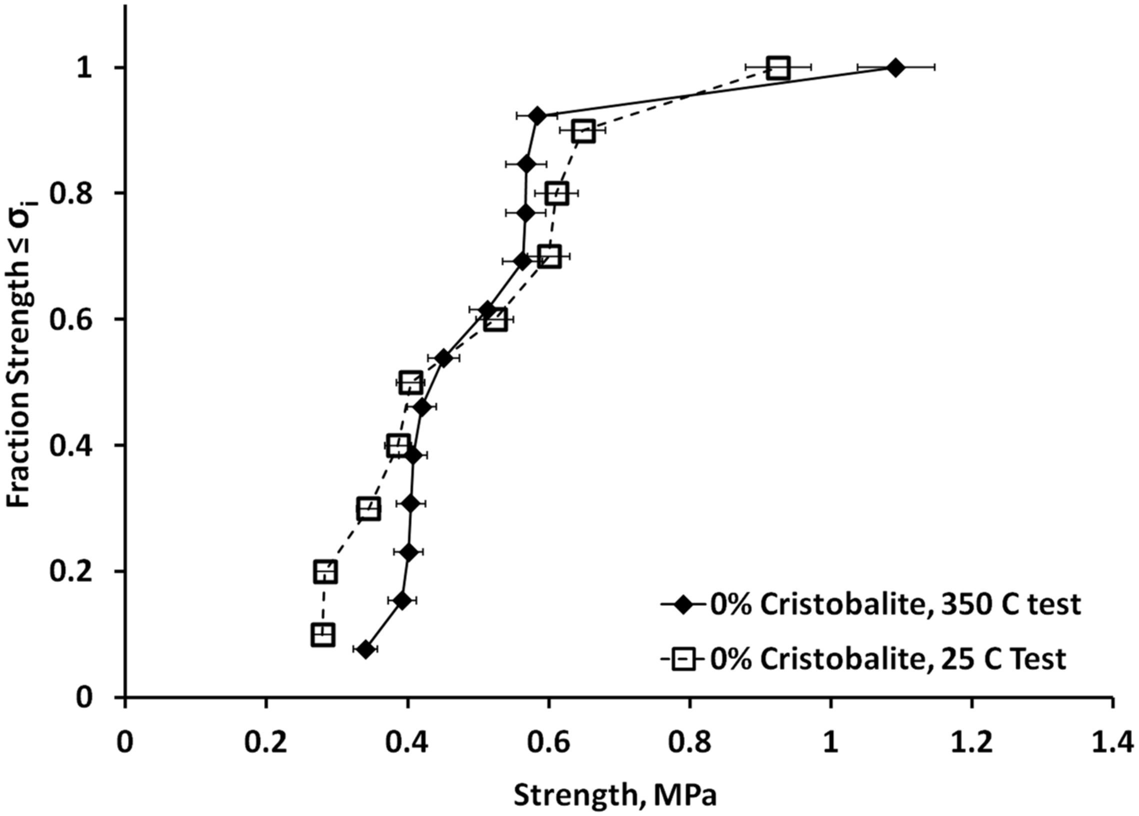

Figure 4.1 Cumulative strength distribution for samples with no cristobalite at 25°C and at 350°C.

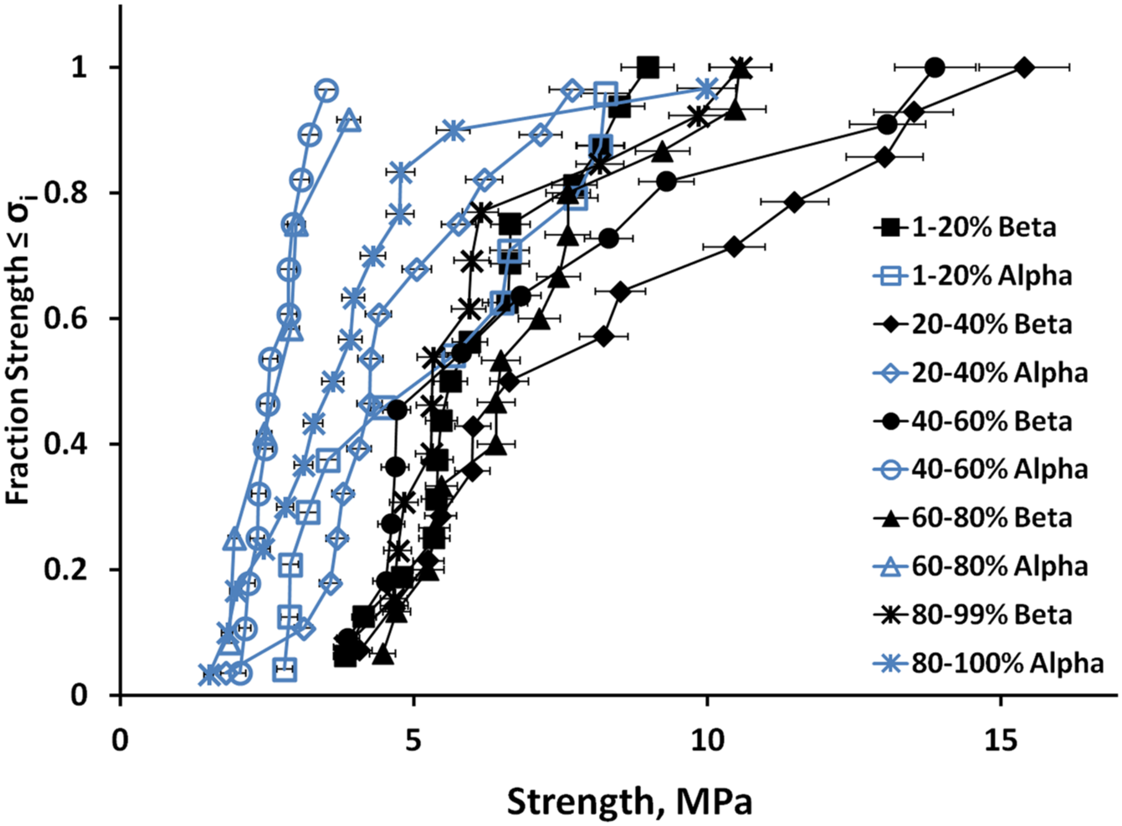

Figure 4.2 Strength distributions at 25°C when the cristobalite is α-cristobalite (Open symbols labeled "alpha") and 350°C when the cristobalite is β-cristobalite (Filled symbols labeled "beta")

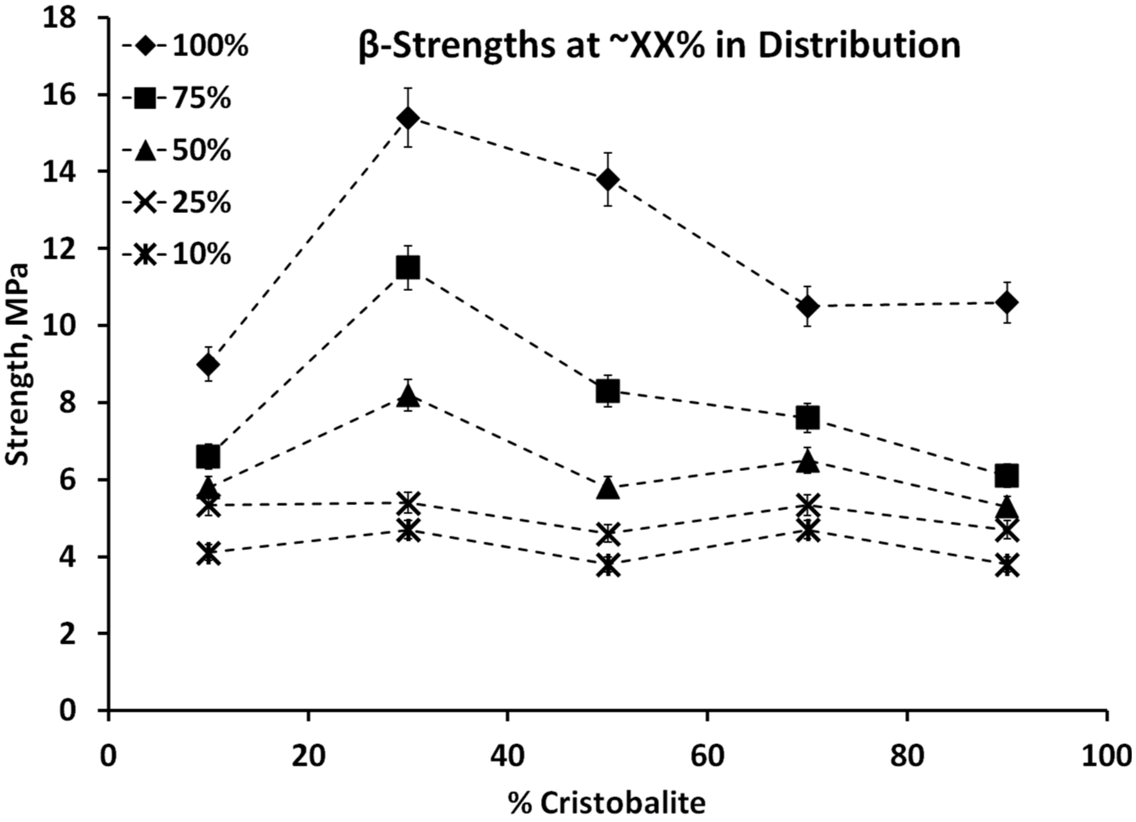

Figure 4.3 Strength of samples tested at 350°C (beta) for 10, 25, 50, 75, and 100 strength percentiles by cristobalite content. There is not a systematic change in strength with the amount of cristobalite.

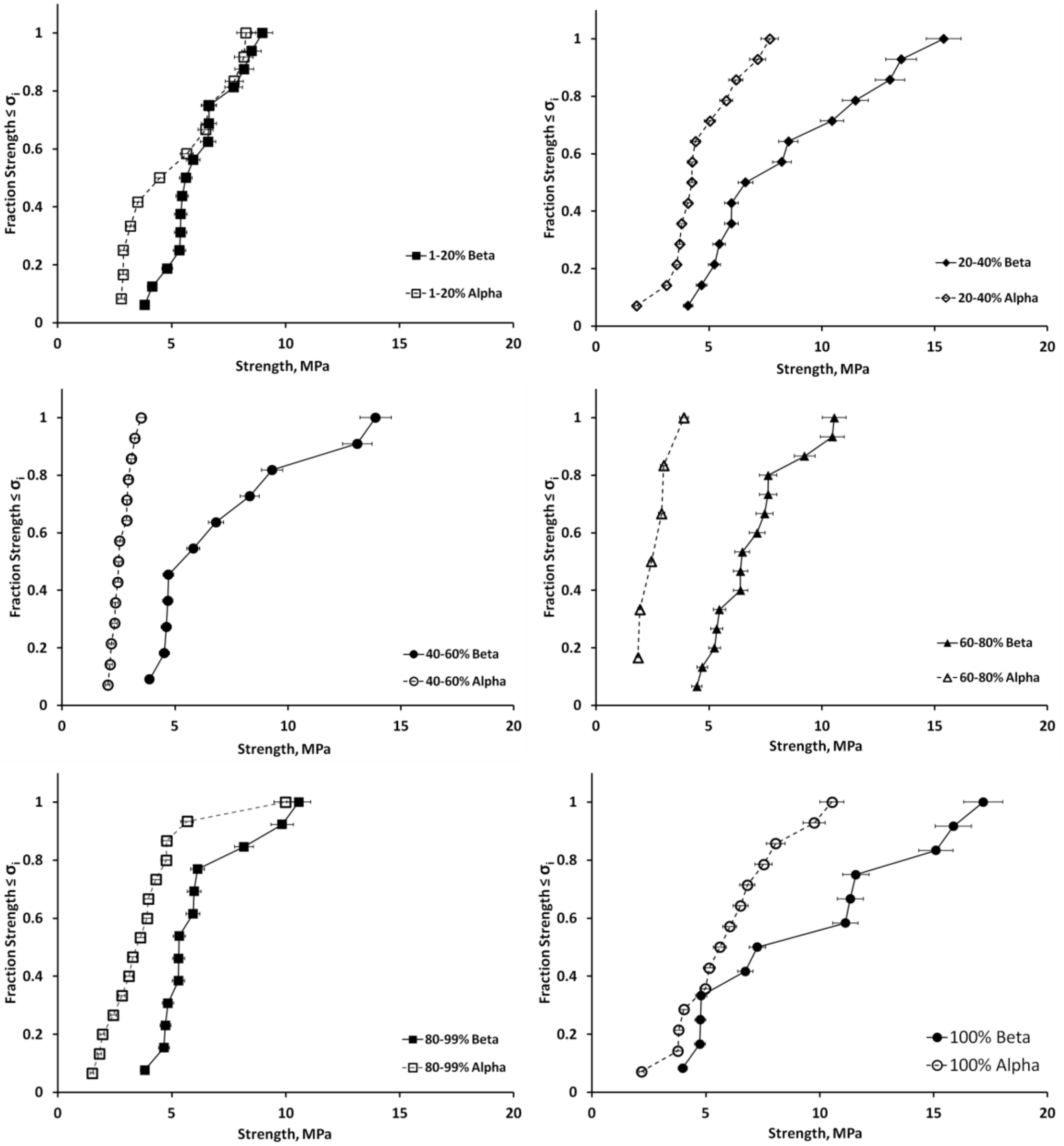

Figure 4.4 Cumulative strength distributions for samples tested at 25°C in the stable range for α-cristobalite and tested at 350°C in the stable range for β-cristobalite. Samples with 100% cristobalite have a higher sintered density compared with the other samples.

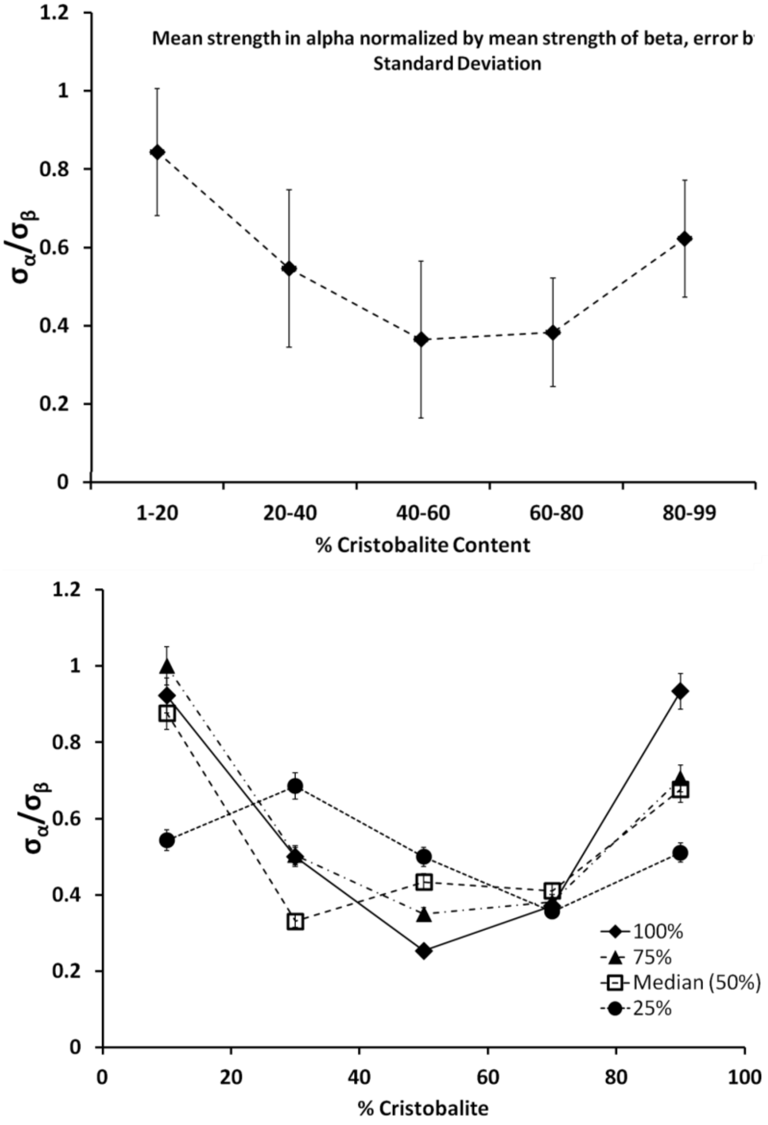

Figure 4.5 Strength at 25°C (alpha) relative to strength at 350°C (beta) plotted over cristobalite content ranges used in Fig.4.3 (A) Mean strength (B) 100th, 75th, 50th, and 25th Percentiles.

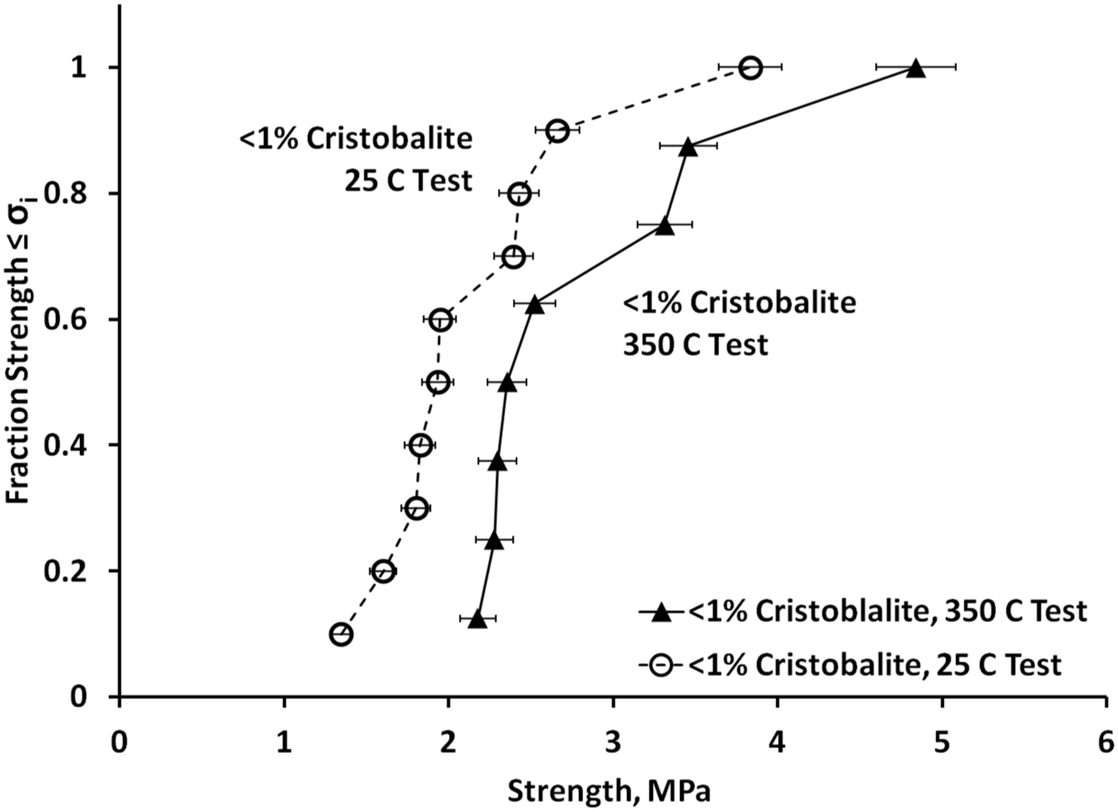

Figure 4.6 Cumulative strength distribution for samples with <1% cristobalite content tested at 25°C and tested at 350°C.

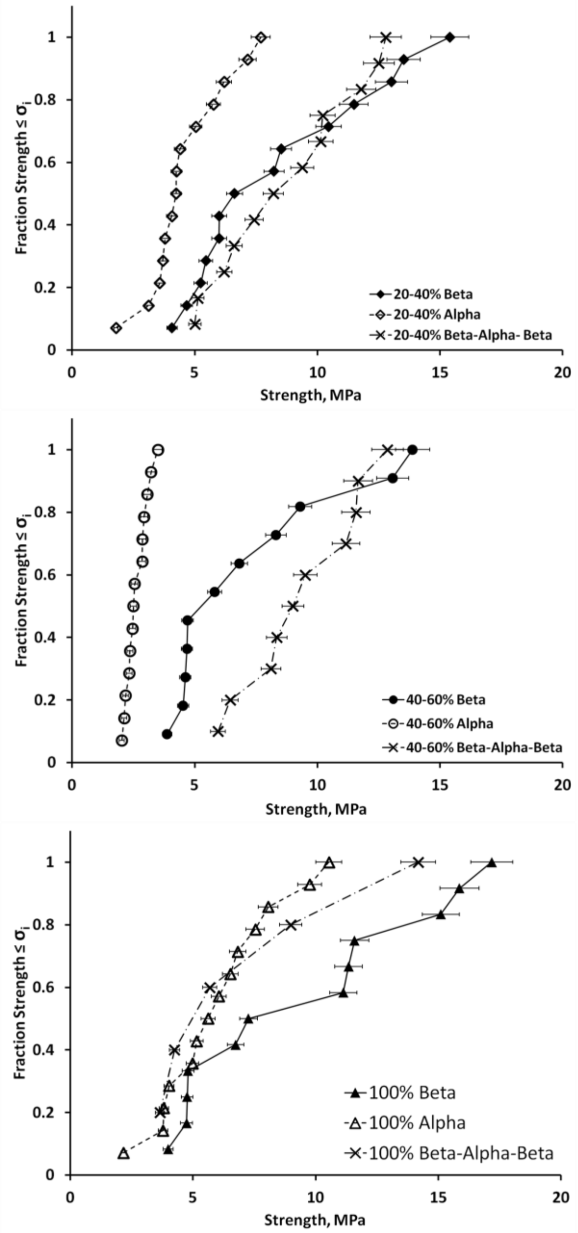

Figure 4.7 Cumulative strength for samples tested at 25°C (alpha), tested at 350°C (beta), and tested at 350°C after previously having been cooled to 25°C (beta-alpha-beta).

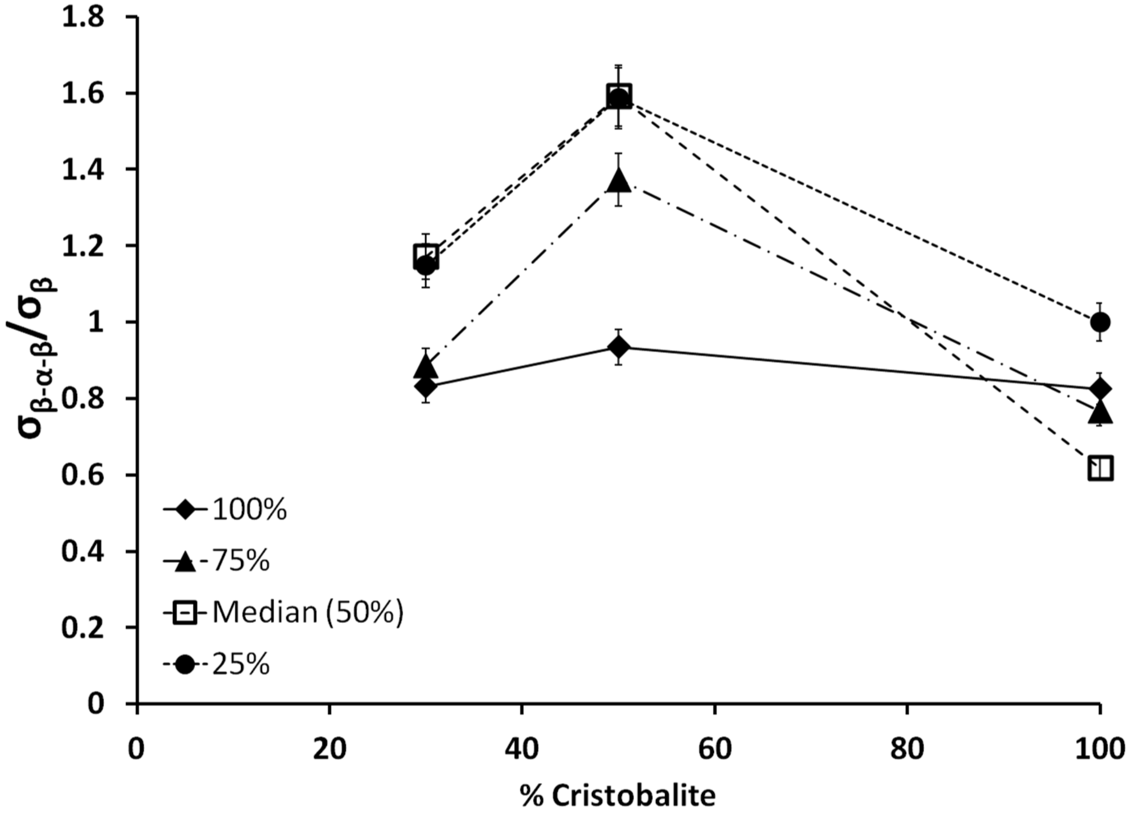

Figure 4.8 100th, 75th, 50th, and 25th percentile strength at 350°C of samples having previously passed the β-α transition (beta-alpha-beta) relative to strength at 350°C without cooling (beta) plotted over cristobalite content ranges used in Fig. 4.6.

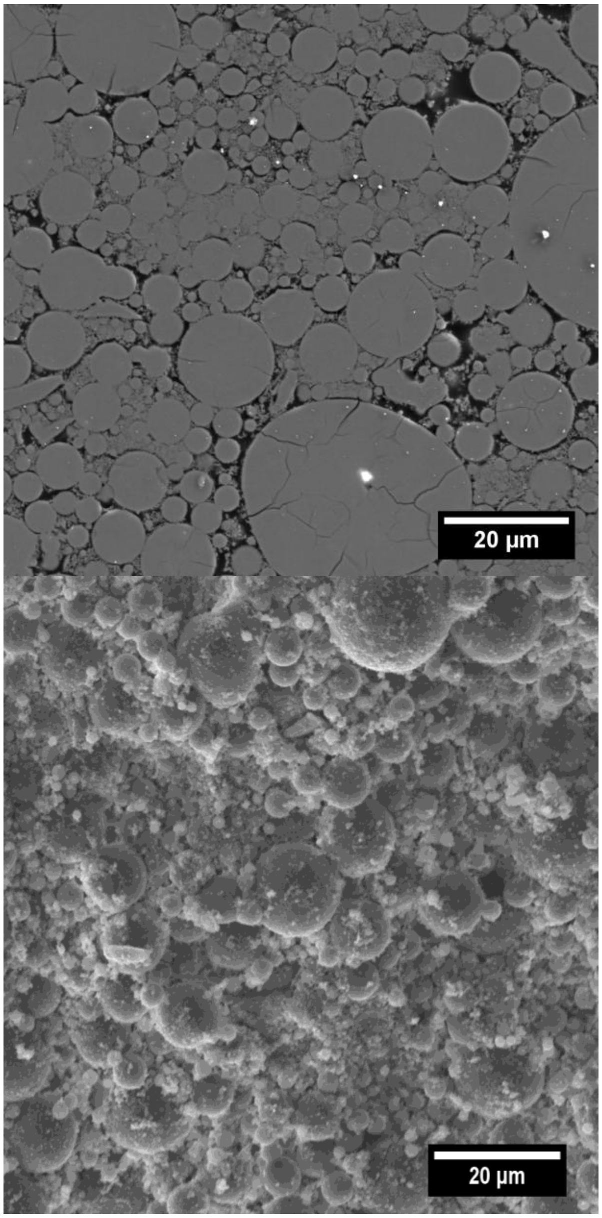

Figure 4.9 SEM of microstructure by secondary election, SE, imaging. (A) Polished cross-section (B) Fracture surface.

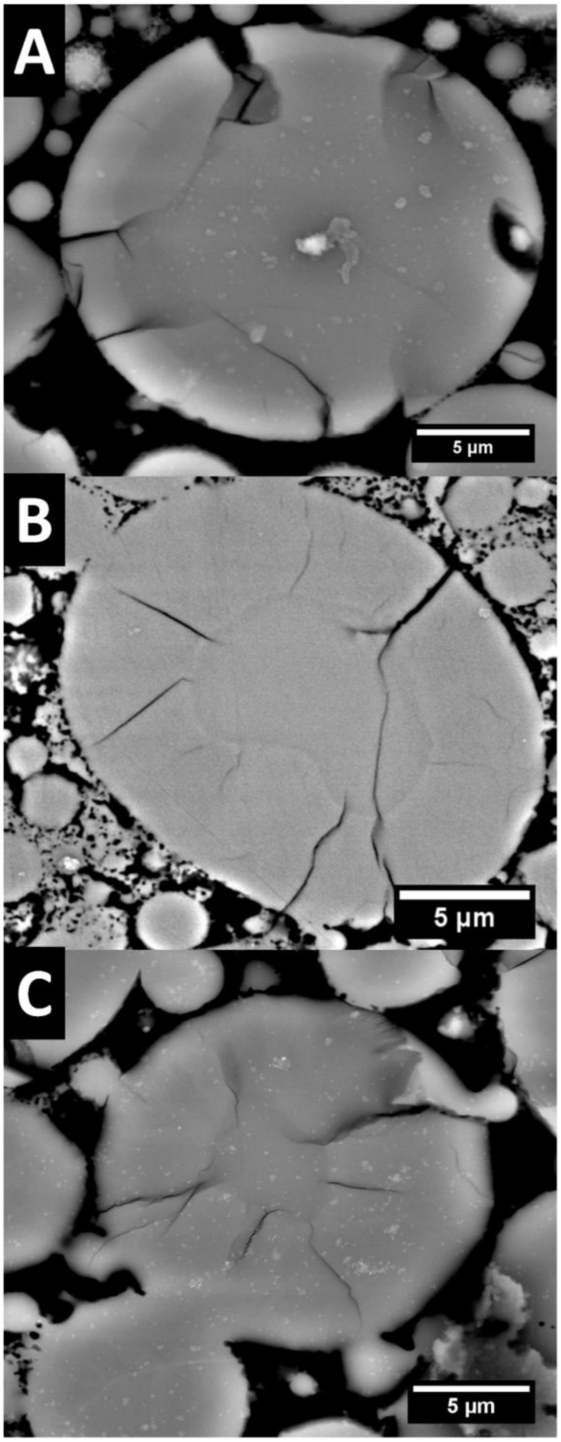

Figure 4.10 SEM of microstructure by back-scatter electron, BSE, illustrating development of cristobalite morphology. Cristobalite is observed to surface nucleate and grow as a crystalline "shell" around the amorphous silica "core." Cristobalite content of (A) 11%, (B) 50%, (C) 84%

Chapter 5
Repeated Cycling of the β-αTransition of Cristobalite

5.1 Preface

The impact of passing through the β-α transition was an important topic for optimizing the sintering of LAMP molds. Over the course of looking at the transition the question of what happens on repeated β-α and α-β cycles was raised. The topic has not been reported in the literature despite a wealth of information on other aspects of the transformation behavior. In order to determine the effect of cycling through the β-α transition, samples were cycled from 190°C to 280°C and back 50 times in a differential scanning calorimeter. The impact of repeated cycling through the β-α transition on the onset temperature of the transformation and transformation enthalpies were observed.

5.2 Introduction

Like other silicate crystal structures, cristobalite exhibits a higher symmetry form at high temperature and undergoes a transformation to a lower symmetry form at low temperature.[1] In cristobalite the high temperature, cubic β-cristobalite structure is the stable structure for silica from 1470 to 1625°C but persists meta-stably to lower temperatures. It undergoes a first order, displacive transformation to tetragonal α-cristobalite between 275 and 200°C.[2, 3, 4] The transformation temperature is highly variable and dependent the thermal history of material as noted by Wyckoff in 1925[2] and Hill and Roy in 1958.[5] The exact nature of the transition and the precise structure of β-cristobalite itself remains an active area of research. The cubic structure of β-cristobalite was first reported by Wyckoff[2] in 1925, but in 1937 Nieuwenkamp[3] proposed the structure is actually dynamically disordered at a local level. As observed by several authors, notably, Wright and Leadbetter in 1975[6], the ideal cubic structure results in bond angles and lengths atypical for SiO2. This topic has been examined with a range of experimental techniques, including TEM by Withers et a,.[7, 8] NMR by Spearing et al,[9] neutron diffraction by Dove et al,[10] and Raman spectroscopy by Swainson et al.[11] The transformation has been treated by Schmal et al[12] using a Landau free energy approach, while Swainson and Dove[13] and Huang et al[14, 15] used MD simulation, and Cope and Dove[16] used a Pair Distribution Function Approach. The general conclusion is drawn that β-cristobalite, while retaining cubic symmetry, is dynamically disordered, but the details continue to be actively researched.

The transition from β-to-α is accompanied by a 4.9% volume reduction[4] leading to a dependence on stress. The effect of hydrostatic pressure was studied by Cohen and Klemment in 1975,[17] and other aspects of the role of the stress state on the transition has been explored by Parise et al in 1994,[18] Lee and Lee in 2001[19], and Chao and Lu in 2002.[20] The origin of this hysteresis was reported on in detail by Schmal in 1993.[21, 22]

In this paper we are interested in the role of thermal history on the hysteresis for this transformation. In particular, we investigate how repeated cycling changes the hysteresis of the transition from the low temperature α-cristobalite to β-cristobalite on heating, and the reverse transition from β-cristobalite to α-cristobalite on cooling. We will report that the transition temperature of the α-to-β endotherm upon heating and β-to-α exotherm on cooling changes stystematically with repeated cycling. The transformation enthalpy does not change with repeated cycling, although the β-α exotherm is consistently larger than the α-to-β endotherm. We will present evidence that this is related to dissipation of stresses associated with the volume change of the transformation.

5.3 Procedure:

5.3.1 Materials:

We used a commercial amorphous silica powder, (TECO-Sphere-Microdust, CE Minerals, Greenville, TN) which is 99.7% silica with primary contaminants of alumina and iron oxide. The powder is spherodized by a drop-melt process, resulting in a distribution of 5-25 micron particles of roughly spherical shape. Details of the powder characteristics were previously reported.[23]

Phase pure cristobalite was produced by the procedure of Wang and Hon.[24] The powder was annealed under lab air at 1550°C for 24 hours followed by grinding, annealed at 1550°C for 12 hours followed by grinding, and annealed again for 12 hours. Thus the material for our first cycle of heating in the DSC had been heated and cooled three times, and had experienced three β-α transitions before DSC and one transition since last annealing at 1550°C. Size fractions were produced by sieving the powder to collect fractions with the following particle size ranges: coarser than 425 microns, 150-425 microns, 106-150 microns, 38-106 microns, and finer than 38 microns.

5.3.2 Calorimetry

Calorimetry was conducted on a TA Q2000 Differential Scanning Calorimeter (TA Instruments-Waters LLC, New Castle, DE), calibrated with the melting point of indium and heat capacity of sapphire. Transition enthalpies were obtained with the TA

Platinum^{TM} DSC software. A sample of powder was sealed in Tzero^{TM} aluminum hermetic DSC pan and a hole was punctured to allow the escape of gas. Nitrogen was used as a cover gas. Testing was conducted by cycling the material from 190°C to 280°C with heating/cooling rates of 3°C/minute, for up to 50 cycles. The onset temperature for the α-β exotherm is defined as the temperature where the heat flow reached 25% of the exothermic peak of that cycle. The onset temperature for the α-β endotherm is defined as the temperature where the heat flow reached 25% of the endothermic peak of that cycle. Note that the DSC calorimetry was for α-cristobalite prepared by multible heatings, so it had already been transformed from β-to-α during cooling from its 1550°C crystallization temperature. What we call "cycle 1" is the first heating cycle we recorded in the calorimeter.

5.4 Results:

5.4.1 Influence of Repeated Cycles on the β-αTransition

The DSC curves for cycle 1 and cycle 50°Can be seen in Figure 5.1. On heating from 190°C to 280°C an endothermic peak corresponding to the α-β transition can be observed at 259-261°C, while on cooling an exothermic peak corresponding to the β-α transition is observed at 235-239°C. The DSC curves for cycle 1 and cycle 50 are compared in Figure 5.1.

For cycle 1, the onset temperature for the endothermic α-to-β transition during heating occurred at 259.4^{o}C and the endotherm was complete around 263^{o}C. Upon cooling, the onset temperature for the exothermic β-to-α transition on cooling occurred at 236.8^{o}C and was complete around 234^{o}C. There was a 22.6^{o}C hysteresis for the onset temperatures for the exotherm and endotherm for cycle 1. For cycle 50, the α-β endotherm upon heating had an onset temperature of 259^{o}C the β-α exotherm onset upon cooling occurred at 238.7^{o}C. The hysteresis at cycle 50 was 20.3^{o}C, which was smaller than the onset hysteresis for cycle 1. The width of the thermal events, from onset to finish, is broader by about 40% after cycle 50, indicating an increased range of phase coexistence. The onset of the α-β endotherm increased by 0.4^{o}C after 50 cycles, while the onset of the β-α exotherm changed by +1.9^{o}C after 50 cycles.

Details of the endothermic and exothermic events for ten selected cycles appear in Figure 5.2, which compares the endotherm for α-β (Figure 5.2a) and the exotherm for β-α (Figure 5.2b) for the first three cycles 1, 2, 3 with cycles10, 20, 30, 40, and with the last three cycles 48, 49, and 50. The cooling β-α exotherms broaden and move to incrementally lower temperatures, while the heating α-β endotherms, broaden more, and have a larger temperature increment.

The transformation enthalpy, determined by integration of the thermal events by the DSC software, does not change with cycling. Figure 5.3 displays the enthalpies as J/g, and it is apparent that there is no change. The enthalpy for the β-α exotherm, L(β-α), was 1560±27 J/mol while the enthalpy for α-β endotherm, L(α-β), was 1260±8 J/mol. Note the substantial difference between the exotherm and the endotherm, which is about 300 J/mole or about 20%. This large difference indicates a significant dissipation of energy during the transformation of β-cristobalite to α-cristobalite.

The onset temperature of the exotherm corresponding to the β-α transition increased systematically with the number of cycles. This increase of temperature of the exotherm onset corresponds to a decrease in the undercooling of the transformation. The temperature of onset is plotted in Figure 5.4. The onset temperature increases monotonically, can be fit to the following relation:

$$T_{onset}^{\beta-\alpha} = 236.8 + 0.473ln(n) \qquad Eq. 5.1$$

In which n is the cycle number. This implies there is an incremental increase in the temperature of transformation to α which diminishes with the number of cycles with a logarithmic decrement of 0.473, or

$$\frac{\partial T_{onset}^{\beta-\alpha}}{\partial n} = \frac{+0.473^{o}}{n} \qquad Eq. 5.2$$

This corresponds to less hysteresis and a reduced super-cooling required to transform implying a lower driving force necessary for the transformation with each passing cycle.

The onset temperature of the endotherm corresponding to the α-β transformation was established by the same method as the exotherm and is plotted in Figure 5.5. The onset temperature was observed to increase with each cycle for 20 cycles after which it stabilizes at 258.9±0.03°C. This corresponds to a decrease in super heating. It was found to fit a logarithmic function through 20 cycles prior to stabilizing.

$$T_{onset}^{\alpha-\beta} = 259.5 - 0.183ln(n) \qquad Eq. 5.3$$

In which n is the cycle number. This implies there is an incremental decrease in the temperature of transformation to β-cristobalite which diminishes with the number of cycles with a logarithmic decrement of 0.183, or:

$$\frac{\partial T_{onset}^{\alpha-\beta}}{\partial n} = \frac{-0.183^{o}}{n} \qquad Eq. 5.4$$

Thus the α-β transformation exhibits a logarithmic decrease in driving force necessary for the transformation with each passing cycle until stabilizing after 20 cycles.

5.4.2 Influence of Particle Size on Behavior with Repeated Cycles

It is known that in order to accommodate the strain of the β-α transition the material undergoes extensive microfracture and twinning. It has previously been reported that cristobalite twinning displays no memory on repeated transformation.[7] This leaves continued microfracture as the likely mode of continued decrease in the driving force required to transform. If the cycling effect is indeed due to a continued microfracture, it is possible there exists a critical particle size, d_{crit}, at which the material is as finely broken as it can be and no cycling effect will occur. To test this, the powder was sieved into the following size fractions: 150-425 microns, 106-150 microns, 38-106 microns, and finer than 38 microns. Samples from each fraction were cycled for 50 cycles. The DSC curves for cycles 1 and 50 for the finer than 38 micron fraction and the 150-425 fraction can be seen in Figure 5.6. The fraction finer than 38 microns has no change in hysteresis over 50 cycles, while the coarser fraction has a noticeable change in hysteresis after 50 cycles. The change in β-α onset for sieved fractions and the whole powder are reported in Figure 5.7. For the larger particle fractions, the onset temperature increased, so the under-cooling decreased, on cycling. Particles smaller than 38 micron do not show a cycling effect, while those with sizes 38-106 micron do. This suggests that a d_{crit} exists and falls between 106 and 38 microns. The middle course size fractions, 150-106 microns and 106-38 microns, actually have a larger logarithmic increment of 0.72±0.04 than the whole powder.

5.5 Discussion:

5.5.1 Hysteresis of the β-α Transition

The hysteresis in the transformation between the β and α phases of cristobalite is probably related to volume change. There is a significant strain energy associated with the initial nucleation of the new phase in the host phase during both the β-α and α-β transitions. Overcoming this strain energy requires an associated driving force which manifests as a transformation hysteresis. In addition to this unavoidable localized effect, there is a macroscopic stain associated with the transformation. As reported by others, the phase transformation is responsive to the macroscopic stress state and particle size of the material.[17, 18, 19, 20, 25] We believe the change in hysteresis on cycling is the alleviation of some of this macroscopic stress by microfracture. Microfracture can reduce overall constraint on the transformation and lower the barrier to transformation.

Theoretically the reduced hysteresis on cycling faces an inherent limit of the reduction to no transformation hysteresis. In this system, the limit is the point at which further fracture is no longer possible. Given the local stress due to volume change on transformation one expects there will always be hysteresis, even for very fine particles. The observed decay in the incremental change as the hysteresis decreases towards a limit of minimum hysteresis is expected. That the decay in the incremental change on transformation temperate behaves logarithmically is an exciting but not surprising observation. Decay to an equilibrium state is often observed to occur logarithmically. The β-α transition exhibits a larger change on cycling of 0.473°C/n and continues to change monotonically for 50 cycles. The α-β transition, on the other hand, exhibits a smaller change on cycling of -0.183°C/n and stabilizes after 20 cycles. This suggests that the ideal transformation temperature at which no hysteresis would be observed is nearer to of 260°C, the observed temperature of the α-β transition, than to ~237°C, the observed temperature of the β-α transition.

The enthalpy of transformation differs between the transformation from β-α and from α to β, as reported by others.[26, 27, 28, 29] We found the enthalpy of transformation from β to α to be 1560±27 J/mol and the enthalpy of transformation from α to β to be 1260±8 J/mol. This falls at the higher end of the range found in the literature of 1100-1430 J/mol for β-α and 1020-1280 J/mol for α to β, perhaps indicative of the effect of the relatively low purity of material used in this study.[12, 26, 30] The difference in enthalpy between the β-to-α and α-to-β transitions was found to be invariant across cycling even as the onset temperatures changed and hysteresis lessened. This suggests the magnitude of the difference in enthalpy is unrelated to the magnitude of hysteresis.

5.5.2 Change in Transition Temperature on Repeated Cycling

The transformation onset temperatures were observed to change on cycling by an increment that decreased logarithmically. The change in onset temperature observed corresponds to a reduction in under-cooling required to drive the β-α transition and a reduction in the super-heating required to drive the α-β transition. This corresponds to a reduced transformation hysteresis and reduced driving force required to transform. The impact of cycling NiTi through the martensitic phase transformation was investigated by McCormick and Liu in 1994. They found the onset temperature of the transformation on heating and on cooling both decreased logarithmically with the difference between onset temperatures remaining constant. The transformation enthalpy was also found to decrease. In all respects aside from the logarithmic change in onset this differs from our observations of the β-α transition of cristobalite suggesting different mechanisms are at work.

Let us consider the elastic strains from the volume change of the transformation to be equivalent to a pressure. Then by the Clausius-Clapeyron equation, we would expect the change pressure-induced change in transformation temperature to be related to the enthalpy and volume change:

$$\frac{\mathrm{dP}}{\mathrm{dT}} = \frac{\Delta\mathrm{H}}{\mathrm{T}\Delta\mathrm{V}} \qquad Eq. 5.5$$

or its inverse:

$$\frac{\mathrm{dT}}{\mathrm{dP}} = \frac{\mathrm{T}\Delta\mathrm{V}}{\Delta\mathrm{H}} \qquad Eq. 5.6$$

for how the transformation temperature changes with pressure (where here the "pressure" is the unrelieved transformation stress.) A chain rule analysis on the inverse Clausius Clapeyron to get the temperature change per cycle:

$$\frac{\mathrm{dT}}{\mathrm{dP}}\frac{\mathrm{dP}}{\mathrm{dn}} = \frac{\mathrm{T}\Delta\mathrm{V}}{\Delta\mathrm{H}}\frac{\mathrm{dP}}{\mathrm{dn}} = \frac{\mathrm{dT}}{\mathrm{dn}} = \frac{\beta}{\mathrm{n}} \qquad Eq. 5.7$$

where β/n is the empirical dependence of transformation temperature changing with cycle number. We observe a change in transformation temperature with cycle dT/dn= β/n, where the empirical value for b is +0.473 for the β-α exotherm and -0.183 for the α-β endotherm. Perhaps this observed dT/dn is related to a ratcheting of the unrelieved stress. Let W= the fractional change in unrelieved stress per cycle, then W= dP/dn:

$$\frac{\mathrm{dP}}{\mathrm{dn}} = \frac{\Delta\mathrm{H}}{\mathrm{T}\Delta\mathrm{V}}\frac{\beta}{\mathrm{n}} = \mathrm{W} \qquad Eq. 5.8$$

and the observed change in dT/dn may imply that the incremental fraction of stored strain energy diminishes as 1/n.

The transformation on cooling from β-to-α is associated with a volume reduction and the development of a tensile strain. This tensile strain can be partially relieved by microfracture. The transition from β-to-α also includes a loss of symmetry from cubic to tetragonal and extensive twinning.[7, 12, 31] Conversely, the α-to-β transition on heating is associated with a volume expansion and alleviation of the prior twinning. Some fraction of this expansion will be accommodated by the closing of the cracks formed on the β-α transition, some may be balanced by retained tensile stress, and the remainder will develop as a compressive stress. At the low temperatures used in this study no relaxation of stress by thermal annealing was possible.

We believe the reduced hysteresis is the result of continued microfracture reducing the macroscopic constraints on the volume change associated with the transformation. Fracture reduces volumetric constraint from surrounding material, lessening the stress or internal pressure associated with transformation. Thus continued microfracture on each cycle could reduce the stored strain energy associated with transformation and reduce the driving force needed to transform. It has previously been reported that twinning does not show any memory on repeated transformation suggesting that twinning mechanisms cannot be responsible for the observed decrease in hysteresis on cycling. The continued microfracture mechanism is corroborated by the results from the powder fractions of varying size. It was found that below a critical size no cycling effect was observed. If the cycling effect was caused by a microstructural phenomena such as the training of the material by repeated twinning there is no reason for the effect to be absent in particles 38 microns in size. However, if the cycling effect is due to continued microfracture one does expect that for a certain size cracking will no longer occur and no effect from cycling will be seen. The lack of any impact of cycling on hysteresis for powder with 38 micron or finer particles suggests this size falls below the critical size necessary for microfracture.

5.6 Conclusions:

Repeated cycling of sintered cristobalite powder was observed to display a decrease in the endotherm onset temperature and an increase in the exotherm onset temperature, reducing the transformation hysteresis. The temperature of the β-α transition was found to follow $T_{onset}^{\beta-\alpha} = 236.8 + 0.473 ln(n),$ while the temperature of the α-β transition was found to follow $T_{onset}^{\alpha-\beta} = 259.5 - 0.183 ln(n).$ The logarithmic decrement suggests a change in the transformation strain energy follows ~1/N. This decrease in the required super heating and cooling respectively indicates a lower energy barrier to transformation. It was found that for powders below a critical particle size between 106 and 38 microns no cycling effect occurred. This suggests the possibility that the cycling effect is caused by continued microfracture which cannot occur below a critical particle size.

The enthalpy of transformation was found to be 600 J/g greater for the β-to-α than the α-to-β transition. The enthalpy did not change on cycling even as transformation hysteresis was reduced.

5.7 References

1. R. B. Sosman, "The Phases of Silica." Rutgers University Press, (1965).
2. R. W. G. Wyckoff, "The crystal structure of the high temperature form of Cristobalite," *American Journal of Science,* 9[54] 448-59 (1925).

3. W. Nieuwenkamp, "On the structure of β-cristobalite," *Z. Kristall.,* 96[6] 454-58 (1937).
4. D. R. Peacor, "High-temperature Single Crystal Study of Cristobalite Inversion," *Z. Kristall.,* 138 274-98 (1973).
5. V. G. Hill and R. Roy, "Silica Structure Studies. 5. The Variable Inversion in Cristobalite," *Journal of the American Ceramic Society,* 41[12] 532-37 (1958).
6. A. F. Wright and A. J. Leadbetter, "Structures of Beta-Cristobalite Phases of SiO2 and AlPO4," *Philosophical Magazine,* 31[6] 1391-401 (1975).
7. R. L. Withers, J. G. Thompson, and T. R. Welberry, "The Structure and Microstructure of Alpha-Cristobalite and its Relationship to Beta-Cristobalite," *Physics and Chemistry of Minerals,* 16[6] 517-23 (1989).
8. R. L. Withers, T. R. Welberry, G. L. Hua, J. G. Thompson, and B. G. Hyde, "A Transmission Electron-Microscopy Study of Cristobalite," *Phase Transitions,* 16 41-45 (1989).
9. D. R. Spearing, I. Farnan, and J. F. Stebbins, "Dynamics of the Alpha-Beta Phase-Transitions in Quartz and Cristobalite as Observed by Insitu High-Temperature Si-29 NMR and 0-17 NMR," *Physics and Chemistry of Minerals*, 19[5] 307-21 (1992).
10. M. T. Dove, D. A. Keen, A. C. Hannon, and I. P. Swainson, "Direct measurement of the Si-O bond length and orientational disorder in the high-temperature phase of cristobalite," *Physics and Chemistry of Minerals*, 24[4] 311-17 (1997).
11. I. P. Swainson, M. T. Dove, and D. C. Palmer, "Infrared and Raman spectroscopy studies of the alpha-beta phase transition in cristobalite," *Physics and Chemistry of Minerals*, 30[6] 353-65 (2003).
12. W. W. Schmahl, I. P. Swainson, M. T. Dove, and A. Graemebarber, "Landau Free-Energy and Order Parameter Behavior of the Alpha/Beta Phase-transition in Cristobalite," *Z. Kristall.*, 201[1-2] 125-45 (1992).
13. I. P. Swainson and M. T. Dove, "Molecular Dynamics Simulation of Alpha-Cristobalite and Beta-Cristobalite," *J. Phys.-Condes. Matter,* 7[9] 1771-88 (1995).
14. L. Huang, M. Durandurdu, and J. Kieffer, "Transformation Pathways of Silica Under Pressure," *Nature Materials*, 5 977-81 (2006).
15. F. L. Yuan and L. P. Huang, "Alpha-Beta Tansformation and Disorder in Beta-cristobalite Silica," *Phys. Rev. B,* 85[13] (2012).
16. E. R. Cope and M. T. Dove, "Evaluation of domain models for beta-cristobalite from the pair distribution function," *J. Phys.-Condes. Matter,* 22[12] 7 (2010).
17. L. H. Cohen and W. Klement, "Differential Thermal-Analysis Investigation of High-Low Cristobalite Inversion Under Hydrostatic-Pressure to 7 Kbar," *Journal of the American Ceramic Society*, 58[5-6] 206-08 (1975).
18. J. B. Parise, A. Yeganehhaeri, D. J. Weidner, J. D. Jorgensen, and M. A. Saltzberg, "Presure Induced Phasetransition and Pressure Dependence of Crystal-Structure in Low (alpha) and Ca/Al-Doped Cristobalite," *J. Appl. Phys.,* 75[3] 1361-67 (1994).
19. S. J. Lee and S. H. Lee, "Behavior of induced phase transformation of beta-cristobalite by shear stress," *J. Mater. Sci. Lett.*, 20[2] 135-37 (2001).

20. C. H. Chao and H. Y. Lu, "Stress-induced beta ->alpha-cristobalite phase transformation in (Na2O+Al2O3)-codoped silica," *Mater. Sci. Eng. A-Struct. Mater. Prop. Microstruct. Process.,* 328[1-2] 267-76 (2002).
21. W. W. Schmahl, "Athermal Transformation Behavior and Thermal Hysteresis at the SiO2-Alpha/Beta-Cristobalite Phase-Transition," *Eur. J. Mineral.,* 5[2] 377-80 (1993).
22. W. W. Schmahl, "Hysteresis and Phase Coexistence at the SiO2 alpha/beta-cristobalite Phase Transition and the Pitfalls of PSD Callibration," *Materials Science Forums*, 133-136 (1993).
23. R. C. Breneman and J. W. Halloran, "Kinetics of Cristobalite Formation in Sintered Silica Glass," *Journal of the American Ceramic Society* (in revision 2014).
24. L. Y. Wang and M. H. Hon, "The effect of Cristobalite Seed on the Crystallization of Fused Silica Based Ceramic Core- A Kinetic Study," *Ceram. Int.*, 21[3] 187-93 (1995).
25. S. J. Lee and C. H. Lee, "Critical size effect for chemically doped beta-cristobalite transformation," *Mater. Lett.,* 45[3-4] 175-79 (2000).
26. P. Richet, Y. Bottinga, L. Denielou, J. P. Petitet, and C. Tequi, "Thermodynamic Properties of Quartz, Cristobalite, and Amorphous SiO2," *Geochimica Et Cosmochimica Acta,* 46[12] 2639-58 (1982).
27. A. B. Thomson and M. Wennemer, "Heat Capacities and inversions in tridymite, cristobalite, and tridymite-cristobalite mixtures," *Amer. Mineral.,* 64 (1979).
28. G. Sabatier, "Chaleurs de transition des formes de basse temperature aux formes de haute temperature du quartz, de la tridymite, et de la cristobalite," *Bull.Soc.Frances Mineral Cristallography,* 80 337-44 (1957).
29. T. W. Smith, "Some Structural and Thermodynamic Studies of alpha-beta phase transformations." in. University of Bristol, 1972.
30. M. A. Butler and D. J. Dyson, "The quantification of different forms of cristobalite in devitrified alumino-silicate ceramic fibres," *J. Appl. Crystallogr.,* 30 467-75 (1997).
31. E. S. Thomas, J. G. Thompson, R. L. Withers, M. Sterns, Y. H. Xiao, and R. J. Kirkpatrick, "Further Investigation of the Stabilization of Beta-Cristobalite," *Journal of the American Ceramic Society,* 77[1] 49-56 (1994).

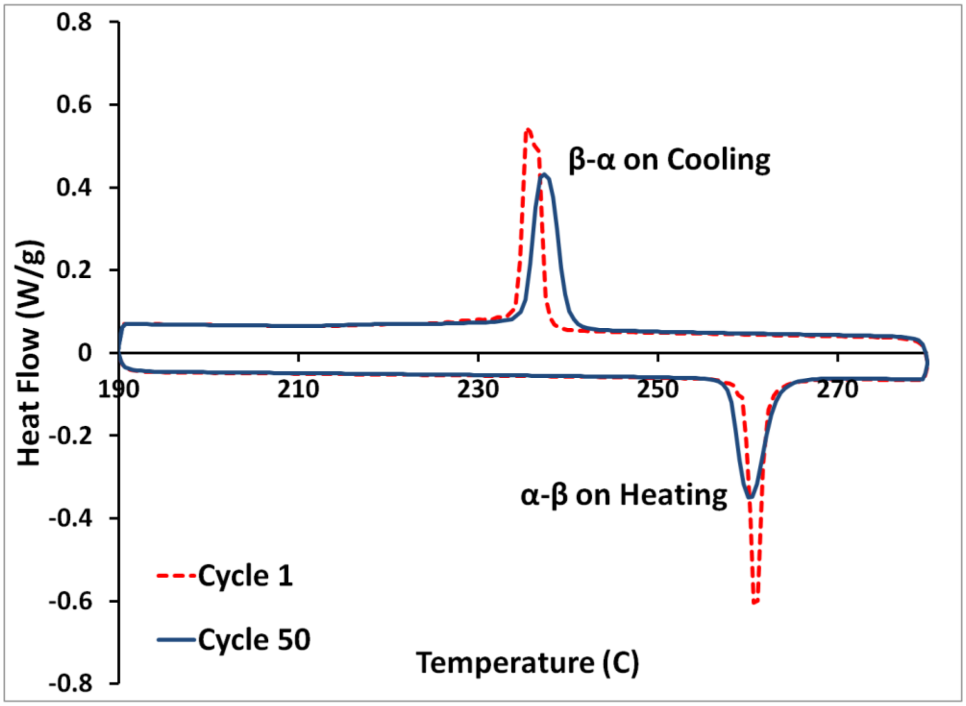

Figure 5.1 DSC curves for Cycle 1 and Cycle 50. Material was previously cooled once from β to α prior to testing.

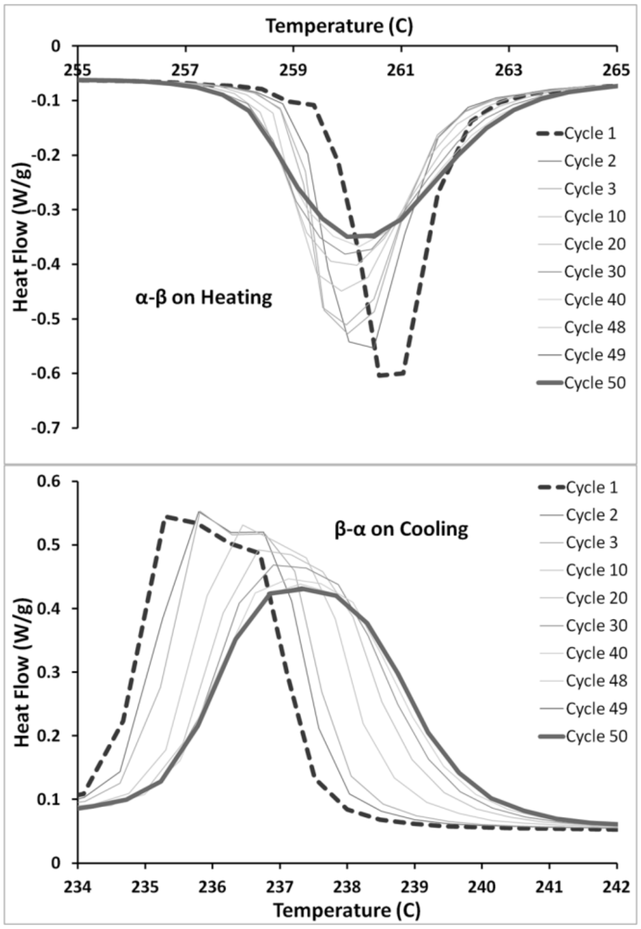

Figure 5.2 Observed exotherm from β-α transition on cooling and endotherm from α-β transition on heating through repeated cycling. The peaks are seen to shift monotonically with the onset temperature of the endotherm decreasing with each cycle and the onset temperature of the exotherm increasing with each cycle. (A) Endotherm corresponding to α-β transition (B) Exotherm corresponding to β-α transition.

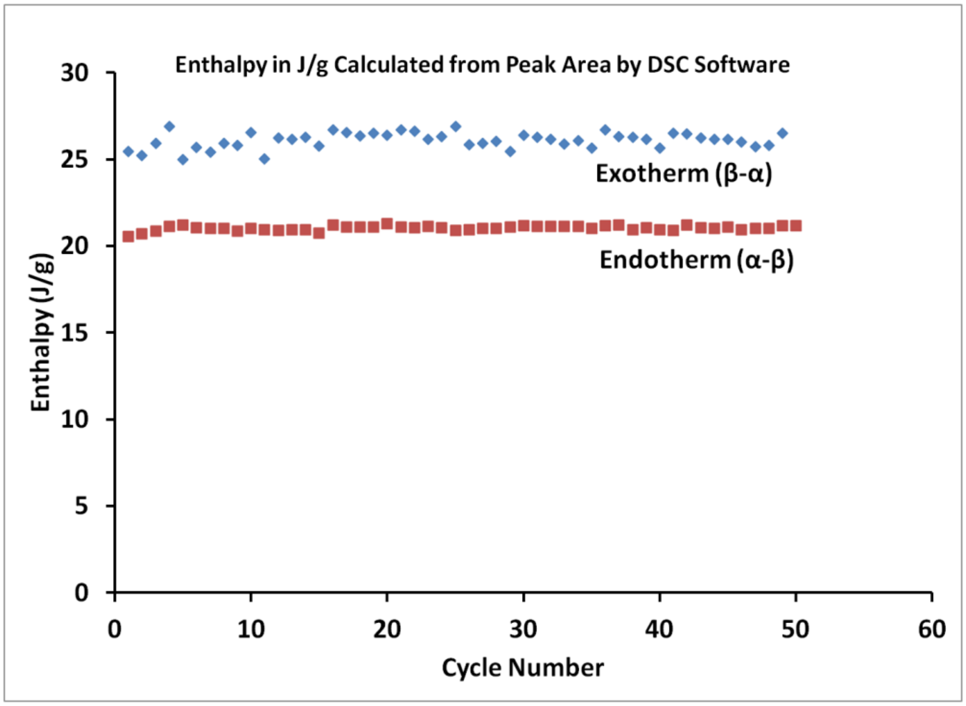

Figure 5.3 Observed energy of transformation as found by integration of peak area.

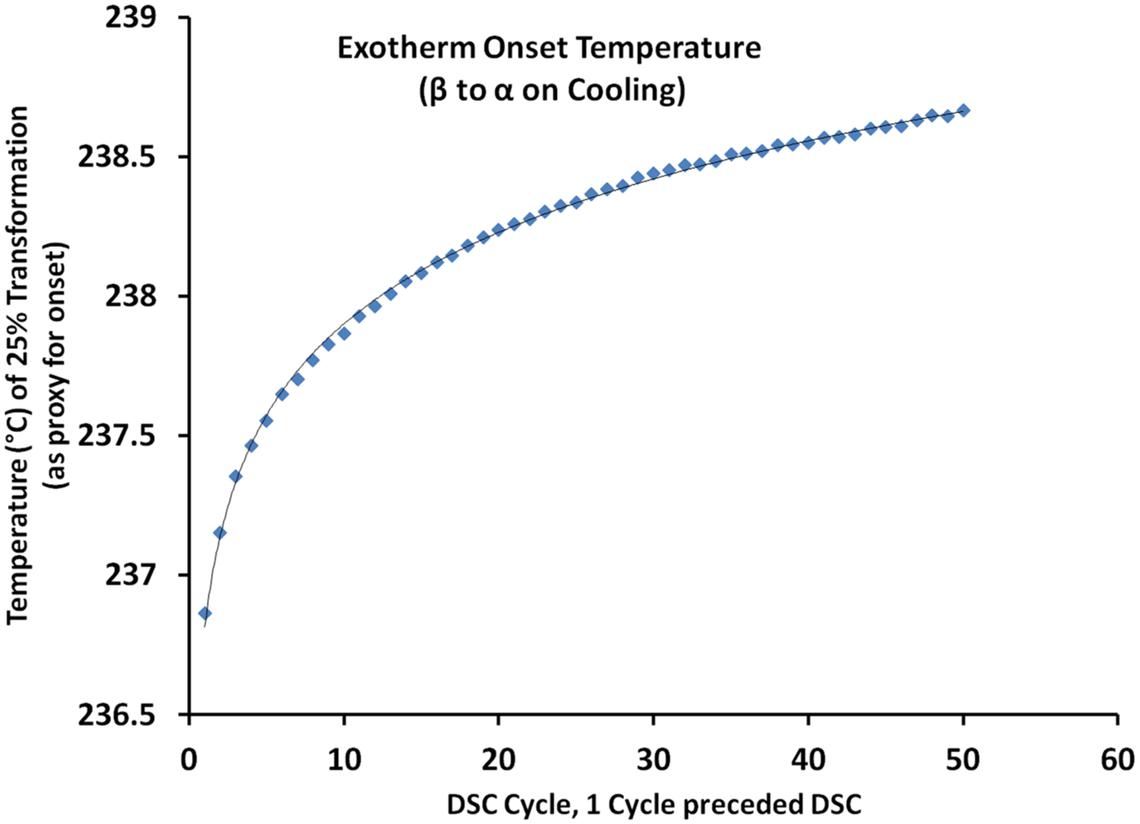

Figure 5.4 Onset temperature as a function of cycle number of the β-α exotherm.

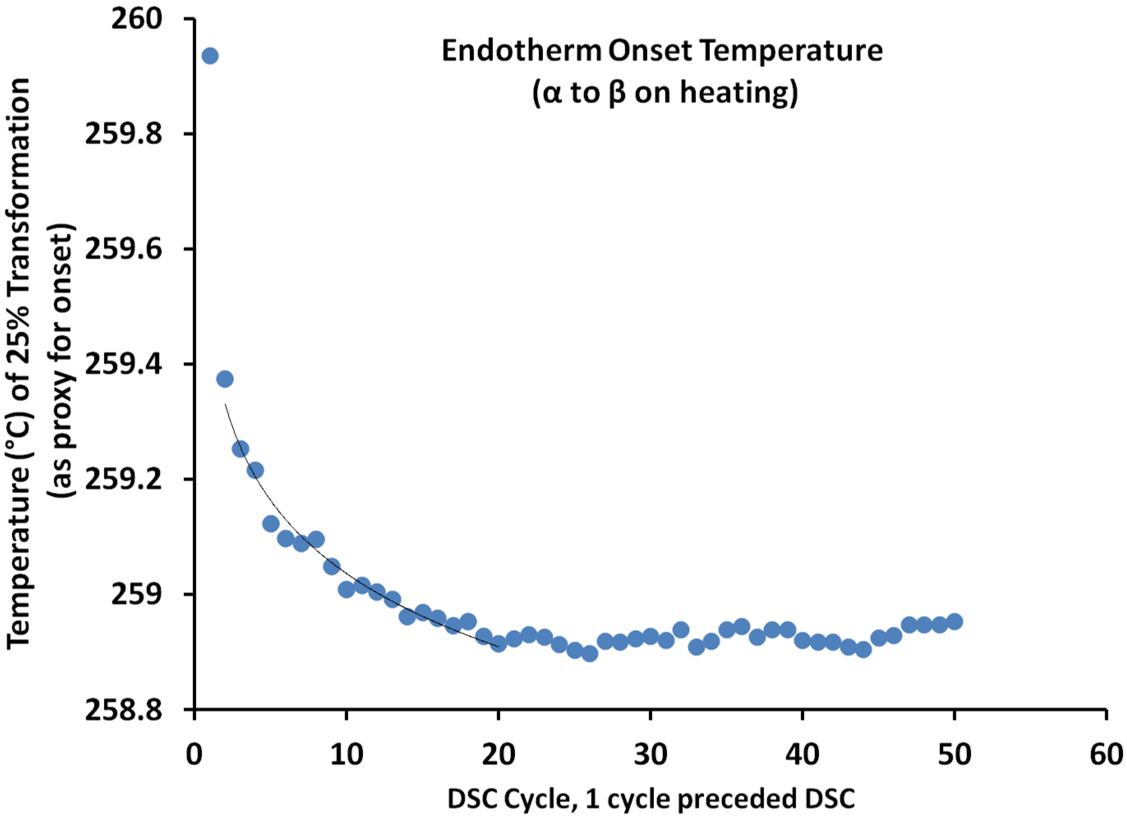

Figure 5.5 Onset temperature as a function of cycle number of the α-β endotherm.

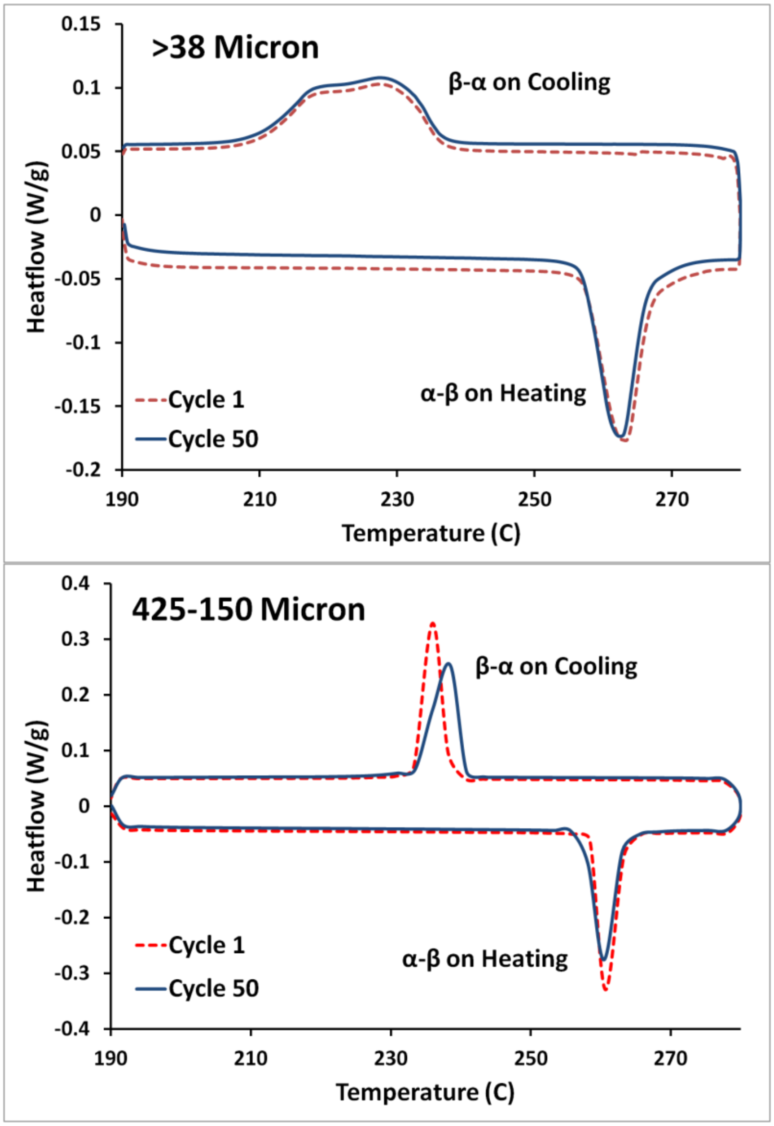

Figure 5.6 DSC curves for Cycle 1 and Cycle 50 for sieved powder fractions. (A) >38 Micron (B) 425-150 Micron.

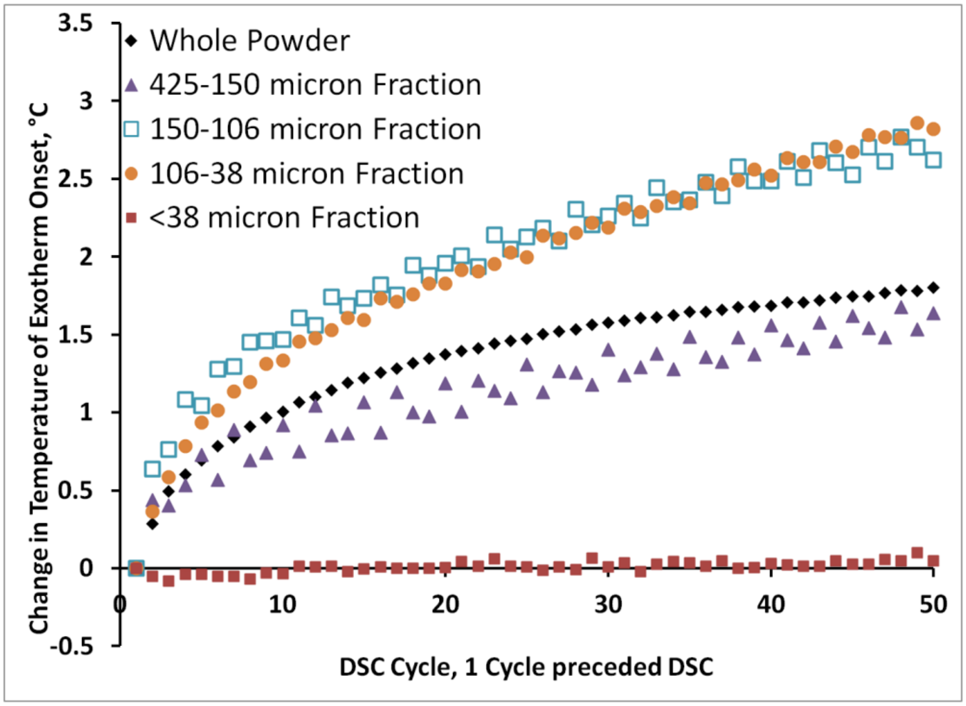

Figure 5.7 Change in exotherm onset temperature for sieved powder fractions.

Chapter 6
Stress Development and Fracture of Surface Nucleated Cristobalite on Smooth Silica Glass Surfaces

6.1 Preface

It is well established that the transformation from β-to-α cristobalite weakens sintered silica through extensive micro-fracture associated with the transformation. In order to explore the development of stress and failure due to the β-to-α transition, cristobalite crystals in a bulk matrix were used as a model system. Slides of high purity amorphous silica were annealed to induce a partial crystallization of the surface. B-cristobalite was found to form as spherulites on the surface after annealing between 1200-1400°C. At room temperature the cristobalite was observed to be heavily twinned α-cristobalite, having transformed from β-cristobalite to α-cristobalite on cooling. Stress fields were observed to surround the α-cristobalite spherulites by crossed-polarizer microscopy; presumably this stress arises from the 4.9% volume reduction associated with the β-to-α transformation. Small spherulites were observed to be twinned but otherwise intact, medium sized spherulites were observed to frequently be encircled by cracks passing through the glass matrix, and the largest spherulites were observed to have fractured through the cristobalite. The cracking behavior was modeled to clarify the role of spherulite size in the occurrence and mode of fracture.

6.2 Introduction

For over a century it has been understood that that crystallization to cristobalite weakens glass. The earliest reports of the crystallization of amorphous silica to cristobalite come from scientists frustrated by the clouding and subsequent breakage of fused-quartz lab-ware exposed to extreme temperatures, such as reported by Crookes in 1912.[1] We know this weakening effect is a result of extensive micro-fracture upon the transition of cristobalite from the high-temperature β-phase to the low-temperature α-phase at ~250°C.[2, 3, 4] This micro-fracture is caused by the 4.9% volume reduction on transition from α-β.[5]

The development of stress in glass-ceramics has been widely reported upon in the literature; however, the work tends to be directed towards bulk-nucleated glass-ceramics in which the multi-phase glass-ceramic can be used as a stiff load bearing material.[6, 7, 8, 9] Less well studied is the development of stress and failure in surface nucleating systems. This is likely because crystallization in such systems is considered a flaw rather than attribute. To our knowledge, no one has looked specifically at the stress development in the amorphous silica-cristobalite system.

Crystallization in cristobalite occurs through the formation surface spherulites which then grow and impinge to form a fully crystalline surface over an amorphous core. The lateral growth across the surface has been reported to occur faster than growth in thickness.[10] During crystallization the glass matrix is above the annealing temperature so no stress develops. On cooling small thermal mismatch stresses can develop between the β-cristobalite and amorphous silica. Although β-cristobalite has very low thermal expansion, the thermal expansion of amorphous silica is nearly zero. On cooling from the strain temperature of ~1100°C to 300°C β-cristobalite will experience a volume shrinkage of ~0.58% relative to the amorphous silica.[11] Upon cooling to ~250°C β-cristobalite transforms to α-cristobalite, resulting in a 4.9% volume reduction and the development of stress between the cristobalite and the amorphous matrix.[5] Therefore the transformation volumetric strain is ~8.4 times larger than the thermal expansion volumetric strain mismatch. As we did not observe any fracture resulting from the thermal expansion strain in β-cristobalite above 250°C, we make the approximation of only considering the much larger transformation strain. In the case of isolated spherulites, the β-cristobalite develops stress free at high temperature, but on transformation to α-cristobalite the spherulite shrinks away from the matrix as shown schematically in Figure 6.1.

In the present study the stress state of isolated spherulites and resulting fracture are observed. The fracture is modeled to understand the relationship between spherulite size and mode of fracture.

6.3 Procedure

6.3.1 Materials

A high purity bulk silica glass was used in this study. GE 124 (GE Momentive, Willoughby, OH) glass prepared as 75 mm by 25 mm by 2.5 mm slides were used as the starting material. The purity of this material is greater than 99.9%. The primary contaminants are aluminum with 14 ppm, titanium with 1.1 ppm, and hydroxyl with <5 ppm. All other contaminants amount to <4.5 ppm in total. It should be noted that this is an very low hydroxyl content that reflects the material as received material. Heating under ambient conditions will increase the hydroxyl content through absorption of atmospheric H_2O.[12, 13] This will result in higher hydroxyl content in the material at crystallization.

6.3.2 Procedure

GE 124 slides were annealed at 1200-1400°C with hold times ranging from 10 minutes to 6 hours. Annealing was conducted under ambient atmosphere with laboratory relative humidity ranging from 15-60%. During annealing the slides were held on an alumina plate and supported by alumina spacers at four points near each corner. The slide was supported in this way to minimize contact contamination that may impact crystallization.[13, 14]

Following annealing, samples were examined by optical microscopy. Polarized light was used in conjunction with a Nomarski prism in order to achieve contrast between the cristobalite and the amorphous silica matrix.

The stress fields surrounding spherulites were qualitatively examined using crossed-polarizers optical microscopy (CPLOM).

6.4 Results

Spherulites were observed to surface nucleate and grow spherulitically as has been reported by others.[3, 15, 16] Though often indistinct when spherulite symmetry can be determined it appears to be 3-fold about the center of the spherulite. This indicates the cubic β-cristobalite grew with a <111> orientation. This agrees with the results of Presser et al. who found the orientation to be <111> and growth to occur on the octahedral faces.[15] When observed at room temperatures spherulites are in the tetragonal α-cristobalte phase having transformed from cubic β-cristobalite. This α-cristobalite is highly twinned as a result of the loss of symmetry through the displacive β-α transformation and also under stress due to the 4.9% volume reduction associated with the transformation.

While many spherulites remain intact some were observed to fracture within the spherulite while others were observed with encircling cracks in the glass matrix. A typical image with fractured and unfractured spherulites in the amorphous matrix can be seen in Figure 6.3. An example of an encircling glass matrix crack and a close up of a fractured spherulite can be seen in Figure 6.4.

Amorphous silica is birefringent under stress. A spherulite surrounded by a radial stress field will polarize transmitted light to an orientation parallel to the stress. In crossed-polarizers optical microscopy (CPLOM), two polarizers oriented 90 degrees apart are utilized, one above and one below the sample. If the sample does not induce any polarization, the light that passes the first polarizer will be extinguished upon reaching the second due to the misorientaion of 90 degrees. In the case of a radial tensile field the light passing through the sample will reorient to be parallel to the stress field. The reoriented light passes through the second polarizer resulting in an illumination effect. In our case of a radial stress field the light will also be polarized. This radial polarization effect in the stressed amorphous silica results in an illumination effect with intensity that scales with the degree of misorientation relative to the polarizers. In the case of a radial stress field (such as that surrounding an α-spherulite) the observed intensity are at a maxima at 45° misorientation to the polarizers. This results in a "Maltese Cross" pattern centered on the middle of the radial stress field. Conversely the misorientation and intensity are at a minimum when aligned with one polarizer or the other. The end results for polarizers oriented vertically and horizontally are intensity maxima at 45, 135, 225, and 315 degrees and minima at 0, 90, 180, and 270 degrees. The development of the Maltese cross under crossed-polarizer microscopy is presented schematically in Figure 6.2.

The stress fields surrounding the α-cristobalite spherulites were imaged qualitatively by CPLOM, as seen in Figure 6.4. (It is feasible to apply a quantitative technique in which the reorientation provides an integrated stress through the thickness. However, such a technique requires specialized equipment and careful consideration. It was decided that the information acquired would not be worth the investment in time.) An image with 3 neighboring spherulites imaged both by reflected polarized light and by cross-polarized light can be seen in Figure 6.6. As discussed in Section 6.3.2, the intensity of a radially symmetric field has maxima at 45, 135, 225, and 315 degrees and minima at 0, 90, 180, and 270. In Figure 6.6 the spherulites are oriented diagonally relative to the polarizers to maximize the intensity in between them. The stress concentration can be seen to be very intense in between the spherulites. In Figure 6.7 an S-crack can be seen, likely initiating from the stress concentration between two adjacent spherulites.

At room temperature spherulites were found to exist in one of three states: (1) Intact, with intact spherulites surrounded by intact but stressed glass matrix; (2) Matrix Cracked, with intact spherulites surrounded by an encircling crack passing through the glass matrix; (3) Self-Fracture, with “mud-crack” self-fracture of the cristobalite spherulite itself. These three states were found to coexist in the same sample. This can be seen in Figure 6.8, in which examples of the 3 states can be seen in reflected polarized and transmitted cross-polarized imaging. A survey was conducted on the failure mode for isolated spherulites to look at the incidence of intact spherulites, matrix cracking, and spherulite self-fracture as a function of spherulite size. In total 2731 spherulites were observed from 7 separate annealed samples. The results are tabulated as a cumulative plot as a function of size in Figure 6.9. For spherulites 30 microns and larger, the spherulite size was recorded with an accuracy of ±5 microns. For spherulites smaller than 30 microns, the accuracy is ±2 microns. It can be seen that no fracture of the cristobalite or encircling cracks in the matrix occur for spherulites less than 15 microns in diameter. For intermediate sizes, some spherulites have matrix cracked with an encircling crack through the glass matrix. Spherulites 70 microns and greater in diameter are almost all self-fractured through the cristobalite in a “dry mud” manner. The occurrence of both matrix cracks in the glass and spherulite self-fracture of the cristobalite appear to be size dependent. However, matrix cracking was always a minority of the spherulites in a given sample; whereas above 70 microns almost all spherulites were observed to be self-fractured. This suggests that while both behaviors are size dependent they may depend on size in a different manner.

6.5 Discussion

6.5.1 Observed failure modes

As seen in Figure 6.8, following the β-α transition, isolated spherulites were observed in one of three states: intact, matrix cracked, or self-fractured. Intact here refers to intact spherulites in intact matrix, while matrix cracked refers to intact spherulites encircled by a crack through the matrix. Self-fractured refers to spherulites in which th cristobalite has fractured. No spherulites were observed to have matrix cracks and also be self-fractured. These two different failure modes both appear to relieve stress, but also appear to be separate phenomena. Both failure modes seem to be size dependent with the population occurring at different spherulite diameters as seen in Figure 6.9. Small spherulites with diameters 15 microns and smaller are all intact, with no cracks in the matrix or fracture of the spherulite. Spherulites between 15 and 70 microns in diameter sometimes are encircled by a crack through the matrix, with frequency of matrix cracking increasing with spherulite diameter. Spherulites above 70 microns in diameter self-fracture through the cristobalite, with very few exceptions. In the following sections the matrix cracking and spherulite self-fracture are modeled.

6.5.2 Modeling matrix cracking

Many spherulites have encircling cracks through the matrix. Such cracks could be caused by the tensile field surrounding the spherulite initiating cracking in the glass. The encircling cracks can occur some distance from the edge of the spherulite. This may be due to the cracks initiating from flaws in the glass, as often observed for the fracture of glass. This would imply an interaction between the stress field intensity and the flaw distribution of the amorphous silica leads to the observed spacing between the spherulite and the encircling crack.

The spherulite can be considered a hemispherical inclusion on the surface of the glass. The well known Eshelby model for a spherical inclusion can then be used to approximate the stress state in the surrounding matrix. In the classic Eshelby solution a spherical particle becomes strained relative to the matrix due to a thermal expansion mismatch. This strain leads to the development of a hydrostatic internal pressure and stress in the surrounding matrix. In the case of the spherulite in the matrix a transformation strain causes the inclusion (spherulite) to shrink relative to the matrix. This is analogous to the Eshelby treatment of stress development on cooling for an inclusion with a greater thermal expansion than the matrix. From the Eshelby solution in this case, the stress inside the inclusion is uniform tension, which is expressed as a pressure p, where:

$$p = \frac{2E\left(\alpha_m - \alpha_p\right)(T_r - T_h)}{(3 - 3\upsilon)} = \sigma_r^{(p)} = -\sigma_\theta^{(p)} = -\sigma_\phi^{(p)} \qquad Eq. 6.1a$$

The three stresses on the right hand side are the radial, angular, and azimuthal stress components in spherical coordinates. These stress components are all equal since inside the particle there is hydrostatic tension. Notice that the stress inside the particle is *independent of size* of the inclusion in this model.

For the case of the β-to-α phase transformation of cristobalite spherulites in a glass matrix the thermal expansion mismatch strain for the Eshelby form is relplaced by the transformation strain, ε_{trans} for the case of β-cristobalite transforming to α-cristobalite.

$$p = \frac{2E\varepsilon_{trans}}{(3 - 3\upsilon)} = \sigma_r^{(p)} = -\sigma_\theta^{(p)} = -\sigma_\phi^{(p)} \qquad Eq. 6.1b$$

Similarly the matrix stresses can be modeled. The stress in the glass matrix surrounding the spherulite has radial *tension*, and angular and azimuthal *compression*. Radial tension in the surrounding glass matrix damps with distance as $1/r^3$ and increases with the cube of the particle size a^3:

$$\sigma_r^{(m)} = \frac{2E\varepsilon_{trans}}{(3 - 3\upsilon)} \frac{a^3}{r^3} = p\frac{a^3}{r^3} \qquad Eq. 6.2$$

This radial tension has the potential to cause the glass matrix to crack. The plane of the crack will be any concentric shell in the glass matrix around the spherulite. There also are compressive stresses in the angular and azimuthal directions. These are:

$$\sigma_\theta^{(m)} = \sigma_\phi^{(m)} = \frac{-2E\varepsilon_{trans}}{(3 - 3\upsilon)} \frac{a^3}{r^3} = -p\frac{a^3}{r^3} \qquad Eq. 6.3$$

These compressive forces are constant with the angles θ,ϕ and damp out in magnitude with the square of the radial distance from the spherulite. They will not cause fracture, but they will suppress any angular or azimuthal component to the crack path. Therefore a matrix crack will tend to circle around the spherulite. This model could explain why cracks initiated some distance from the spherulite encircle but do not approach the spherulite.

The highest magnitude of the matrix tension occurs at r=a, the boundary between the spherulite and the matrix. However, for an incremental spherical shell outside the spherulite, while the stress decreases as $1/r^3$, the volume under stress increases as $4\pi/3(r^3-a^3)$. So in the region where the stress is highest, the stressed volume is smallest. Fracture in glass is often determined by the largest flaw found in the stressed volume, so the problem can be considered in the context of Weibull statistics.

The probability, F, of initiating an encircling matrix crack can be described as:

$$F = 1 - exp\left[\int_a^\infty -\left(\frac{\sigma(r)}{\sigma_o}\right)^m \frac{V(r)}{V_o} dr\right] \qquad Eq. 6.4$$

where σ_o and m are the characteristic strength and Weibull modulus for a two-parameter Weibull, and V_o is the reference volume associated with the characteristic strength. Since the stress and stressed volume change with distance r, we assess the failure probability integrated for all r greater than the spherulite radius a. Equation 6.4 models how the probability of failure varies with stressed volume V(r). Substituting values for the stress and volume terms allows the integration as follows:

$$F = 1 - exp\left[\int_a^\infty -\left(\frac{pa^3}{\sigma_o r^3}\right)^m \frac{2\pi r^2}{V_o} dr\right] \qquad Eq. 6.5a$$

Followed by:

$$F = 1 - exp\left[\frac{2\pi}{V_o}\left(\frac{pa^3}{\sigma_o}\right)^m \int_a^\infty r^{2-3m} dr\right] \qquad Eq. 6.5b$$

And finally:

$$F = 1 - exp\left[\frac{2\pi}{V_o}\left(\frac{p}{\sigma_o}\right)^m \frac{a^3}{3m-3}\right] \qquad Eq. 6.5c$$

So from Eq. 6.5c, the probability of crack initiation in the matrix surrounding a single spherulite is simply a function of the Weibull parameters, the internal pressure p derived from the Eshebly approximation, and the spherulite size, a. If we consider the size when the probability of matrix cracking is a particular value, say 37% (i.e., 1/e) to simplify the exponential, we have a critical spherulite size is $a_{F=0.37}$ where:

$$\underset{F=0.37}{a} = \left(\frac{[3m-3]V_o}{2\pi}\right)^{1/3} \left(\frac{\sigma_o}{p}\right)^{m/3} \qquad Eq. 6.6$$

Thus the likelihood of matrix cracking should increase strongly with the spherulite size, but remains a statistical phenomenon. This seems to match the behavior seen in Figure 6.9. Glass matrix cracking caused by spherulites is clearly related to size with larger sizes being associated with higher rates of matrix cracking; however, matrix cracking is always observed to coexist with unfractured spherulites. The Weibull model suggests that as spherulites get larger the probability of activating a flaw and triggering a matrix crack increases, but it remains a statistical phenomena dependent on the Weibull parameters of the glass. Thus the observed matrix cracks behave in the manner of a classic brittle failure induced by a stress field than can be approximated by Eshelby methods.

6.5.3 Modeling spherulite self-fracture of α-cristobalite

The self-fractured spherulites can be considered separately from glass matrix cracking, because the fracture occurs within the cristobalite and the crack morphology differs. The geometry of the spherulites may also change as they grow as others have reported faster growth laterally than in depth;[10] however we were unable to accurately measure depth of the spherulites and so cannot confirm this. Self-fractured spherulites exhibit a cracking pattern reminiscent of dried mud. This pattern of cracking is not uncommon in thin film applications. In many thin film applications a stress develops between the film and the substrate, such as that due to a mismatch in thermal expansion. Often such films develop channel cracks to alleviate this stress, resulting in dried-mud morphology. This may suggest the largest spherulites are behaving similar to thin films under stress. In fact, as can be seen in Figure 6.10 when the spherulites impinge and create a fully crystalline surface the fracture pattern remains similar to that of self-fractured spherulites. This supports the hypothesis that self-fractured spherulites are behaving like thin films. A cristobalite layer on an amorphous silica matrix will attempt to shrink on passing the β-α transition, but it will be constrained by the underlying matrix. The constraint from the underlying glass results in biaxial stresses. This situation is directly analogous to a thin film on a thick substrate experiencing biaxial tension.

A thin film under biaxial stress on an infinite matrix is a well defined system. In such systems the stress often arises from a strain resulting from the thermal expansion mismatch between the film and substrate. In the case of the spherulites the strain is the strain from the β-α transition. Cristobalite and amorphous silica both have an elastic modulus of 72 GPa which further simplifies the relationship. The fracture of thin films on infinite substrates with identical elastic moduli is governed by:

$$\frac{\left({}^{E}\!/_{(1-v^2)}\right)G_{ss}}{\sigma_o^2 h} = 1.98 \qquad Eq. 12$$

in which G_{ss} is the steady state energy release due to fracture.[17] Fracture is expected if $G_{ss} \geq \Gamma$, where Γ is the cohesive energy of the material. This provides a critical thickness, h_c, for failure given transformation strain, ε_{trans} as follows:

$$\frac{\Gamma}{\left({}^{E}\!/_{(1-v^2)}\right)\varepsilon_{trans}^2 1.98} = h_c \qquad Eq. 6.13$$

For a given strain energy, elastic modulus, poissons ratio, and cohesive energy there is a critical film thickness at which the film cracks spontaneously. One can suppose that for spherulites the thickness, h, is a function of the diameter, a. If we make an approximation that a = b*h we can rewrite Eq. 43 in terms of spherulite diameter:

$$\frac{b\Gamma}{\left({}^{E}\!/_{(1-v^2)}\right)\varepsilon_{trans}^2 1.98} = a_c \qquad Eq. 6.14$$

This suggests that above a critical diameter the spherulite is expected to be able to lower its energy by spontaneously fracturing. This matches the behavior seen for spherulite fracture. Above a certain size the spherulites are observed to nearly universally self-fracture. A field of spherulites above this critical size can be seen in Figure 6.11. The critical value for spherulite diameter, a_c, appears to be ~70 microns as very few spherulites are unfractured above that size. It seems that self-fractured spherulites are exhibiting fracture behavior similar to thin films. Upon reaching a certain size the strain energy associated with the biaxial constraint of the transformation strain induces fracture of the spherulite.

6.6 Conclusions

Cristobalite spherulites were formed on the surface of fully dense amorphous silica and allowed to pass the β-α transition upon cooling. Stress fields were observed to surround unfractured samples by crossed-polar microscopy. Fractured spherulites were found to have failed by one of two mechanisms, either by encircling cracks passing through the matrix or "mud-cracking" of the spherulite itself. Matrix cracks were observed to always co-exist with unfractured spherulites, and the frequency of cracking was observed to increase with spherulite size. Spherulite fracture on the other hand, was observed in larger spherulites, and nearly all spherulites above 70 microns in diameter were self-fractured. Applying a Weibull statistics to glass cracks induced by an Eshelby stress field produced a model for matrix cracking. This model predicts probabilistic matrix hoop cracking with a dependence on spherulite size, which aligns with observation. The occurrence of matrix cracks is a size dependent but statistical phenomena. A separate model based on thin-film mechanics was formulated for spherulite fracture. The spherulite behaves as a thin film under biaxial stress over an infinite matrix. This model predicts a critical size at which the spherulite will fracture. This critical size matches the observation that above a certain size, nearly all spherulites have self fractured. Based on the models and observations, a complete picture of failure can be developed. Upon transitioning from β-α stress is induced by the ~5% volume reduction. In spherulites above a critical size this results in spontaneous self fracture. In spherulites below the critical size, the stress field may induce cracking if the stress field activates a sufficiently large flaw. Larger spherulites induce larger matrix stresses over larger areas increasing their probability of activating a flaw, but matrix cracking remains a statistical phenomena.

6.7 References

1. W. Crookes, "On the devitrification of silica glass," *Proc. R. soc. Lond. Ser. A-Contain. Pap. Math. Phys. Character,* 86[588] 406-08 (1912).
2. R. B. Sosman, "The Phases of Silica.*"* Rutgers University Press, (1965).
3. N. G. Ainslie, C. R. Morelock, and D. Turnbull, "Devitrification Kinetics of Fused Silica,*"* in Symposium on Nucleation and Crystallization in Glasses and Melts.
4. F. E. Wagstaff, "Crystallization Kinetics of Internally Nucleated Vitreous Silica," *Journal of the American Ceramic Society,* 51[8] 449-& (1968).
5. D. R. Peacor, "High-temperature Single Crystal Study of Cristobalite Inversion," *Z. Kristall.,* 138 274-98 (1973).
6. V. R. Mastelaro and E. D. Zanotto, "Residual stresses in a soda-lime-silica glass-ceramic," *J. Non-Cryst. Solids,* 194[3] 297-304 (1996).
7. O. Peitl, F. C. Serbena, V. R. Mastelaro, and E. D. Zanotto, "Internal Residual Stress Measurements in a Bioactive Glass-Ceramic Using Vickers Indentation," *Journal of the American Ceramic Society,* 93[8] 2359-68 (2010).
8. F. C. Serbena and E. D. Zanotto, "Internal residual stresses in glass-ceramics: A review," *J. Non-Cryst. Solids,* 358[6-7] 975-84 (2012).
9. E. D. Zanotto, "Glass Crystallization Research A 36-Year Retrospective. Part I, Fundamental Studies," *Int. J. Appl. Glass Sci.,* 4[2] 105-16 (2013).
10. R. S. Hay, G. E. Fair, R. Bouffioux, E. Urban, J. Morrow, A. Hart, and M. Wilson, "Relationships between Fiber Strength, Passive Oxidation, and Scale Crystalization Kinetics in HI-Nicalon-S SiC Fibers," pp. 39-51. in Mechanical Properties and Performance of Engineering Ceramics and Composites Vi, Vol. 32**.** *Ceramic Engineering and Science Proceedings.* Edited by D. Singh, J. Salem, and S. Widjaja, 2011.
11. I. P. Swainson and M. T. Dove, "On the Thermal Expansion of Beta-Cristobalite," *Physics and Chemistry of Minerals,* 22[1] 61-65 (1995).
12. T. Honma, N. Tamura, K. Saito, and E. Sekiya, "Difference in Structural Relaxation Times of Inner Surface and Inner Bulk Region of Silica Glass Arc Tube," *New Journal of Glass and Ceramics* 48-52 (2013).
13. P. P. Bihuniak, "Effect of Trace Impurities on Devitrification of Vitreous Silica," *Journal of the American Ceramic Society,* 66[10] C188-C89 (1983).
14. E. Opila, "Influence of Alumina Reaction Tube Impurities on the Oxidation of Chemically-Vapor-Deposited Silicon-Carbide," *Journal of the American Ceramic Society,* 78[4] 1107-10 (1995).
15. V. Presser, A. Loges, Y. Hemberger, and K. G. Nickel, "Microstructural Evolution of Silica on Single-Crystal Silicon Carbide. Part I: Devitrification and Oxidation Rates," *Journal of the American Ceramic Society,* 92[3] 724-31 (2009).
16. F. E. Wagstaff and K. J. Richards, "Preparation and Crystallization Behavior of Oxygen Deficient Vitreous Silica," *Journal of the American Ceramic Society,* 48[7] 382-& (1965).
17. M. S. Hu, M. D. Thouless, and A. G. Evans, "The Decohesion of Thin-films from Brittle Substrates," *Acta Metallurgica,* 36[5] 1301-07 (1988).

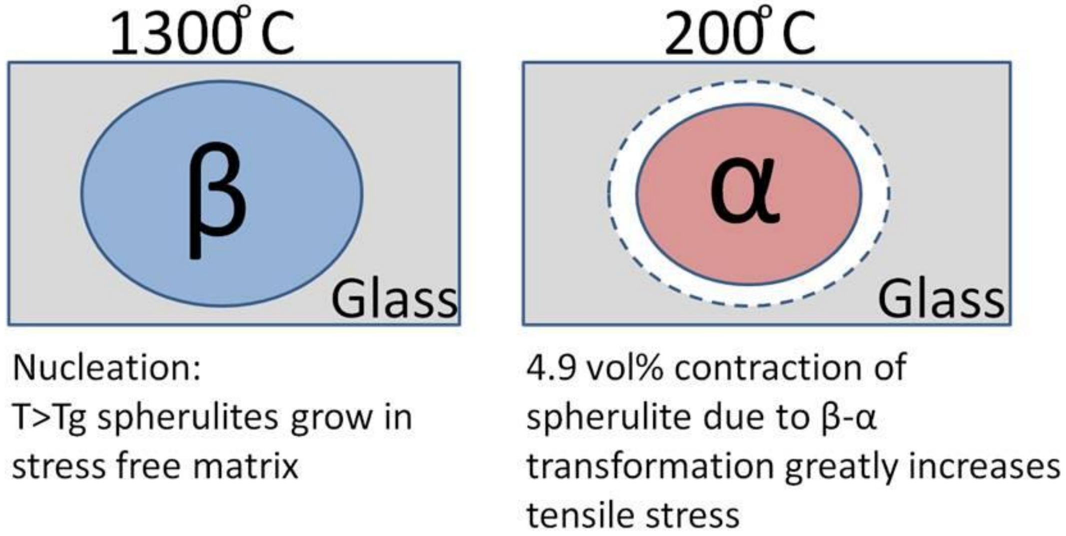

Figure 6.1 Illustration of the β-α transformation for an isolated spherulite in a glass matrix. The 4.9% volume decrease on transformation to α from β on cooling causes the spherulite to try to pull away from matrix inducing stress and/or failure.

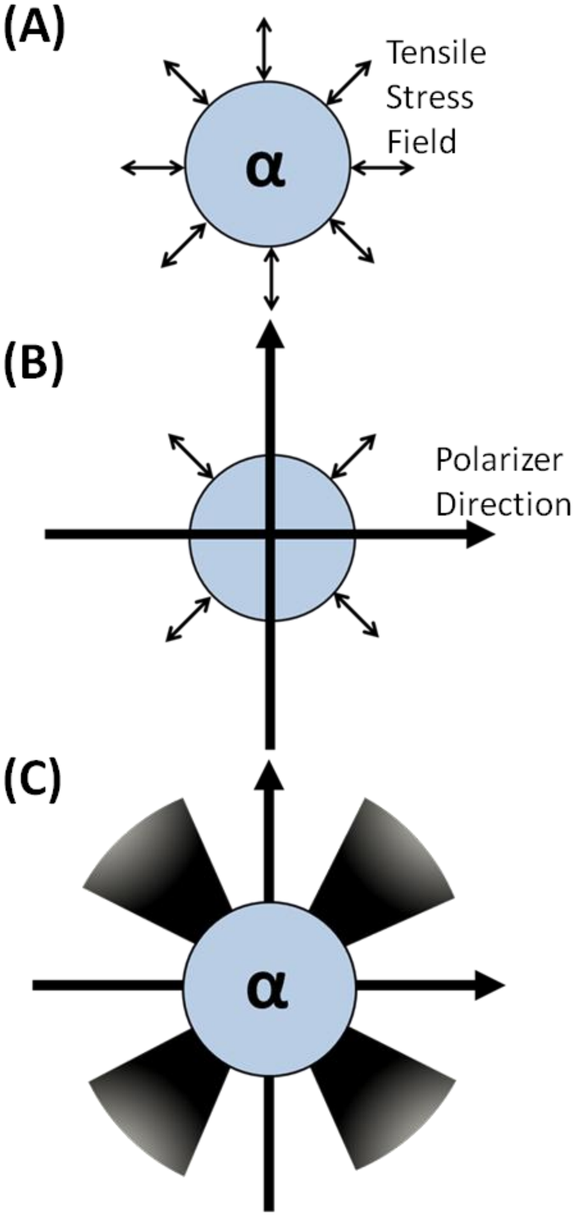

Figure 6.2 Schematic for origin of Maltese cross pattern under crossed polarizers. (A) A radial tensilie field surrounds the spherulite. (B) Crossed polarizers oriented vertically and horizontally are over laid. At 0, 90, 180 and 270 degrees around the spherulite the stress field is parallel or anti-parallel to a polarizer. (C) View seen in microscope with crossed polarizers. Light intensity scales with misorientation to both polarizers. This leads to maxima at 45, 135, 225, and 315 degrees.

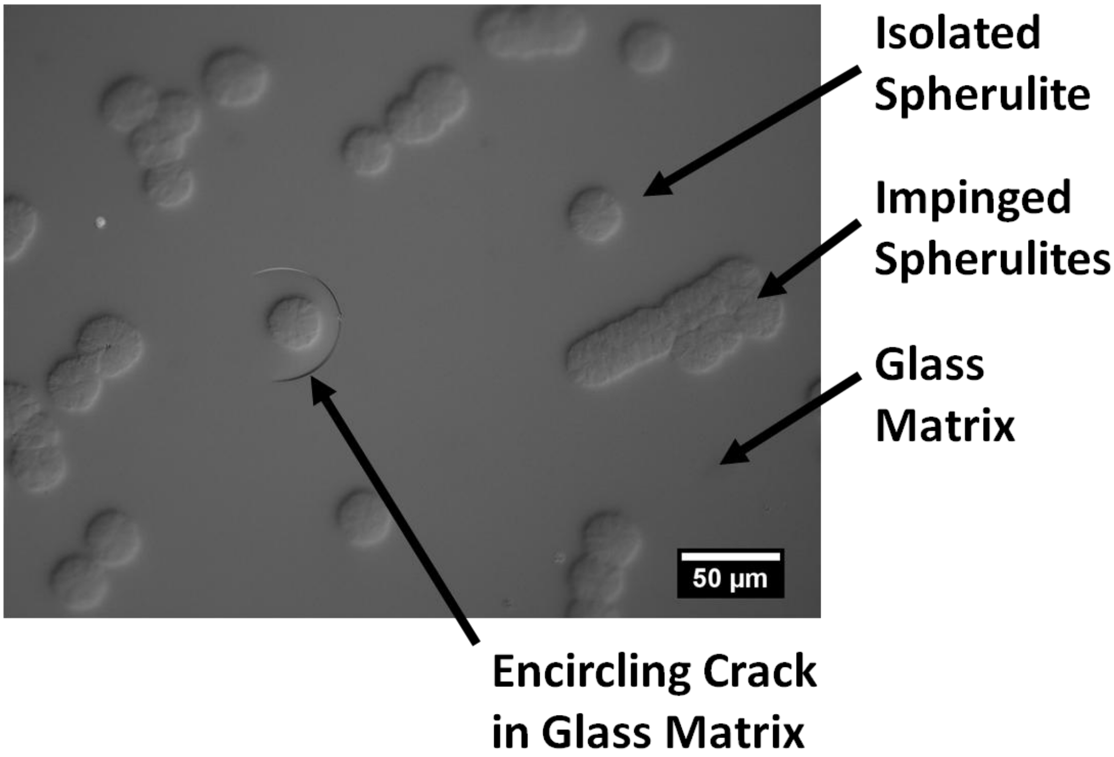

Figure 6.3 Isolated spherulites in amorphous silica matrix viewed by reflected polarized light. Spherulites can be observed in both fractured and unfractured state.

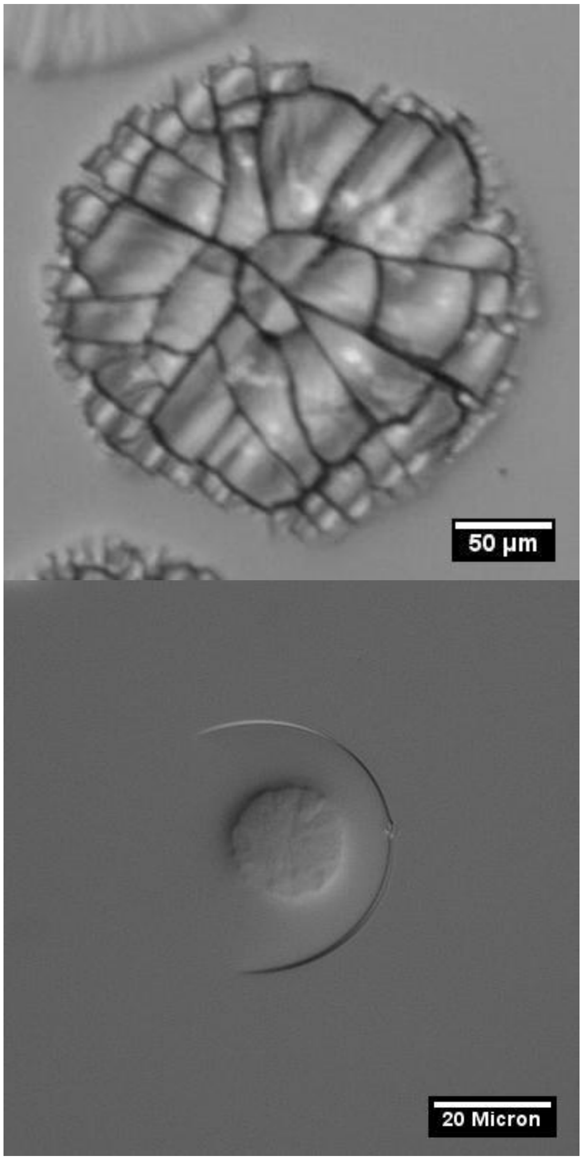

Figure 6.4 Close up images of fractured spherulite and spherulite with a surrounding matrix crack viewed by reflected polarized light.

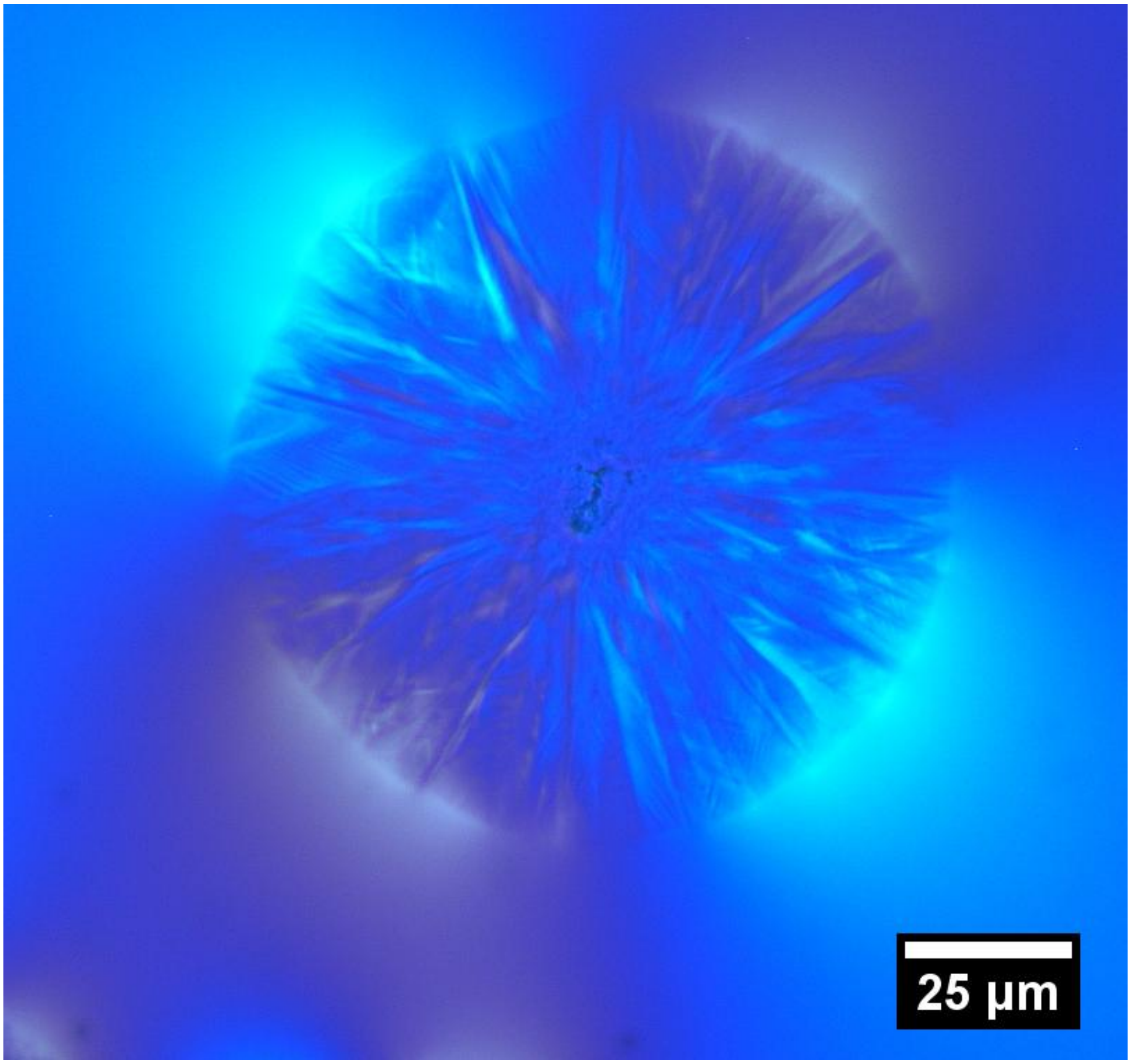

Figure 6.5 Close up of isolated spherulite imaged under transmitted crossed-polars microscopy. Stress fields present a "Maltese cross" shape due to the interaction between the crossed polars and the radial symmetric stress field. The "feathered" appearance within the spherulite is due to twinning.

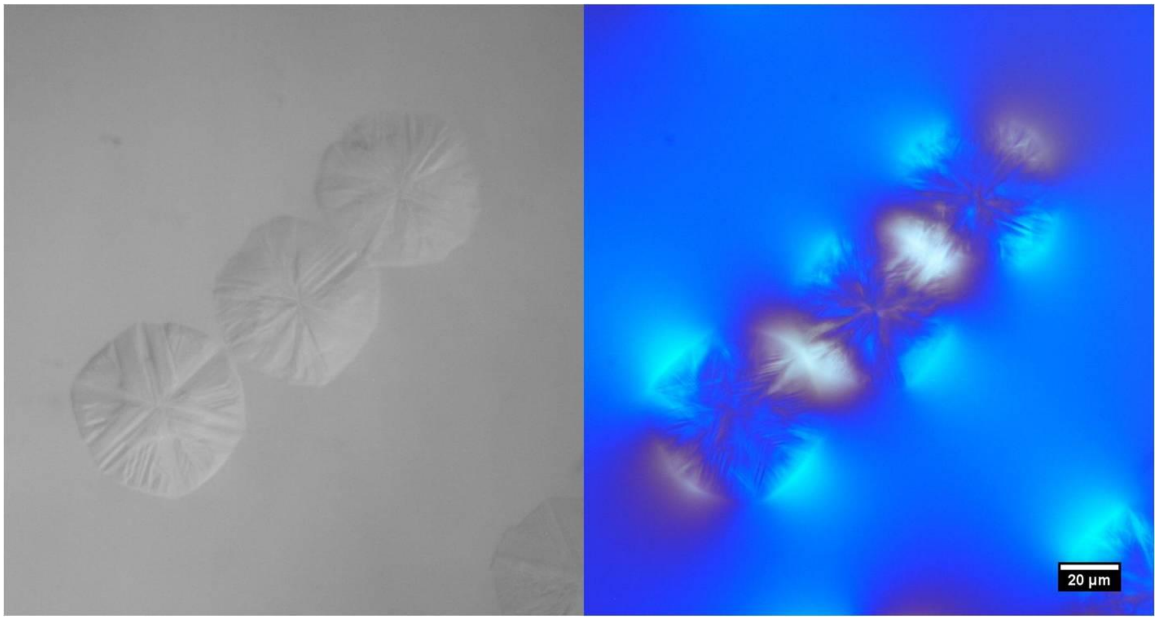

Figure 6.6 **Spherulites imaged under polarized reflected light [left] and imaged by cross-polarized transmitted light [right]. Cross-polarized imaging highlights the stress concentration between spherulites.**

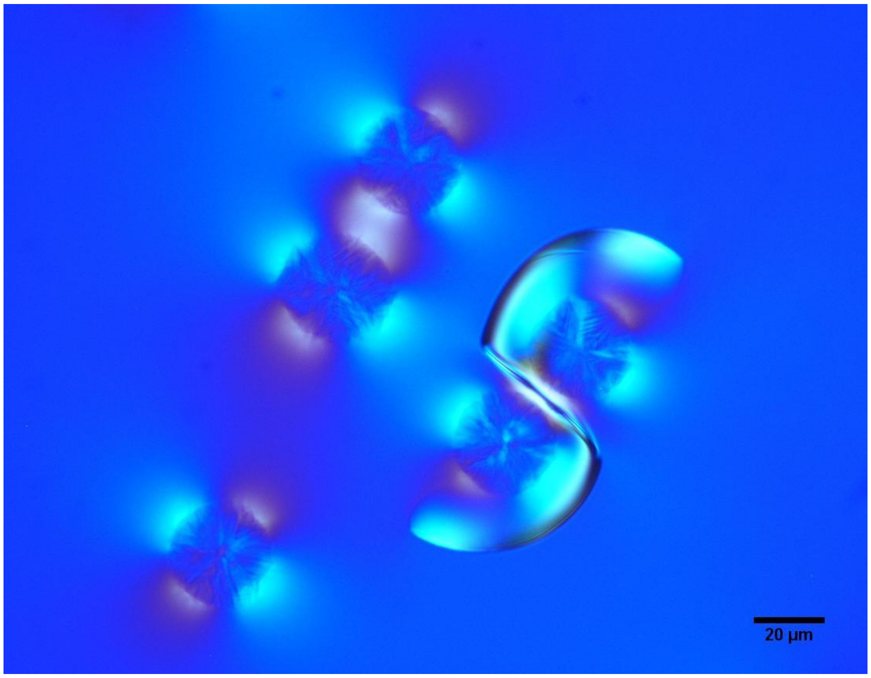

Figure 6.7 Transmitted cross-polarized light image illustrating stress fields and matrix cracking.

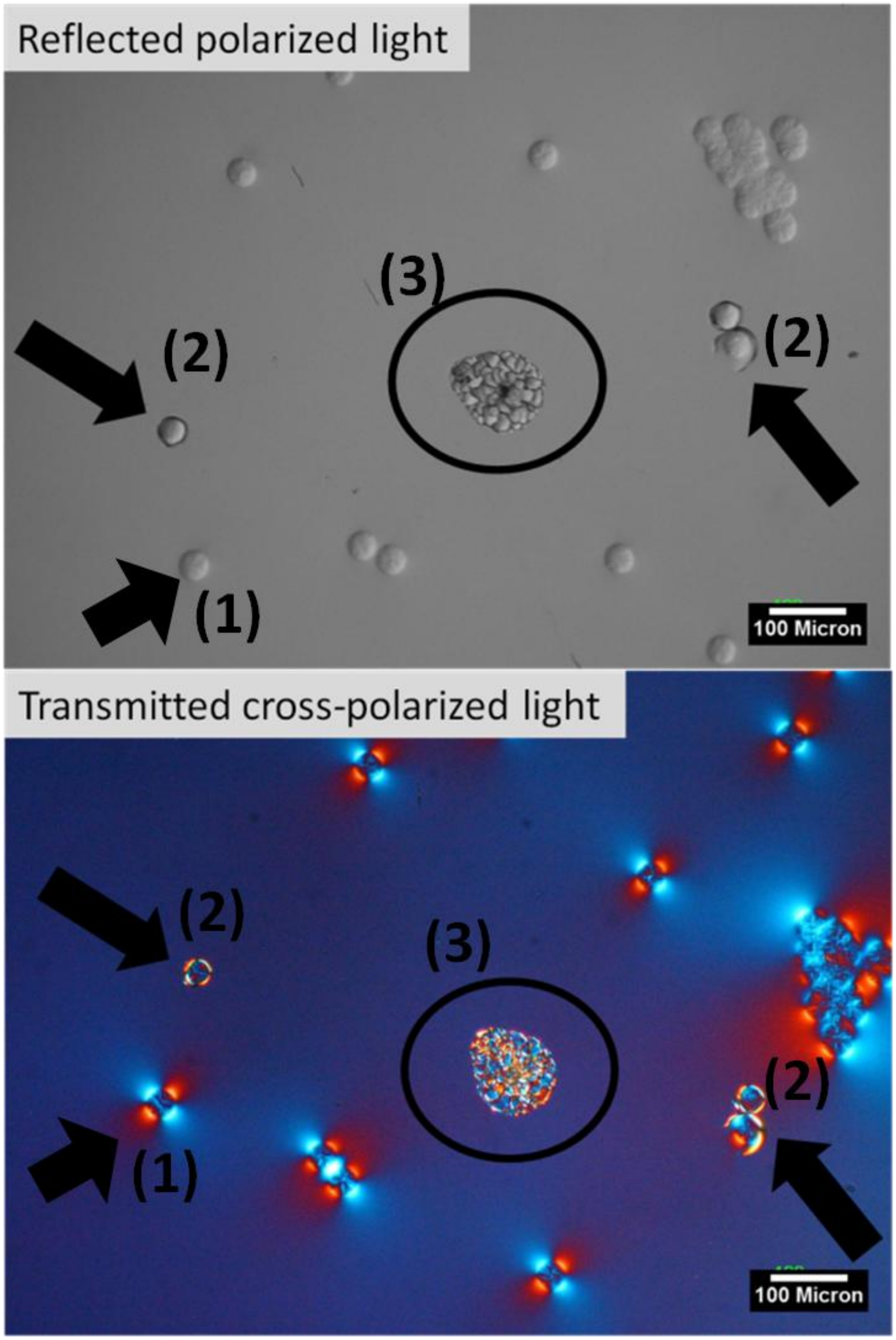

Figure 6.8 Reflected polarized and crossed-polarized light images showing 3 behaviors of spherultes: (1) Stressed by no fracture (2) Matrix cracking around spherulite (3) Fracture of the spherulite.

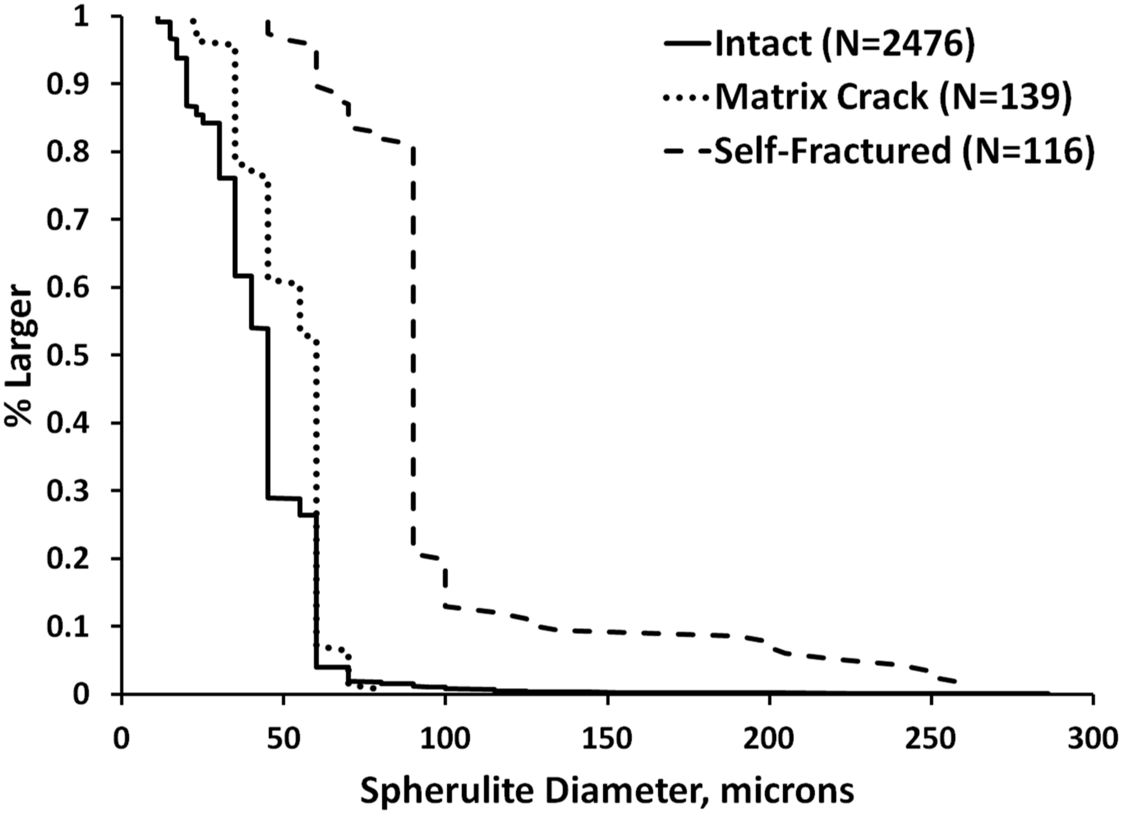

Figure 6.9 Cumulative distribution by size of isolated spherulites for each failure behavior.

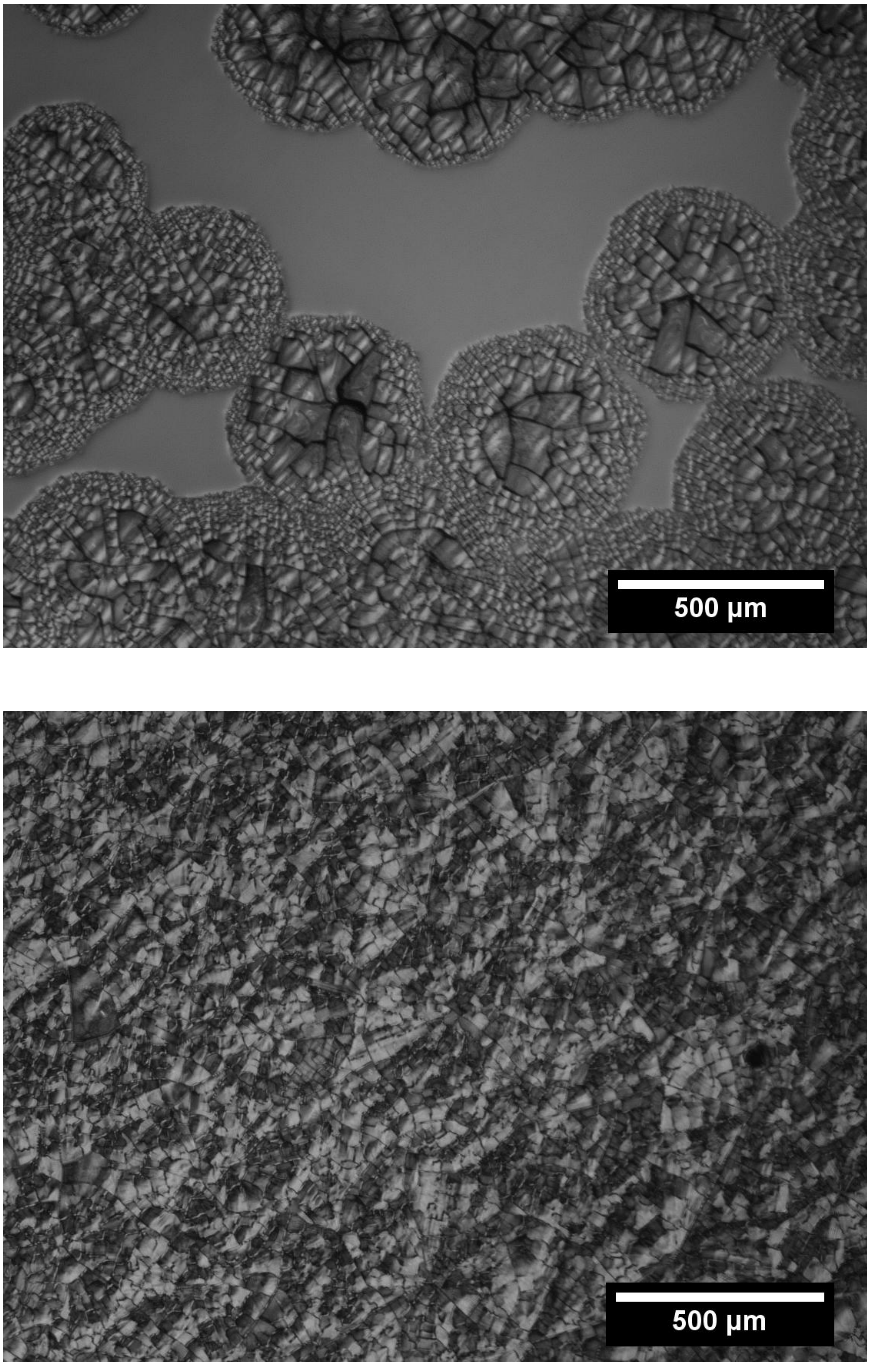

Figure 6.10 Fractured surface of sample in which spherulites have begun impinging (top) and in which spherulites have all impinged (bottom) producing fully crystalline surface over an amorphous bulk.

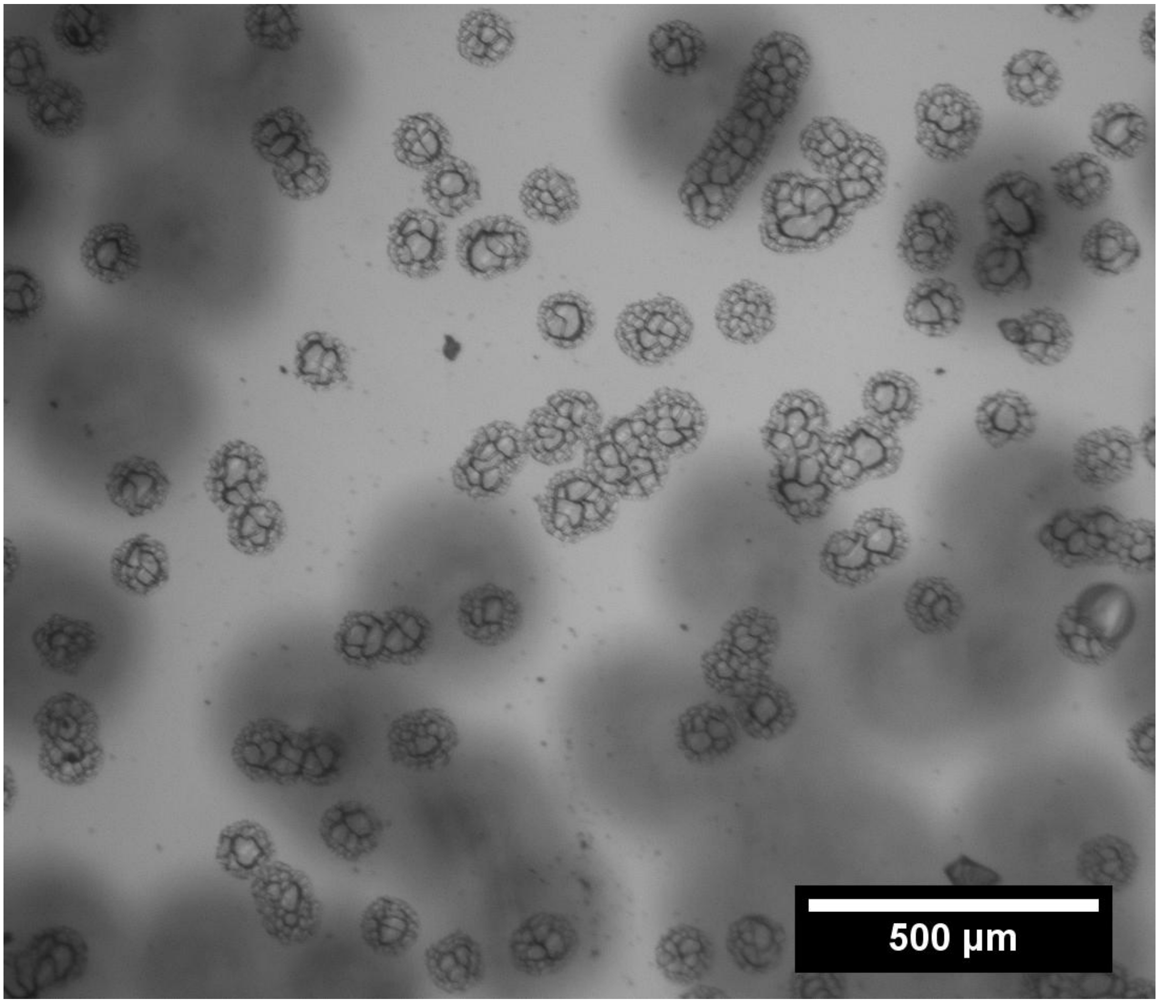

Figure 6.11 A field of view with many spherulites of ~90 microns in diameter, all of which have self-fractured. The blurry dark background shapes are crystallization on the far surface.

Chapter 7
Addressing Development of Separation Flaws in LAMP Builds Through Control of Photo-Curing Process

7.1 Preface

Following the successful casting of single crystal super-alloy in an un-cored LAMP mold, the focus was placed on addressing a particular type of problem that occurred in the LAMP molds. These were crack-like flaws between the build layers, which were referred to in the project as "cracks" or "delaminations." But, as the term "crack" implies failure due to a mechanical stress, and "delamination" suggests an adhesion problem, we adopted the neutral term "separations" to avoid assuming the flaw origin. Uncored fired molds with separations could be used in casting by stuccoing over the surface at the foundry, but for cored molds separations resulted in failure of the core inside the integrally cored mold. It was found the separations could be addressed by modifying the curing behavior by adjustment suspension and build parameters.

7.2 Introduction: Development of Flaws in LAMP

Any production method has flaws characteristic to that method that must be addressed, for example the shrinkage porosity associated with aluminum casting. LAMP has its own characteristic flaws associated with the creation and assembly of many layers of cured material. There were addressed as part of the DARPA team in order to produce successful molds.

One characteristic flaw associated with LAMP is coined the "Shuffle." Shuffle flaws are diagonal lines that run across the build at an angle to the build plane. A shuffle flaw can be seen in Figure 7.1. The shuffle itself is caused by the systematic shift of the illuminating print head. The LAMP UV cure system is adopted from a UV-setters, which expose UV sensitive ink plates used in high-quality printing. In the printing industry it was found that a systematic shift to the program "0 point" was needed to avoid burn-in or wear-out effects on the print head by illuminating the exact same pixels over many cycles. A shuffle was introduced where by the "0 point" of the print head is shifted by a few pixels on every cycle shifting the DMD relative to the image by a few pixels. The spreads the work load over the entire print head DMD, extending its life. This shuffle programming is retained in LAMP but due to the layered nature of the process the impacts are different. The shuffle moves the 0 point of the print head relative to the build on every layer. This means a point x in the build in layer n, x-(n), is illuminated by a different section of the print head on the next pass, so x-(n) is exposed by different pixels than x-(n+1). This shifting procedure is sketched in Figure 7.2. The shuffle itself does not produce flaws, but only systematically shifts them. The existence of any visible defect indicates there is a line defect in illumination occurring during the exposure. This can lead to diagonal effects such as the feature seen in Figure 7.1. This could be a line of dead pixels in the DMD or a misalignment between the actual area of illumination and that expected by the software. The consequence of this shuffling is that the flaws are systematically shifted across the build through the layers. Eliminating the shuffle can have dire consequences as seen in Figure 7.3. For the build in Figure 7.3, the shuffle was turned off, so that every point in the build x-y plain was illuminated by the same pixel of the print head on every layer. This lead to sharp vertical separations due to the same column of material being underexposed on each build layer. The "Shuffle" serves as an example of the characteristic problems addressed in a layered additive manufacture technique.

A far more serious characteristic challenge or defect in LAMP is the layer-layer separation. These are cracks or delaminations occurring between build layers as illustrated in Figure 7.4. The term separation is used here to avoid the suggestion of a cause associated with terms like crack and delamination. Internal illumination is used to to highlight the flaws, a procedure adopted by UM and GT from Tom Van Vranken of PCC Airfoils Inc. Addressing these flaws was an area of intense prolonged work at both UM and GT. Initially these flaws were worked around in un-cored molds by application of a ceramic stucco at PCC over the LAMP build. This stuccoing sealed the mold and provided mechanical strength. However, in the case of cored molds the layer-separations caused failure of the cores which could not be addressed post-sintering. Figure 7.5 displays a core with a separation flaw visible in the flag region of the core.

7.3 Development of LAMP Separations

Initial efforts to address the layer-separations focused on slowing the binder-burnout process as this seemed a likely culprit. During binder-burnout the pyrolysis of the acrylate binder can cause stress as gas develops and escapes from the build. Processes that include a binder burnout it are widely observed to produce failures during pyrolysis of the binder.[1] However, it was found that slowing binder-burnout did not seem to address the issue.

Separations were found to occur very early in the binder burnout process prior to significant mass-loss. It was even found in some cases that molds developed separation flaws after aggressive development similar to those seen after burnout. (Development is the process used to remove the un-cured suspension as described in Chapter 1.) In 2011 Phillip Dodge examined the development of these flaws in the early stages of burnout, including observation of burnout through a pyrex window. Dodge found the separations occurred very early in burnout prior to any real pyrolysis or actual burning out of the binder. He also found that dye applied to green builds at room temperature highlighted specific inter-layer lines that later developed into separations as seen in Figure 7.6. To produce the effect seen in Figure 7.6 a line of food coloring was applied to the green mold with a cotton swab. The dye was found to spread from the application site along lines parallel to the build layer. These lines the dye flowed through became layer separations during BBO. These findings suggest the features that become layer separations are present in the green state but only become visible during binder burn out.

Three hypotheses on the origin of these flaws have been explored by the LAMP team: (1) Undercured Monomer Hypothesis, (2) Residual Stress Hypothesis, (3) Over-cured Surface Hypothesis. The Undercured Monomer Hypothesis posits that undercured monomer from incomplete polymerization can exist at the bottom of the build layer. This undercured material can be thermally initiated and continue polymerization early in BBO leading to shrinkage stress and crack formation. This undercured layer would also be vulnerable to attack by solvents leading to the observed separations after intense development. The Residual Stress Hypothesis posits that shrinkage stresses develop during polymerization and theses stresses are relieved by periodic layer separations. The Overcured Surface Hypothesis posits that the top surface of a build layer must retain some degree of undercure to allow proper adhesion to the subsequent layer.

Each of these hypotheses depends on the degree of curing through the build layer. An intense program to systematically adjust the photocuring behavior by changing the suspension and exposure was undertaken and it was ultimately found that certain conditions were associated with crack-free builds. The suspension formulation and build parameters were systematically adjusted at GT and molds were subsequently fired at UM to evaluate the degree of layer separations. The formulations of the builds produced between November 2012 and March 2103 can be seen in Table 7.1 , and the formulations of the builds between April 2013 and July 2013 can be seen in Table 7.2 . These tables present the formulation parameters relating to the concentration of components in the photosuspension and build parameters relating to the LAMP machine and environment. Many parameters were held constant across builds while others were varied. The goal of the GT team was to produce high resolution builds that fully captured the needed detail. Molds that were considered a success in the green state were shipped to UM for subsequent firing.

The formulation parameters impact the attenuation of light within the suspension and the curing behavior of the suspension. The impact of these parameters is governed by the equations presented in Section 7.4.1. The build parameters are those of the LAMP machine and the environment. Build parameters include the layer thickness, the surface exposure dose E_0 which is controlled by the exposure time and UV source intensity, the build temperature, and the build humidity.

The occurrence of separations were found to vary in a complicated and somewhat stochastic way with the formulation and build parameters, necessitating the larger number of tests. For the sake of brevity, only the results of two characteristic formulations are discussed in detail here. These are presented in Section 7.6. These were chosen as one represents the best parameters for build resolution and the other the best parameters for minimizing layer separations. Both were found to be repeatable although only the two builds are discussed. Before addressing these specific cases, the theoretical frame work must be established.

7.4 Curing as a Function of Exposure and Suspension Parameters:

7.4.1 Introduction to the Photopolymerization of LAMP Slurries

The suspension is a complex system, and the photo-curing a complex process. The suspension is composed of acrylate monomers, photo-initiators, dyes, inhibitors, and dispersant mixed with 60 vol% silica powder. The curing behavior is dependent upon all of these components as the sensitivity of the suspension to UV is modified along with the dissipation of the UV by various means. They relationship between the the formulation and the photocuring behavior was extensively studied by Vladislava Tomeckova, Susan Gentry, and John Halloran and the following description of photopolymerization behavior is adopted from their work.[2, 3, 4, 5, 6, 7, 8, 9, 10, 11] I did not participate in the development of the models reported here, but rather used them in collaboration with the rest of the LAMP team to address curing issues related to LAMP.

The attenuation with depth can generally be described by the Beer-Lambert formulation as follows:

$$E(z) = E_o exp\left(\frac{-z}{D_p}\right) \qquad Eq. 7.1$$

where *E(z)* is the energy at a depth of *z*, E_o is the total surface energy dose, and D_p is a sensitivity parameter of the suspension. This D_p can in turn be defined in terms of the suspension formulation by:

$$\frac{1}{D_p} = \frac{1}{l_{sc}} + (1 - \Phi)\left(C_p \varepsilon_p + C_D \varepsilon_D\right) \qquad Eq. 7.2$$

In which l_{sc} is the UV scattering length of the suspension, Φ is the volume fraction of ceramic, C_p is the photoinitiator concentration, ε_p is the extinction coefficient of the photoinitiator, C_D is the dye concentration, and ε_D is the extinction coefficient of the dye.

The depth of cure in a given formulation can be defined as the depth at which E(z) diminishes to the point that the suspension does not reach sufficient cure for gelation and remains liquid. So cure depth, z_{cure} is the depth at which E(z) reaches the critical energy E_c of gelation.

$$Z_{cure} = D_p ln\left(\frac{E_0}{E_c}\right) \qquad Eq. 7.3$$

in which D_p is previously defined, E_0 is the surface energy dose, and E_c is the critical energy dose. This E_c can in turn be found from the suspension parameters by the following:

$$E_c = (1 - \Phi)\frac{h\nu}{\Omega}(\gamma_{inh} C_{inh} + \gamma_D C_D)\frac{1}{C_P \varepsilon_p} \qquad Eq. 7.4$$

where C_{inh} is the concentration of inhibitors, γ_{inh} is the number of radicals absorbed per inhibitor molecule, γ_D is the number of radicals that never formed due to the dye present, h is Plank's constant, ν is the frequency of the exposing light, and Ω is the number of free radicals given off per photon absorbed.

7.4.2 Degree of Cure as a Function of Depth

We are interested in determining the degree of monomer conversion, α, as a function of the exposure energy dose, E_o, the layer thickness, H, the critical photocuring dose, E_c, and the photocuring sensitivity, D_p. The polymerization was previously reported on by Tomeckova et al utilizing photorheology and photocalorimetry to relate monomer conversion to energy dose.[6, 9, 10, 11] This information will be utilized to develop a model for the degree of cure through the layer thickness.

In non-photo-bleaching systems the intensity of the UV attenuates with depth by the Beer-Lambert relation, Eq.7.1. The relationship between the attenuation parameters and formulation are described in the previous section. The energy dose with depth as a function of initial energy dose is presented in Figure 7.7 for a range of D_p values. It can be seen that for low values of D_p the energy quickly attenuates with depth, while for larger values of D_p there is less attenuation and much larger energy dose is present at much greater depth.

We can define an E_c as the dose required for gelation and an E_{max} as the energy dose required for full polymerization. By this convention E_c is the minimum critical dose to produce solid, and E_{max} is the energy to cure the monomer as fully as possible. As the energy dose increases from E_c to E_{max} the degree of polymerization increases. The actual intensity from a range of exposures given a constant D_p is plotted against E_{max}, E_c, and the layer-thickness in Figure 7.8. We can see for the E_1 the energy dose is not above E_c through the entire layer depth, which will result in liquid at the bottom of the build layer. For E_4 the energy dose is above E_{max} for the entire depth of the build layer so the polymer is fully cured through the entire depth. This energy attenuation is well established, and the variation of D_p with formulation is well known.

The polymerization physics is not as firmly quantified as the energy attenuation, but the general behavior is still well understood. Figure 7.9 presents an idealized plot of monomer conversion as a function of energy dose. The gel point of ~0.2-03 is reached at the critical energy dose E_c, and polymerization continues until asymptoting to a conversion of ~0.8 at E_{max}. The polymerization will always exhibit an S-curve, but there is no simple expression to describe it quantitatively. Published rheology data can be used to estimate the parameters of polymerization.[6, 9, 10, 11]

The well known attenuation with depth can be combined with the monomer conversion with dose to produce a plot of conversion with depth. This is seen in Figure 7.10. We can now examine the degree of conversion with depth and consider undercure and overcure. Undercure can be defined as material within a single layer not exposed to E_{max}, while overcure is any exposure to a dose of E_c or greater at depths beyond layer thickness. Undercured material within the layer may be tied to separation flaws by thermal polymerization during BBO or solvent attack during development. While overcure can limit resolution when material under the cured layer is unintentionally polymerized. (Such as when producing arch-like structures) In Figure 7.10 the undercure in the build layer and the over cure beyond the layer depth are highlighted.

Moving beyond these schematic representations we can develop expressions for this conversion with depth. The depth at which energy falls below the level needed for gelation and monomer remains liquid can be defined as z_{liq} and given by Equation 7.2:

$$z_{liq} = D_p ln\left(\frac{E_o}{E_c}\right) = C_D \qquad Eq. 7.5$$

where C_D is the cure depth. The depth of full cure can likewise be defined as:

$$z_{FC} = D_p ln\left(\frac{E_o}{E_{max}}\right) \qquad Eq. 7.6$$

Ideally both z_{liq} and z_{FC} would be exactly equal to the layer thickness H. The entire build layer would be fully cured and no curing would occur below the layer. In reality, z_{FC} will be less than H and there will be undercure, or z_{liq} will be much greater than H and there will be overcure, or both will occur to some extent as in Figure 7.10.

The energy to achieve full conversion is not well known and must be estimated. It can be defined as a multiple of the critical energy such that:

$$E_{max} = BE_c \qquad Eq. 7.7$$

Here B is a "polymerization parameter" which we must approximate. The published photorheology data available can be used to find the relationship between the critical and maximum energy dose. The induction time, t_o, half reaction time, t_{50}, and reaction period, Δt, can be used. It's known that induction time is a function of the critical energy dose. Perhaps we can assume the conversion maximum occurs two periods after t_{50} and can be approximated as $t_{max}= t_{50}+2\ \Delta t$. This would imply $B=(t_{50}+2\ \Delta t)/t_o$. B can be approximated from the photorheology data from Tomeckova et al.[6, 10, 11]

Using $B= (t_{50} +2\ \Delta t)/t_o$, it seems that for the PI series, (no absorber dye, no added inhibitor), it seems that B varies from 1.9 to 5.6, increasing with PI concentration linearly, as described by $B= 1.3+ 21C_{PI}$, with C_{PI} being the PI concentration in moles/liter. For the series with absorber dye, B does not vary greatly with dye concentration, so we can use B=2.2 +/-0.5 for cases with constant PI and variable dye. Added inhibitor does not change B much, and the 4 data points can be represented by B=1.23+/- 0.05.

Using our approximation for E_{max} we can make write an equation for the degree of cure as a function of energy dose:

$$\alpha(E) = \alpha_{gel} + \frac{(\alpha_{max} - \alpha_{gel})}{(B-1)}\left(\frac{E}{E_c} - 1\right) \qquad Eq. 7.8$$

If we assume a gel point of 30% conversion and a maximum conversion of 80% we can rewrite Equation 7.5 as:

$$\alpha(E) = 0.3 + \frac{(0.5)}{(B-1)}\left(\frac{E}{E_c} - 1\right) \qquad Eq. 7.9$$

We can now substitute depth for energy using Eq.7.1 to develop a form for the degree of conversion with depth:

$$\alpha(z) = \left[\alpha_{gel} - \frac{(\alpha_{max} - \alpha_{gel})}{(B-1)}\right] + \frac{(\alpha_{max} - \alpha_{gel})}{(B-1)}\left[\frac{E_o}{E_c}\right]\exp\left(\frac{-z}{D_p}\right) \qquad Eq. 7.10$$

Eq.7.10 correctly reports that $\alpha(z=C_D)=\alpha_{gel}$ and that $\alpha(z=z_{FC})=\alpha_{max}$. This suggests we can accurately use Eq.7.10 to model the degree of polymerization with depth.

We can also rewrite z_{FC} as a function of B and E_c rather than E_{max}:

$$z_{FC} = D_p ln\left(\frac{E_o}{E_{max}}\right) = D_p ln\left(\frac{E_o}{BE_c}\right) \qquad Eq.7.11$$

At z_{FC} $\alpha(z)=\alpha_{max}$ while the decay in conversion for depths greater than z_{FC} can be written:

$$\alpha(z) = \alpha_{max} exp\left(\frac{-[z - z_{FC}]}{D_p}\right) = \alpha_{max}\frac{E_o}{BE_c} exp\left(\frac{-z}{D_p}\right) \qquad Eq. 7.12.$$

A full "proper dose" could be defined as Ep where the fully cured depth Z_{fc} is equal to the layer thickness:

$$z_{FC} = H = D_p ln\left(\frac{E_p}{BE_c}\right)$$

The dose that fully cures a layer H will be:

$$E_p = BE_c exp\left(\frac{H}{D_p}\right) \qquad\qquad Eq. 7.13$$

This reports the does required to prevent undercure. The opposite will be the overcure or cure beyond the depth H.

$$C_d = D_p ln\left(\frac{E_p}{E_c}\right) = D_p ln\left[\frac{BE_c exp\left(\frac{H}{D_p}\right)}{E_c}\right] = D_p lnB + H \qquad Eq. 13$$

The OC=(Cd-H) is simply:

$$OC = D_p$$

The degree of cure as a function of depth was examined experimentally but the attempts were unsuccessful. First, green molds were cross sectioned and polished to provide a view of the build layers. These samples were examined by RAMAN spectroscopy using green laser excitation. However, the samples were found to fluoresce, preventing data collection. The same polished cross sections were examined under UV-vis microscopy under the hope that the degree of fluorescence would correlate to the degree of polymerization. Samples were stimulated with UV and the emissions were observed by optical microscopy. Unfortunately no contrast with-in layers was found. The degree of polymerization through the layer was then examined by mechanical means. Samples were indented across the build layer with a micro-Vickers hardness tester. Unfortunately, indentions were not observable. The material compliance and roughness (due to ceramic particles of up to 30 microns in size) prevented formations of observable Vickers indents. Finally, the material was serially sectioned in the build direction by careful polishing. Incremental amounts of material were polished from the green build and collected. The collected material was examined with FTIR by the method used by Kahn Wu.[12] However, no contrast could be developed between sections due to a combination of small sample size and contamination. Ultimately the experimental verification of degree of cure across the layer thickness was not completed. This would be a fruitful area for future research, perhaps accomplished by serial sectioning by microtome sectioning.

7.5 Overcure vs Undercure

It can be seen schematically in Figure 7.10 and inferred from Eq.7.9 that there is a trade off between overcure and undercure. An energy dose sufficient to eliminate undercure by reaching E_{max} at a depth H will also supply a dose greater than E_c for some depth beyond a depth H leading to overcuring. Similarly, an energy dose sufficiently small to eliminate overcuring by diminishing below E_c at a depth of H will also fall below E_{max} at depths less than H resulting in undercuring. One could imagine a system with an very small D_p and very high dose such that E(z) diminishes very rapidly and passes both E_{max} and E_c over a short range near a depth of H. However, creating such an extreme system is not truly feasible. This forces us to accept certain degrees of undercuring and overcuring while attempting to mitigate layer separation.

The Undercured Monomer Hypothesis posits that layer separations occur as a result of undercured monomer. Undercured monomer can be thought of as a gel of acrylate polymer that is saturated with acrylate monomer. It was originally proposed by Chang-Jun Bae that cracking in molds produced by similar stereolithography techniques was caused by retained uncured monomer.[13] At temperatures of ~200°C the photoinitiator becomes a thermal initiator. This could result in continued polymerization of undercured monomer in the early stages of BBO resulting in stresses and separations. The resulting separations would occure prior to mass-loss, consistent with the Dodge observations. Alternatively, the monomer may evaporate from undercured material producing stresses. This would occur prior to pyrolysis of the polymer and significant mass loss, but would itself constitute limited mass loss. Additionally, undercured material could be expected to be more vulernable to attack by solvents potentially explaining the appearance of separations during aggressive development similar to those that appear during BBO. According to the Undercured Monomer Hypothesis, separations could be eliminated by eliminated undercuring. This suggests that to eliminate separations we must accept a large degree of overcuring and ensure full curing through the layer thickness H. The Undercured Monomer Hypothesis could explain the development of separations during both BBO and overly aggressive development, and could be addressed by full curing through the build layer.

The Residual Stress Hypothesis posits that stress develops from curing shrinkage leading to layer separations. Two forms of this theory have been advanced. The first was presented by Mathew Conrad of GT who suggested continued curing of layer n during exposure of layers n+1 and higher lead to the development of stress.[14] This view runs counter to the model developed in Section 7.4 since during the exposure of the n+1 layer any undercured material in layer n must fall at a depth of $H+Z_{FC}$ and if the $E(Z_{FC})$ is the energy for full cure then $E(H+Z_{FC})$ must be must smaller. An alternate version of the Residual Stress Hypothesis posits that shrinkage stresses develop during curing and these stresses are relieved by separation of layers during BBO when the material is at its weakest. (This is being pursued by Tao Wu of Georgia Tech and will explored in greater detail in his thesis forthcoming in 2014) This approach takes the view that shrinkage is an inherent feature of polymerization and therefore stress development over many layers is a natural outcome. By this reasoning, some undercure in every layer is desirable as the undercured material retains the plasticity necessary to relax stress. This presents a solution to layer separations by ensuring undercuring allowing for formulations and exposures that eliminate overcuring. This is the opposite of the suggestion of the Undercured Monomer Hypothesis.

The Overcured Surface Hypothesis posits that for proper layer-layer adhesion the surface must be cured to a degree less than α_{max} allowing for cross-polymerization to join the layers. This suggests that formulations with large D_p and slow attenuation are desirable, allowing for the surface exposure E_o and the exposure $E(H)$ at the layer interface to both fall between E_c and E_{max}. This facilitates the continued polymerization at the interface ensuring bonding between the layers. The Overcured Surface Hypothesis differs from the prior two in 2 significant ways. Firstly, it does not explain the driving force that leads to separations but instead attempts to address weak layer-layer bonding that would make the layers vulnerable to separating. Secondly, the Overcured Surface Hypothesis suggest that a large degree of both undercuring and overcuring are necessary and desirable. This makes the Overcured Surface Hypothesis compatible with the Residual Stress Hypothesis suggesting a moderate cure with low attenuation will eliminate layer separations.

A further concern beyond addressing layer separations is resolution. Deep undercuring will polymerize material deep below the surface layer leading to unintended curing in the case of overhanging features. This overcuring can be detrimental to the creation of the fine and intricate features of an airfoil core.

7.6 Case Study: High vs Low Sensetivity

The proposed mechanisms addressing layer separations differ in what formulation and cure are expected to produce molds without separation flaws. To evaluate them a case study between a deep curing undercured build optimized to prevent layer separations was compared to a build with a large exposure and small D_p optimized for feature resolution.

These builds were designated 6/27 and 7/1 for their build dates. 6/27 was optimized to reduce separation and had a D_p of 1000 microns, an EC of 68.3 mJ/cm^2, and an exposure dose of 102 mJ/cm^2. 7/1 was optimized for feature resolution and had a D_p of 200 microns, an E_C of 85.8 mJ/cm^2, and an exposure dose of 242 mJ/cm^2. Thus the D_p's differed by an order of 5 and the exposure doses by nearly half that factor. The energy with depth is plotted in Figure 7.11 while the degree of cure using Equation 7.11 is plotted in Figure 7.12. The build 6/27 was a deep cure with low attenuation and undercuring present at the surface. The build 7/1 displays very little undercuring and much faster attenuation balanced by a larger exposure energy dose. Both display significant overcuring, although in the case of 7/1 this was known not to be a problem for feature resolution.

The 6/27 and 7/1 builds are compared side by side with internal illumination in Figure 7.13. There were no visible layer separations in build 6/27, while 7/1 had significant layer separations. In the case study cylinders were produced as the goal was to eliminate separations. The ability of the parameters used for 6/27 to produce good resolution in an airfoil core is unquantified, but it is known that 7/1 is superior in this regard.

The much improved layer separation of 6/27 validates the Residual Stress and Overcured Surface Hypotheses. Although, it could be argued that since undercuring was present in both cases the Undercured Monomer Hypothesis was not properly evaluated. In 6/27 the surface was undercured and the degree of curing was very consistent across the layer. E(z) was larger than E_c for several layers into the material which combined with the undercured surface should promote layer adhesion by the Overcured Surface Hypothesis. The large amount of undercuring should also have promoted relaxation of polymerization stresses.

These results suggest that a consistent deep cure with slow attenuation results in far fewer layer separations relative to a faster attenuation and deep cure optimized to reduce both over and under cure. It also illustrates that overcure is not as detrimental to feature resolution as feared. The conditions used for build 7/1 were selected as it was known to have excellent feature resolution but it still had significant overcure.

7.7 Conclusions

The layer separations present in LAMP builds can be addressed by adjusting the photopolymization parameters. It was found that deep even curing minimized the occurrence of layer separations. This is consistent with the view that an undercured surface promotes layer adhesion and low degree of curing promotes relaxation of polymerization stresses. The results suggest that presence monomer cured between the gel-point and the maximum cure does not produce layer separations. That the optimal formulation for resolution does not correspond to the optimal formulation for minimizing separations suggests that a compromise must be made.

Further work past the DARPA project conducted at PCC Airfoils and DDM Systems suggests that the selection of ceramic may impact layer separations as well. However, that is beyond the scope of this work.

7.8 References

1. K. E. Hardina, J. W. Halloran, M. Kaviany, and A. Oliveira, "Defect Formation During Binder Removal in Ethelyne Vinyl Acetate Filled System," *J. Mater. Sci.,* 34 3281-90 (1999).
2. C. J. Bae and J. W. Halloran, "Integrally Cored Ceramic Mold Fabricated by Ceramic Stereolithography," *International Journal of Applied Ceramic Technology,* 8[6] 1255-62 (2011).
3. S. P. Gentry and J. W. Halloran, "Depth and width of cured lines in photopolymerizable ceramic suspensions," *J. Eur. Ceram. Soc.,* 33[10] 1981-88 (2013).
4. S. P. Gentry and J. W. Halloran, "Absorption effects in photopolymerized ceramic suspensions," *J. Eur. Ceram. Soc.,* 33[10] 1989-94 (2013).
5. J. W. Halloran, V. Tomeckova, S. Gentry, S. Das, P. Cilino, D. J. Yuan, R. Guo, A. Rudraraju, P. Shao, T. Wu, T. R. Alabi, W. Baker, D. Legdzina, D. Wolski, W. R. Zimbeck, and D. Long, "Photopolymerization of powder suspensions for shaping ceramics," *J. Eur. Ceram. Soc.,* 31[14] 2613-19 (2011).
6. V. Tomeckova and J. W. Halloran, "Radical depletion model for intensity effects on photopolymerization," *J. Eur. Ceram. Soc.,* 33[1] 25-35 (2013).
7. V. Tomeckova and J. W. Halloran, "Porous Ceramics by Photopolymerization with Terpene-Acrylate Vehicles," *Journal of the American Ceramic Society,* 95[12] 3763-68 (2012).
8. V. Tomeckova and J. W. Halloran, "Macroporous polyacrylates from terpene-acrylate thermoreversible photopolymerizable vehicle," *J. Mater. Sci.,* 47[16] 6166-78 (2012).
9. V. Tomeckova and J. W. Halloran, "Critical energy for photopolymerization of ceramic suspensions in acrylate monomers," *J. Eur. Ceram. Soc.,* 30[16] 3273-82 (2010).
10. V. Tomeckova, S. J. Norton, B. J. Love, and J. W. Halloran, "Photopolymerization of acrylate suspensions with visible dyes," *J. Eur. Ceram. Soc.,* 33[4] 699-707 (2013).
11. V. Tomeckova, F. Teyssandier, S. J. Norton, B. J. Love, and J. W. Halloran, "Photopolymerization of acrylate suspensions," *J. Photochem. Photobiol. A-Chem.,* 247 74-81 (2012).
12. K. Wu, "Parametric Study and Optimization of Ceramic Stereolithography," pp. 332. in Materials Science and Engineering, Vol. PhD. University of Michigan, 2005.
13. C. J. Bae and J. W. Halloran, "Influence of Residual Monomer on Cracking in Ceramics Fabricated by Stereolithography," *International Journal of Applied Ceramic Technology,* 8 1289-95 (2011).

14. M. Conrad, "Experimental Invstigations and Theoretical Modeling of Large Area Maskless Photopolymerization with Grayscale Exposure." in, Vol. Master of Science. Georgia Institute of Technology, 2011.

Table 7.1 LAMP Build Parameters Nov. 2012 through April 2013

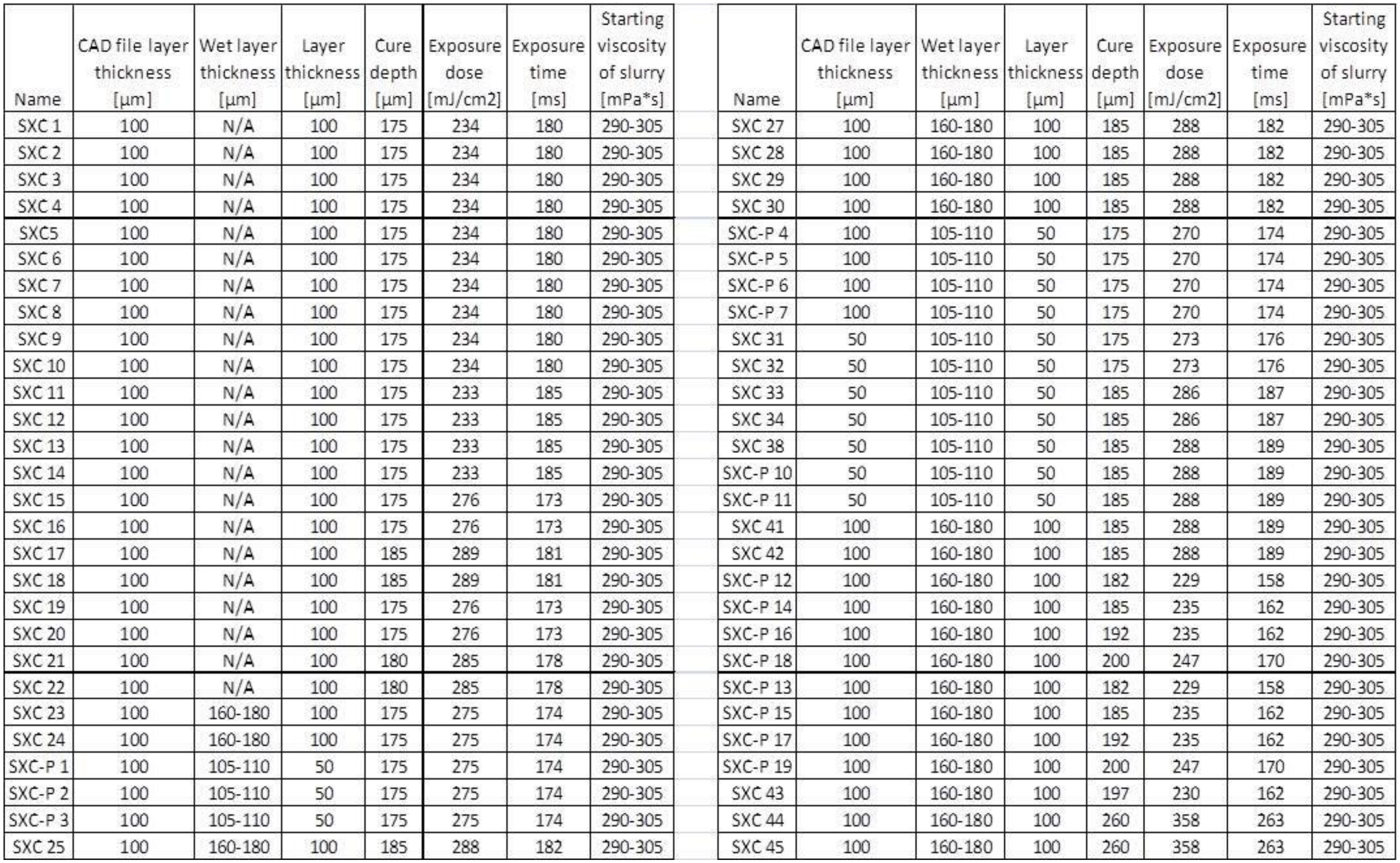

Name	CAD file layer thickness [μm]	Wet layer thickness [μm]	Layer thickness [μm]	Cure depth [μm]	Exposure dose [mJ/cm2]	Exposure time [ms]	Starting viscosity of slurry [mPa*s]
SXC 1	100	N/A	100	175	234	180	290-305
SXC 2	100	N/A	100	175	234	180	290-305
SXC 3	100	N/A	100	175	234	180	290-305
SXC 4	100	N/A	100	175	234	180	290-305
SXC5	100	N/A	100	175	234	180	290-305
SXC 6	100	N/A	100	175	234	180	290-305
SXC 7	100	N/A	100	175	234	180	290-305
SXC 8	100	N/A	100	175	234	180	290-305
SXC 9	100	N/A	100	175	234	180	290-305
SXC 10	100	N/A	100	175	234	180	290-305
SXC 11	100	N/A	100	175	233	185	290-305
SXC 12	100	N/A	100	175	233	185	290-305
SXC 13	100	N/A	100	175	233	185	290-305
SXC 14	100	N/A	100	175	233	185	290-305
SXC 15	100	N/A	100	175	276	173	290-305
SXC 16	100	N/A	100	175	276	173	290-305
SXC 17	100	N/A	100	185	289	181	290-305
SXC 18	100	N/A	100	185	289	181	290-305
SXC 19	100	N/A	100	175	276	173	290-305
SXC 20	100	N/A	100	175	276	173	290-305
SXC 21	100	N/A	100	180	285	178	290-305
SXC 22	100	N/A	100	180	285	178	290-305
SXC 23	100	160-180	100	175	275	174	290-305
SXC 24	100	160-180	100	175	275	174	290-305
SXC-P 1	100	105-110	50	175	275	174	290-305
SXC-P 2	100	105-110	50	175	275	174	290-305
SXC-P 3	100	105-110	50	175	275	174	290-305
SXC 25	100	160-180	100	185	288	182	290-305
SXC 27	100	160-180	100	185	288	182	290-305
SXC 28	100	160-180	100	185	288	182	290-305
SXC 29	100	160-180	100	185	288	182	290-305
SXC 30	100	160-180	100	185	288	182	290-305
SXC-P 4	100	105-110	50	175	270	174	290-305
SXC-P 5	100	105-110	50	175	270	174	290-305
SXC-P 6	100	105-110	50	175	270	174	290-305
SXC-P 7	100	105-110	50	175	270	174	290-305
SXC 31	50	105-110	50	175	273	176	290-305
SXC 32	50	105-110	50	175	273	176	290-305
SXC 33	50	105-110	50	185	286	187	290-305
SXC 34	50	105-110	50	185	286	187	290-305
SXC 38	50	105-110	50	185	288	189	290-305
SXC-P 10	50	105-110	50	185	288	189	290-305
SXC-P 11	50	105-110	50	185	288	189	290-305
SXC 41	100	160-180	100	185	288	189	290-305
SXC 42	100	160-180	100	185	288	189	290-305
SXC-P 12	100	160-180	100	182	229	158	290-305
SXC-P 14	100	160-180	100	185	235	162	290-305
SXC-P 16	100	160-180	100	192	235	162	290-305
SXC-P 18	100	160-180	100	200	247	170	290-305
SXC-P 13	100	160-180	100	182	229	158	290-305
SXC-P 15	100	160-180	100	185	235	162	290-305
SXC-P 17	100	160-180	100	192	235	162	290-305
SXC-P 19	100	160-180	100	200	247	170	290-305
SXC 43	100	160-180	100	197	230	162	290-305
SXC 44	100	160-180	100	260	358	263	290-305
SXC 45	100	160-180	100	260	358	263	290-305

Table 7.2 LAMP Build Parameters May through July 2013

Build Date	DP	EC	CD	E/Eo at Cd	E/Eo at 100 µm	Exposure	Viscosity	PI	Absorber	Dispersant	Ceramic	Wet layer thickness	Nominal thickness	CAD layer thickness	Ball milling	Machine chamber Temp.	Relative humidity
	(µm)	(mJ/cm^2)	(µm)			(ms)	(mpas)	(wt%)	(wt%)	(wt%)	(wt%)	(µm)	(µm)	(µm)	(h)	(F)	
5/30/2013	1053	58	383	0.695	0.909	58	345	4%	0%	8.3%	55%	300	100	100	48	64	NA
6/3/2013	718	40.5	545	0.468	0.870	60	371	6%	0%	2.0%	55%	300	100	100	72	64	NA
6/4/2013	751.2	37.4	492	0.520	0.875	50	379	6%	0%	8.3%	55%	300	100	100	72	64	NA
6/6/2013	701.1	44.4	490	0.497	0.867	62	482	6%	0%	2.0%	65%	300	100	100	72	64	NA
6/7/2013	489.8	29.8	505	0.357	0.815	58	359	4%	0%	8.3%	55%	300	100	100	48	64	NA
6/10/2013	919.2	46	549	0.551	0.897	58	346	6%	0%	2.0%	70%	300	100	100	72	64	NA
6/12/2013	795.5	39.4	570	0.489	0.882	58	348	6%	0%	8.3%	55%	300	100	100	48	64	NA
6/14/2013	829.8	36.8	300	0.697	0.886	38	324	4%	0%	8.3%	55%	300	100	100	48	64	NA
6/17/2013	910.4	63.3	391	0.651	0.896	70	374	2%	0%	8.3%	55%	300	100	100	48	59	49%-61%
6/22/2013	952.5	83.7	463	0.615	0.900	100	453	1.5%	0%	8.3%	55%	300	100	100	48	59	51%-61%
6/24/2013	831.8	50.4	402	0.617	0.887	60	402	4%	0%	8.3%	55%	300	100	100	48	59	50%-61%
6/27/2013	1003	68.3	402	0.670	0.905	75	455	4%	0%	8.3%	55%	300	100	100	48	59	49%-61%
7/1/2013	203.2	85.8	211	0.354	0.611	175	411	6%	0.25%	8.3%	55%	180	100	100	48	59	51%-61%
7/8/2013	205.4	84.7	231	0.326	0.615	215	397	6%	0.25%	8.3%	55%	180	100	100	72	59	47%-62%

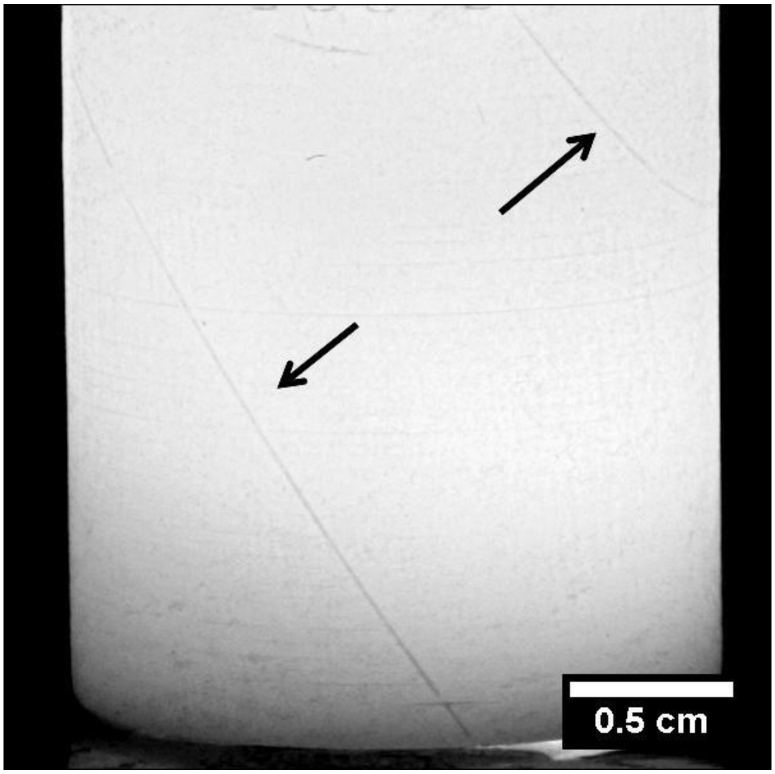

Figure 7.1 LAMP produced cylinder in Green state illustrating "Shuffle" flaw

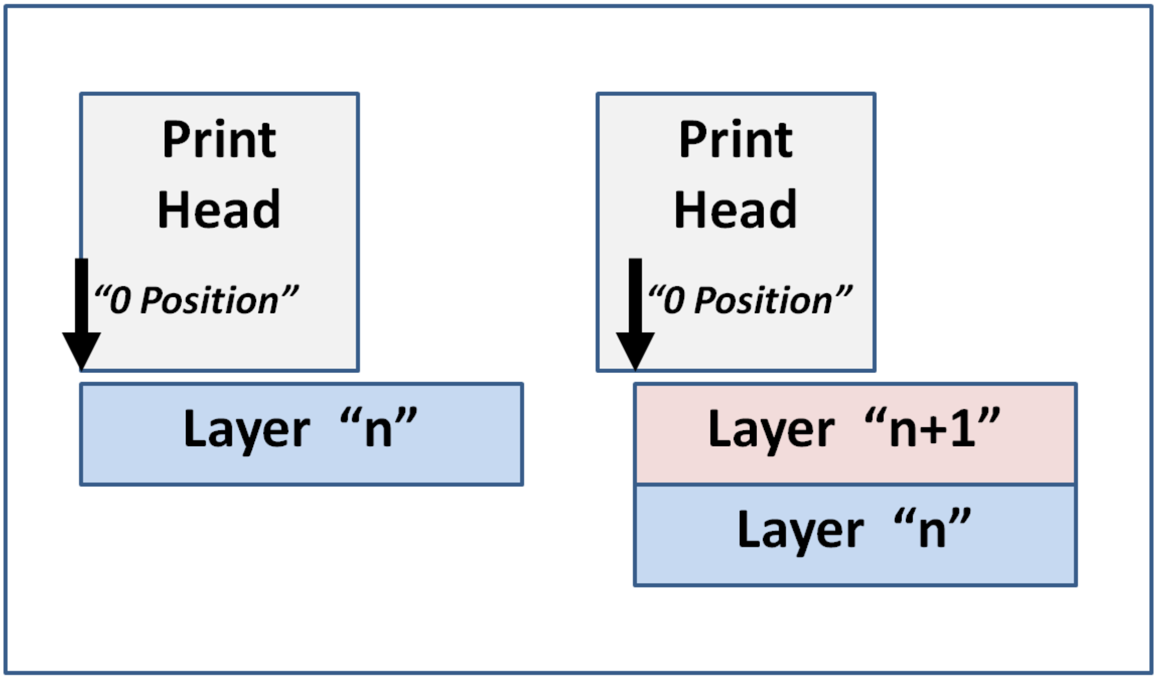

Figure 7.2 **Schematic of "Shuffle" procedure where by LAMP UV print-head shifts on each subsequent layer. The shuffle itself does not produce flaws, but can lead to the systematic shift of flaws from improper exposure.**

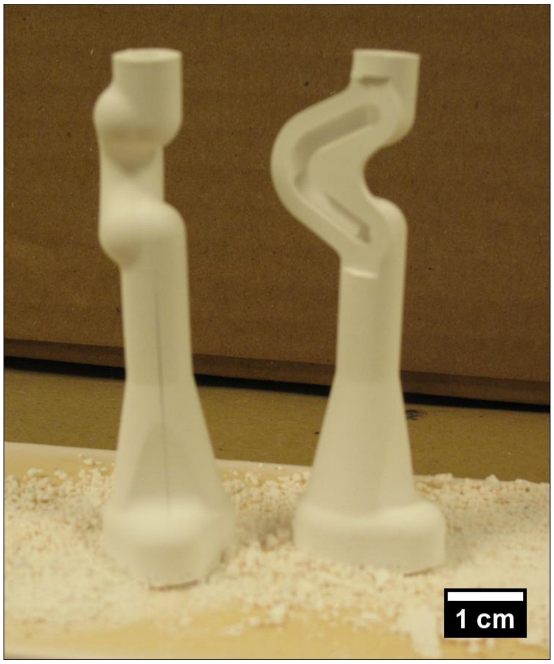

Figure 7.3 LAMP part produced with “shuffle” turned off resulting in uncured vertical plane flaw.

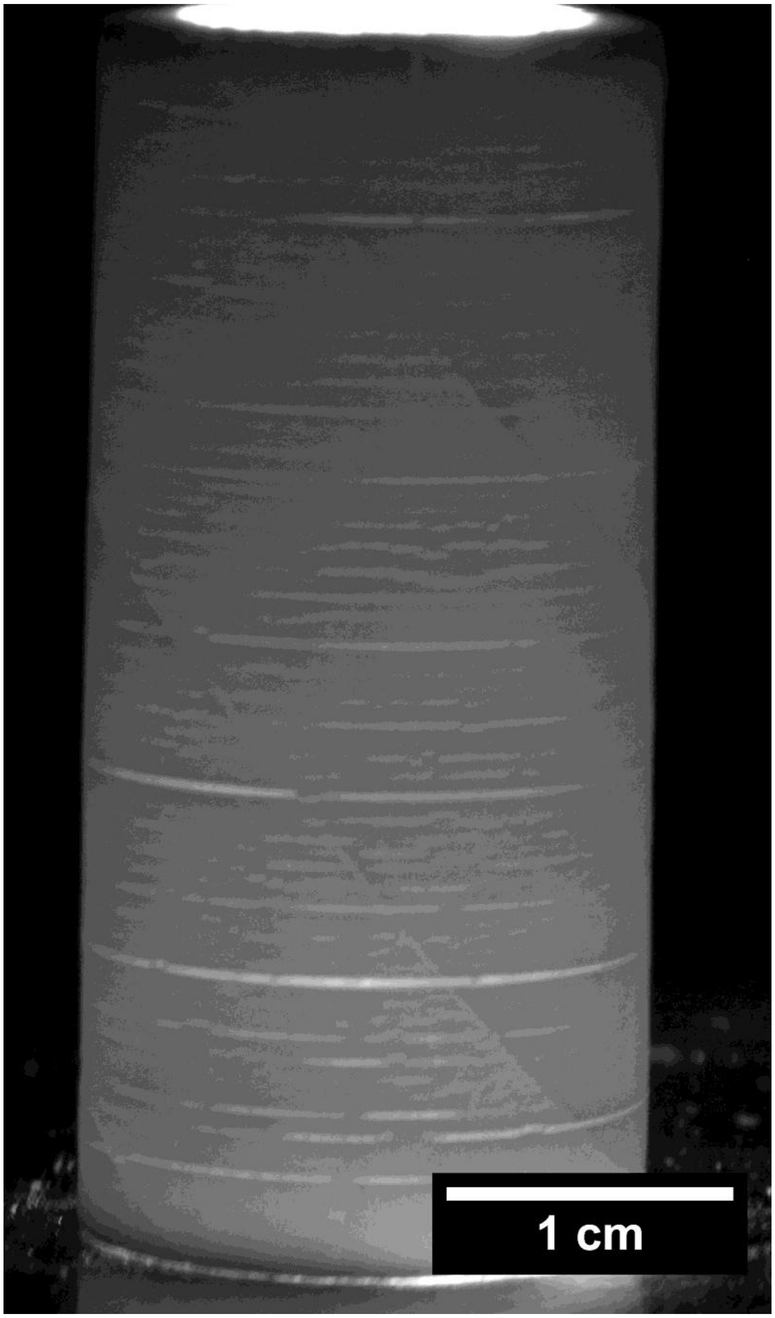

Figure 7.4 Internally illuminated sintered LAMP cylinder illustrating layer separations and shuffle flaws.

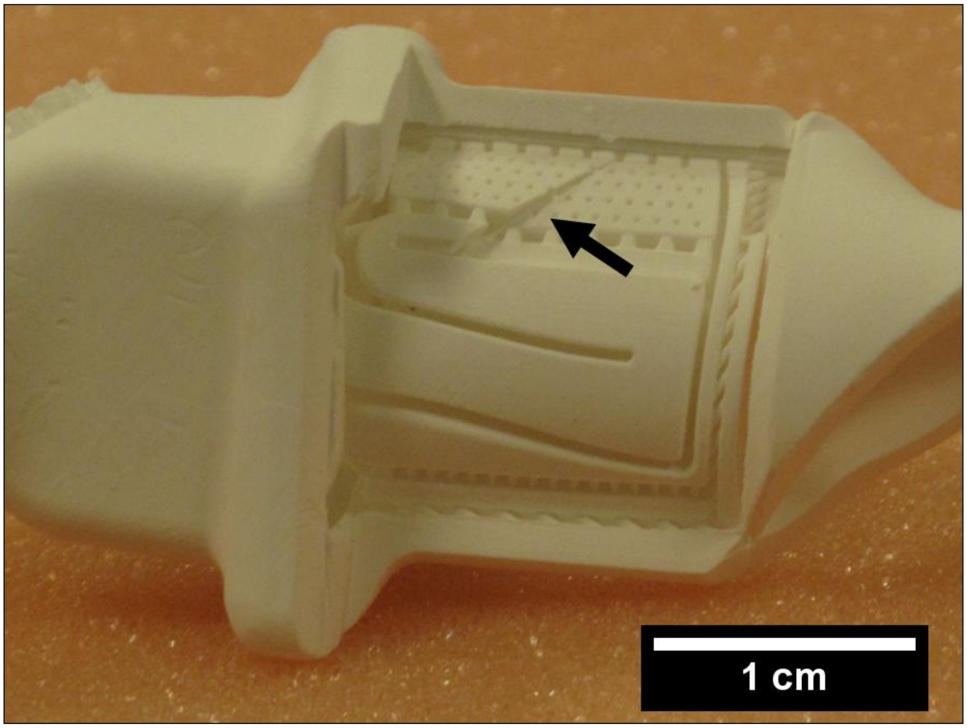

Figure 7.5 Cut-away view of cored mold with large separation flaw in the flag section of the core.

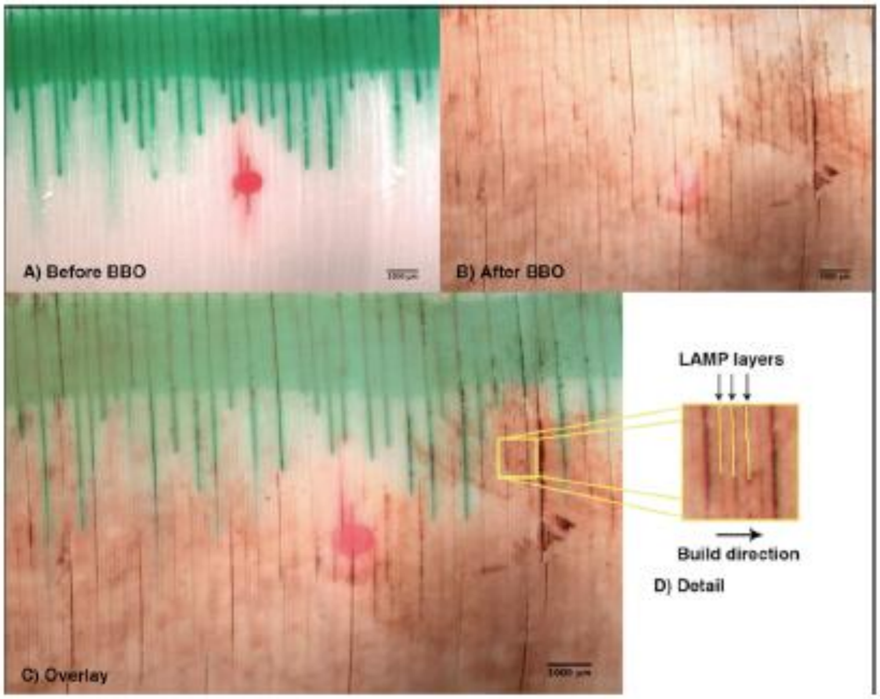

Figure 6: Stereomicroscope pictures of mold from Feb 25 BBO test. A) before BBO. Red dot is a dot of pen ink used to align the before and after pictures. B) After BBO. C) Computer generated overlay of A and B. Note how the green lines of dye from the before image match up with the dark cracks in the after image. D) Detail of cracks in mold, showing LAMP layer planes and build direction.

Figure 7.6 Dye Penetration of lines Prior to separation formation adopted from MSE 490 work performed by Philip Dodge.

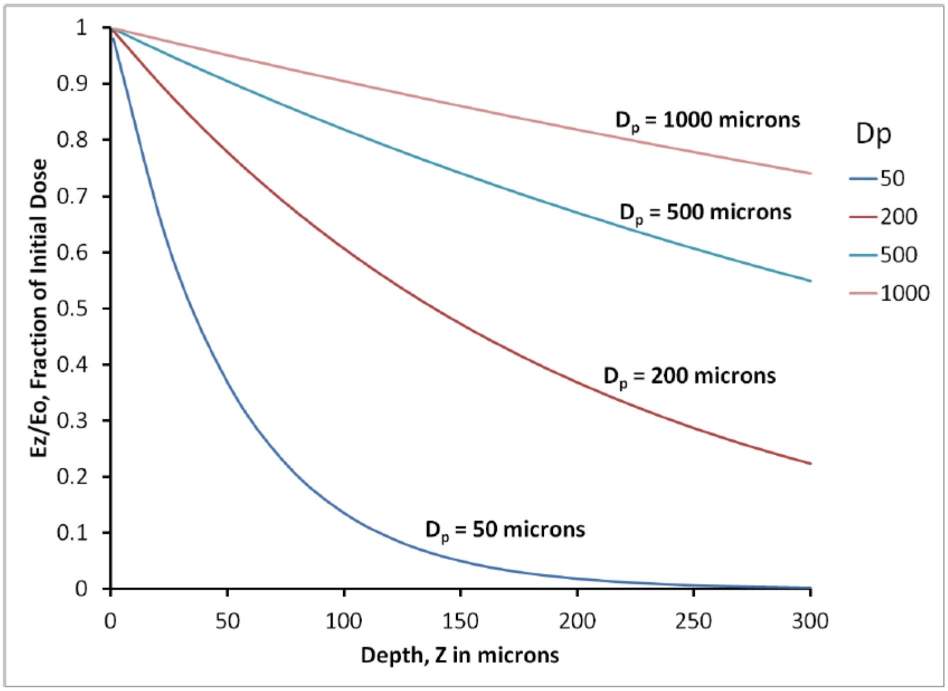

Figure 7.7 Normalized energy dose with depth for suspensions of varied sensitivity, Dp.

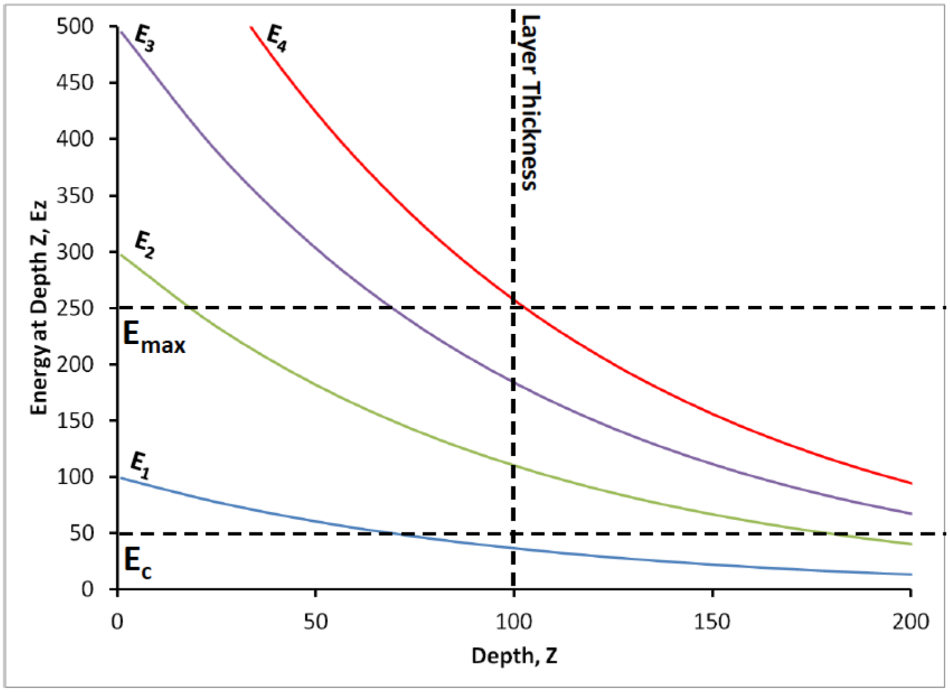

Figure 7.8 Energy dose with depth for various surface energy doses.

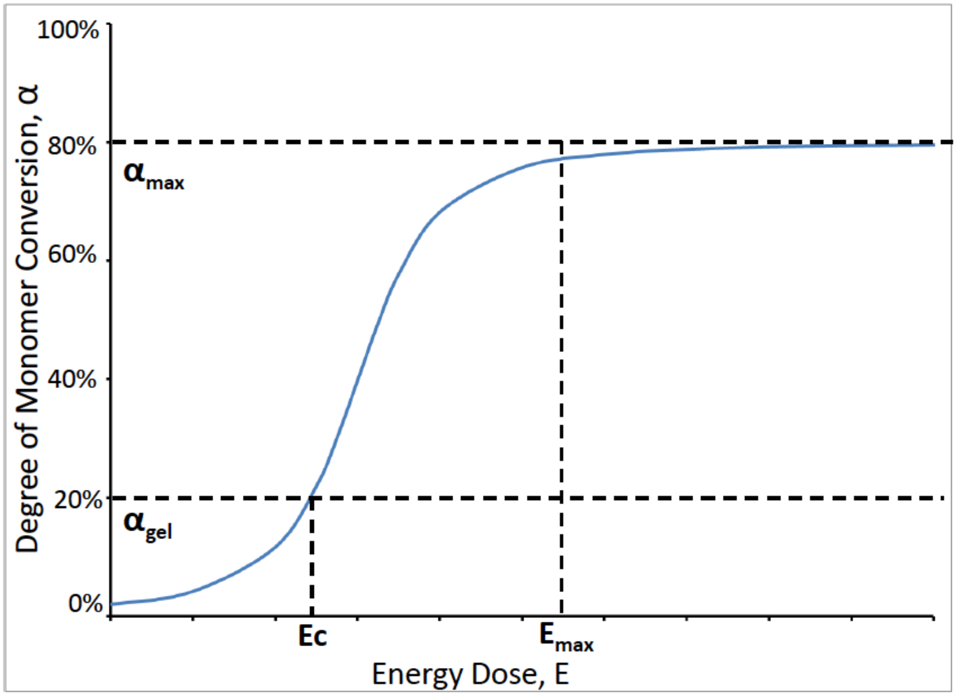

Figure 7.9 Degree of Conversion vs Energy Dose

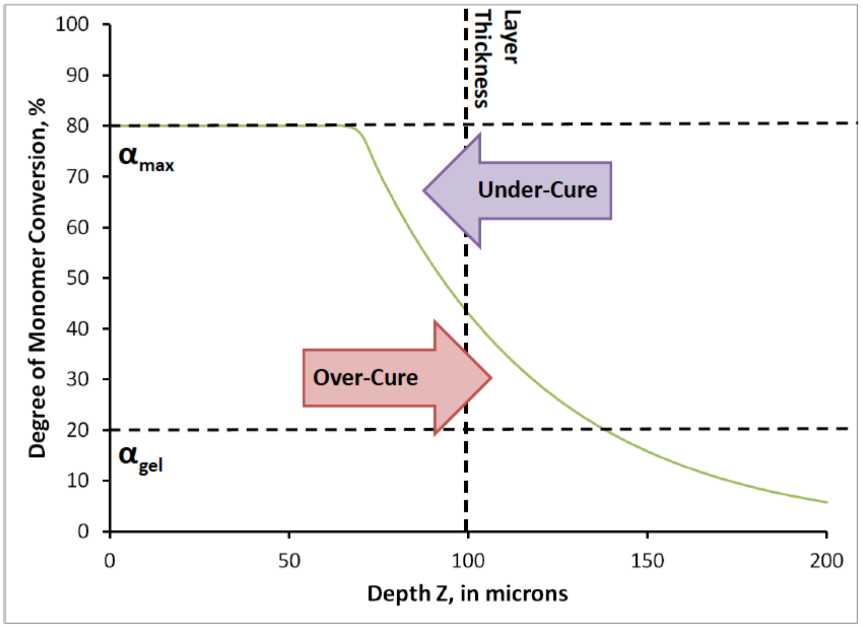

Figure 7.10 Degree of monomer conversion plotted as a function of depth illustrating Under-cure and Over-cure.

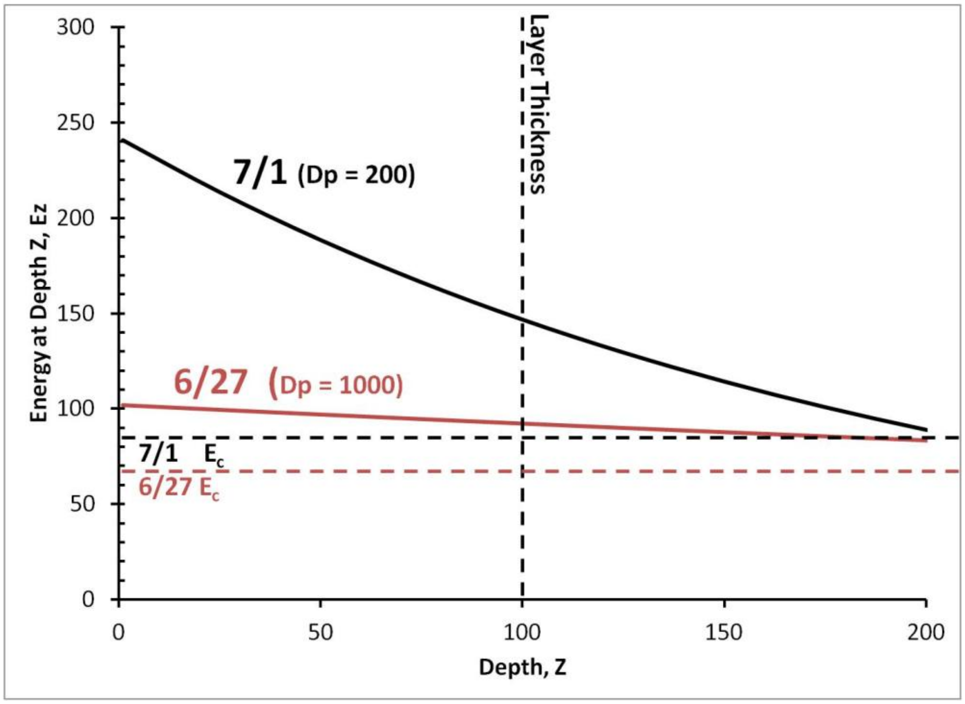

Figure 7.11 Case Study: Energy with depth for the 6/27 and 7/1 builds

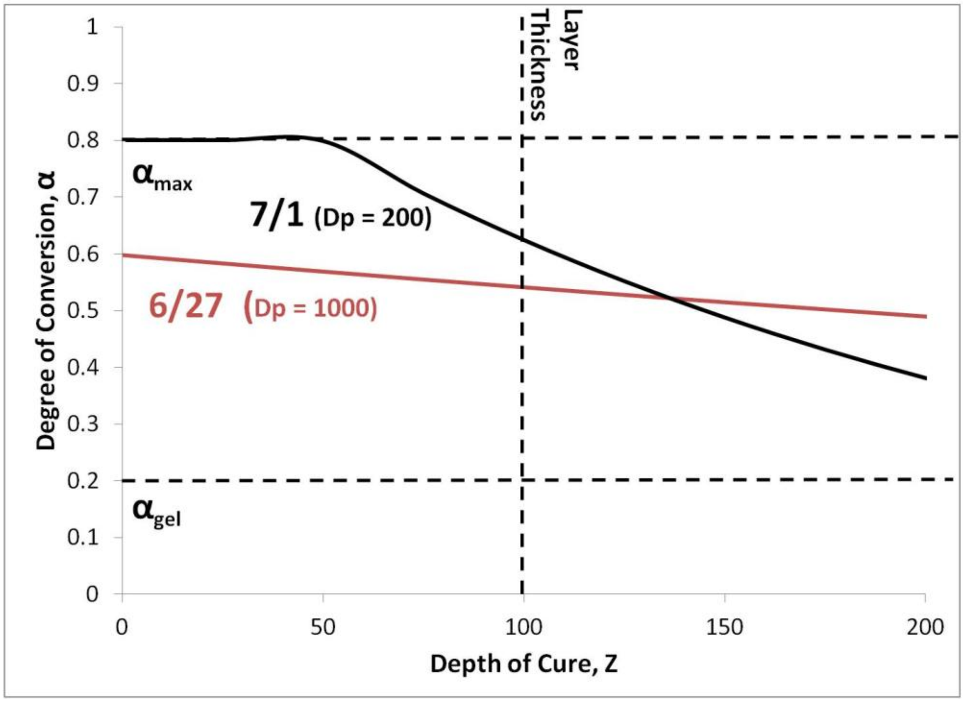

Figure 7.12 Case Study: Conversion with depth for the 6/27 and 7/1 builds

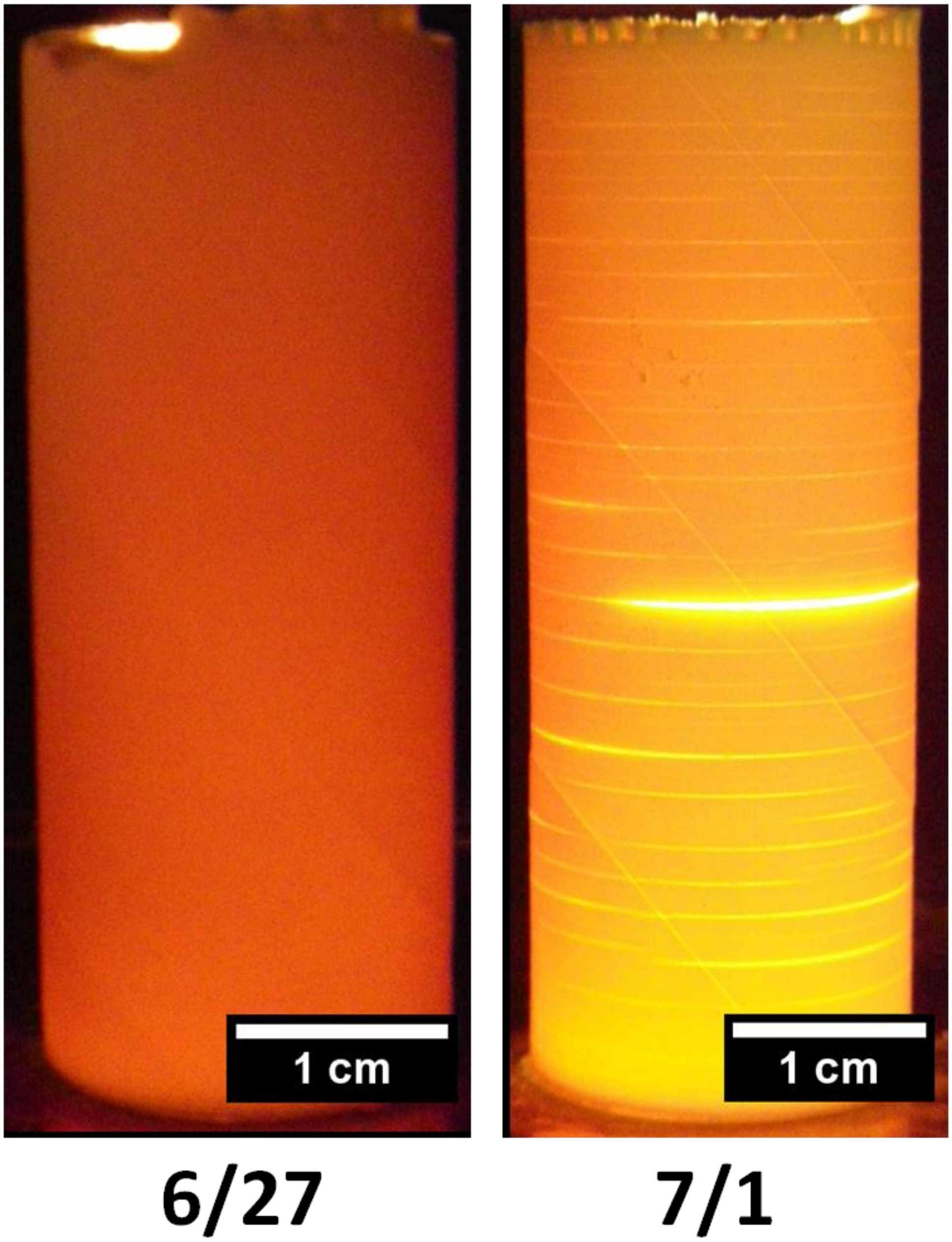

Figure 7.13 Case Study: Comparison of 6/27 and 7/1 builds by internal illumination

Chapter 8
Conclusions

8.1 LAMP as a Production Means for Airfoils

Single-crystal Ni-super-alloy was successfully cast in refractory molds produced by the new process of Large Area Maskless Photopolymerization, LAMP, demonstrating that refractory casting molds can be produced by 3-D printing methods. The LAMP 3-D printing process of photocuring a ceramic loaded suspension has proven capable of producing integrally cored molds with resolved features as fine as 250 micron diameter flag holes and 450 micron diameter film cooling rods. The failure of the initial attempt to cast single crystal demonstrates the importance of proper firing of the LAMP silica mold to establish the properties needed for successful casting of single crystal Ni-super-alloy. The crystallization of silica to cristobalite was used to control creep and sintering shrinkage in the mold, unfortunately cristobalite also reduces room temperature strength. When crystallized to 80% cristobalite content or higher the amorphous silica used in the LAMP process was found to resist sintering and creep during casting while retaining sufficient room temperature strength. For the silica used, 80% cristobalite and 28% porosity were achieved by sintering at 1350°C for 60 minutes, following a 600 minute binder burn-out to 600°C to pyrolizes the organic binder. Crack-like separations between the build layers were found to develop under certain photocuring conditions, but these flaws could be avoided by using a surface dose of UV below the threshold for full curing and photosuspension formulated for low-attenuation.

8.2 Effect of Cristobalite Content and the β-αTransition on Mechanical Properties

The crystallization of silica to cristobalite was used to control creep and sintering shrinkage in the LAMP molds. The impact of cristobalite content on creep and sintering was inferred from the observed rate of stress relaxation under a constant strain as a function of cristobalite content. The observed apparent relaxation time increased with increasing cristobalite content. Also, the relaxation time increased with time as the stress reduced over the course of testing, and this increase in apparent relaxation time over the test increased with increasing cristobalite content. The natural log of the apparent relaxation time was found to be a linear function of the natural log of the remaining stress, with parameters varying as a function of cristobalite content. Samples containing 25% cristobalite had a significantly slower relaxation than fully amorphous samples, but samples containing 52% cristobalite had only slightly slower relaxation than samples containing 25% cristobalite. In turn, samples with 90% cristobalite had significantly slower relaxation than samples with 52% cristobalite content. There is little marginal gain in creep and sintering resistance for increasing cristobalite fraction for intermediate cristobalite contents, suggesting an optimized process should use low cristobalite content or very high cristobalite content.

The gains in sintering and creep resistance with increasing cristobalite content must be balanced against the loss of strength at room temperature due to microfacture caused by the β-α transition of cristobalite. Diametral testing was used to evaluate the strength of cristobalite at 25°C, as α-cristobalite, and at 350°C, as β-cristobalite. In samples with no cristobalite the strength was found to be the same at 25°C and 350°C, indicating any observed difference in strength is a result of the cristobalite. Partially crystallized sintered silica tested at 350°C as β-cristobalite have never passed the β-α transition showed no effect of cristobalite content on strength, illustrating that the weakening at room temperature is entirely due to microfracture on passing the β-α transition. Testing of partially crystallized sintered silica at 25°C showed a loss of strength in sintered silica with cristobalite content of less than 1%. The strength at 25°C as α cristobalite was found to decrease to a minimum for 40-60% cristobalite and increase towards 100% cristobalite content, where the strength as α-cristobalite was ~60% the strength as β-cristobalite having never passed the α-β transition. Samples that were cooled to 25°C and reheated and tested at 350°C as β-cristobalite were found to be as strong or stronger than samples tested at 350°C as β-cristobalite having never cooled through the β-α transition for cristobalite contents of 20-60%; however, such beta-alpha-beta samples were only as strong as α-cristobalite for samples with 100% cristobalite content. The results of testing at 25°C indicate that if cristobalite must be formed, full crystallization will reduce room temperature strength less than an intermediate cristobalite content.

It was originally assumed that an intermediate cristobalite content would be needed in order to balance the need for creep resistance and room temperature strength; however, after investigating the actual behavior sintered silica, this intuition has proven incorrect. Both the strength and stress relaxation results suggest that intermediate cristobalite content produces the worst properties possible by maximally reducing room temperature strength and only marginally improving sintering and creep resistance. Instead, full crystallization provides the best properties by maximizing the resistance to sintering and creep while only moderately reducing strength.

The kinetics of the crystallization of amorphous silica to cristobalite in porous sintered silica was studied and a TTT diagram was developed. The maximum transformation temperature or "nose" of the TTT was found to occur at 1550°C. The lower linear leg of the TTT diagram was found to fit the Avrami or JMAK equation, with an exponent of 3. Cristobalite powder was found to act as seed when mixed with fully amorphous silica powder, accelerating the transformation relative to fully amorphous silica powder without seeding. Silica with 5% residual quartz content from incomplete amorphization was found to have even faster transformation kinetics than the fully amorphous powder seeded with cristobalite. This may suggest the residual quartz acts as a nucleation site; however, TEM studies were unable to confirm this.

Pure cristobalite produced by sintering silica powder was repeatedly cycled from α-to-β and β-to-α and the hysteresis was found to change systematically on cycling. The onset temperatures of both the β-α transition and α-β transition changed logarithmically on cycling to reduce the driving force of the transition, but the β-α transition onset temperature changed more significantly. This logarithmic shift in the onset temperatures was absent in material with a particle size of 38 microns or finer, indicating a critical size for the effect to occur. The enthalpy of the transformation, on the other hand, was constant with cycling and the enthalpy of the β-α transition on cooling was 20% larger than the enthalpy of the α-β transition on heating.

Cristobalite was formed on the surface of bulk pure silica and the development of stress and fracture due to the β-α transition was observed. Cristobalite surface nucleated and grew spherulitically with a <111> growth habit. Stress was observed in the matrix surrounding isolated spherulites, caused by the volume reduction of 4.9% on transition from β-cristobalite to α cristobalite. In spherulites smaller than 15 microns in diameter large radial tensile stresses are observed in the glass matrix, but no fracture occurs. In spherulites larger than 70 microns in diameter nearly every spherulite self-fractured with “dried mud” type cracks passing through the cristobalite. In spherulites larger than 15 microns that do not self-fracture, a fraction are encircled by cracks passing through the matrix; the occurrence of such encircling matrix cracks increases with increasing spherulite diameter.

8.3 Future Work

LAMP molds have been shown capable of successful casting of Ni-super-alloy, but more work is still needed. Only uncored LAMP molds have been successfully cast at this time due to the development of separations which cause breakage of the core as discussed in Chapter 7. The development of separations can be prevented by adjustment of the suspension parameters and the curing parameters during the build, but it comes with a loss of resolution. Further work is needed to develop suspension and curing parameters to produce castable cored LAMP molds.

There is also more work to be done in integration and scale up. The LAMP molds were inefficiently integrated into a casting procedure by substituting the LAMP mold for the wax airfoil. For LAMP to be effective replacements for current methods, a procedure for directly implementing ceramic LAMP molds into a casting assembly are needed. LAMP also needs to be scaled up from the current laboratory scale process to a production scale process. This will necessitate changes in production and handling of the photosuspensions and the processing of green molds. The challenges of scaling up from laboratory to production scale are inherent to any new technology that must be implemented, and the success or failure of scalable will ultimately determine if LAMP truly can revolutionize the casting of airfoils.